

TESE DEFENDIDA POR Gustavo Dalben
Rossetto E APROVADA PELA
COMISSÃO JULGADORA EM 22.08.2001

José Roberto de França Arruda
ORIENTADOR

UNIVERSIDADE ESTADUAL DE CAMPINAS
FACULDADE DE ENGENHARIA MECÂNICA

**Contribuição à teoria e prática da análise modal
acústica experimental**

Autor : **Gustavo Dalben Rossetto**
Orientador: **Prof. Dr. José Roberto de França Arruda**

50/01

**UNIVERSIDADE ESTADUAL DE CAMPINAS
FACULDADE DE ENGENHARIA MECÂNICA
DEPARTAMENTO DE MECÂNICA COMPUTACIONAL**

**Contribuição à teoria e prática da análise modal
acústica experimental**

Autor : **Gustavo Dalben Rossetto**

Orientador: **Prof. Dr. José Roberto de França Arruda**

Curso: Engenharia Mecânica.

Área de concentração: Mecânica dos Sólidos e Projeto Mecânico

Dissertação de mestrado apresentada à comissão de Pós Graduação da Faculdade de Engenharia Mecânica, como requisito para obtenção do título de Mestre em Engenharia Mecânica.

Campinas, 2001

S.P. - Brasil

666612002

**UNICAMP
BIBLIOTECA CENTRAL
SEÇÃO CIRCULANTE**

FICHA CATALOGRÁFICA ELABORADA PELA
BIBLIOTECA DA ÁREA DE ENGENHARIA - BAE - UNICAMP

R735c Rossetto, Gustavo Dalben
Contribuição à teoria e prática da análise modal acústica
experimental. / Gustavo Dalben Rossetto. --Campinas,
SP: [s.n.], 2001.

Orientador: José Roberto de França Arruda.
Dissertação (mestrado) - Universidade Estadual de
Campinas, Faculdade de Engenharia Mecânica

1. Acústica. 2. Análise modal. 3. Fourier, Análise de. I.
Arruda, José Roberto de França. II. Universidade
Estadual de Campinas. Faculdade de Engenharia
Mecânica. III. Título.

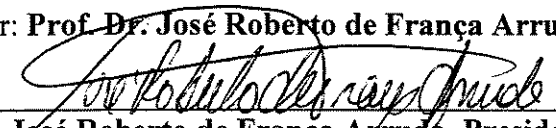
**UNIVERSIDADE ESTADUAL DE CAMPINAS
FACULDADE DE ENGENHARIA MECÂNICA
DEPARTAMENTO DE MECÂNICA COMPUTACIONAL**

DISSERTAÇÃO DE MESTRADO

**Contribuição à teoria e prática da análise modal
acústica experimental**

Autor : **Gustavo Dalben Rossetto**

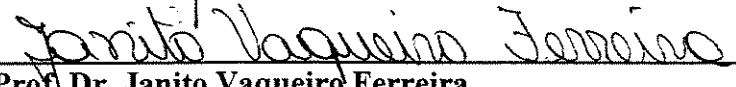
Orientador: **Prof. Dr. José Roberto de França Arruda**



**Prof. Dr. José Roberto de França Arruda, Presidente
FEM/DMC/Unicamp**



**Prof. Dr. Domingos Alves Rade
Faculdade de Engenharia Mecânica da Universidade Federal de Uberlândia**



**Prof. Dr. Janito Vaqueiro Ferreira
FEM/DMC/Unicamp**

Campinas, 22 de Agosto de 2001

Dedicatória

Dedico este trabalho aos meus pais, Adilson José Rossetto e Maria Augusta Dalben Rossetto.
A eles sou grato eternamente pela oportunidade de ser e estar.

Agradecimentos

Agradeço ao Departamento de Mecânica Computacional da Faculdade de Engenharia Mecânica da Unicamp por ter dado todas as condições para que este trabalho fosse desenvolvido, e ao *CNPq* (Conselho Nacional de Desenvolvimento Científico e Tecnológico) por tê-lo financiado.

Minha gratidão e reconhecimento vão ao professor José Roberto de França Arruda, orientador desta tese, pelos ensinamentos, pelo apoio e estímulo constantes, e pelo exemplo de conduta que muito me marca.

Agradeço a Allan Pereira pela orientação desde o primeiros passos na pós-graduação, pelo exemplo, e pela amizade.

Enfim, agradeço a Belisário Hualpa, Khaled Ahmida, Paulo Sérgio Alves e Lázaro Donadon pela excelente recepção no grupo de vibroacústica e pelo apoio constante.

À procura de soluções, os homens caminharão uns pelo campo da tecnologia material e outros, pelo campo espiritual. Maior conflito, então, se instalará, uma vez que a unilateralidade - espírito ou tecnologia material - não promoverá o equilíbrio. Será necessário, para este, a integração da técnica e do espírito, colocados, ambos, em pratos equidistantes da balança, tendo como centro o coordenador-homem.

Dr. Celso Charuri

Resumo

Rossetto, Gustavo Dalben, *Contribuição à teoria e prática da análise modal acústica experimental*, Faculdade de Engenharia Mecânica, Universidade Estadual de Campinas, 2001. 121 p. Dissertação (Mestrado)

Neste trabalho uma geometria simples (cavidade retangular) é usada para o estudo da metodologia aplicada na análise modal acústica. Modelos analítico e numérico são desenvolvidos para a comparação com os resultados experimentais. Três tipos de dispositivos de excitação do sistema acústico foram construídos. Um baseado num pistão conectado a um *shaker*, e outros dois usando um alto-falante do tipo *driver*. O primeiro atuador usando o *driver* é similar ao modelo desenvolvido por um projeto europeu, onde um tubo flexível com uma terminação instrumentada com um microfone é usado para a condução da excitação acústica. O segundo atuador baseado no uso do *driver* também usa um tubo flexível, mas este é instrumentado com dois microfones em sua terminação. O comportamento destes dois últimos atuadores em termos de aceleração de volume (essencial para a análise modal acústica experimental) e de potência ativa (necessária para Análise Estatística de Energia Experimental) sendo injetados no meio são investigados. A análise modal experimental da cavidade retangular é realizada e um método que utiliza a transformada de Fourier espacial multidimensional do campo de pressão medido é proposto para a construção do campo de deslocamento de partícula para a visualização do modo acústico.

Palavras Chave

- Cavidade, atuadores acústicos, Transformada de Fourier Discreta espacial, visualização do modo acústico

Abstract

Rossetto, Gustavo Dalben, *A contribution to the theory and practice of experimental acoustic modal analysis*, Faculdade de Engenharia Mecânica, Universidade Estadual de Campinas, 2001. 121 p. Dissertação (Mestrado)

In the present work, a simple geometry (rectangular shallow cavity) is used to investigate the acoustic modal analysis methodology. Analytical and numerical models are developed for the comparison with the experimental results. Three types of excitation devices were constructed. One based on a shaker-driven piston and the other two using a driver loudspeaker. The first actuator based on a driver loudspeaker is similar to a model developed by an EEC project, where a flexible tube with a socket, instrumented with one microphone, at its termination is used to conduct the sound excitation. The second actuator based on a driver loudspeaker also uses a flexible tube, but it is instrumented with two microphones in its socket instead of one. The behavior of these last two actuators in terms of volume acceleration (essential in the acoustic modal analysis) and active power (necessary for the Experimental Statistical Energy Analysis) being injected into the medium are investigated. The experimental modal analysis of the rectangular cavity is performed and a method using multi-dimensional spatial Fourier transforms of the array of pressure measurements is proposed for the construction of the particle displacement field for acoustic mode shape visualization.

Key Words

- Cavity, acoustic actuators, spatial Discrete Fourier Transform, acoustic mode shape visualization

Índice

<i>Lista de Figuras</i>	<i>i</i>
<i>Lista de Tabelas</i>	<i>vi</i>
<i>Nomenclatura</i>	<i>vii</i>
<i>Capítulo 1</i>	<i>1</i>
<i>Introdução</i>	<i>2</i>
<i>Chapítulo 2</i>	<i>5</i>
<i>Sistremas Acústicos</i>	<i>5</i>
2.1 – <i>Introdução</i>	<i>5</i>
2.2 – <i>Analogia Mecânica</i>	<i>5</i>
2.3 – <i>Equação da onda não homogênea</i>	<i>11</i>
2.4 – <i>Visualização de modos em sistemas acústicos</i>	<i>13</i>
<i>Capítulo 3</i>	<i>15</i>
<i>Análise modal numérica e analítica de uma cavidade rectangular</i>	<i>15</i>
3.1 – <i>Introdução</i>	<i>15</i>
3.2 – <i>Solução analítica</i>	<i>16</i>
3.3 – <i>Modelo de Elementos Finitos</i>	<i>20</i>
<i>Capítulo 4</i>	<i>32</i>
<i>Desenvolvimento de um atuador com um microfone</i>	<i>32</i>
4.1 – <i>Introdução</i>	<i>32</i>
4.2 – <i>Revisão da teoria de dutos</i>	<i>32</i>
4.3 – <i>Atuador de um microfone</i>	<i>36</i>
4.4 – <i>Formulação Mathemática</i>	<i>39</i>
4.5 – <i>Validação experimental</i>	<i>40</i>

<i>Capítulo 5</i>	47
<i>Desenvolvimento de um atuador com dois microfones</i>	47
5.1 – Introdução	47
5.2 – Formulação Matemática	48
5.3 – Validação experimental	55
5.4 – Aceleração de volume	56
5.5 – Potência acústica ativa	59
<i>Capítulo 6</i>	68
<i>Resultados and discussões</i>	68
6.1 – Introdução	68
6.2 – Experimento com atuador eletrodinâmico	71
6.3 – Experimento com atuador de um microfone	73
6.4 – Experimento com atuador de dois microfones	76
6.5 – General analysis	78
6.6 – Pressure and particle velocity fields visualization	81
<i>Capítulo 7</i>	85
<i>Conclusões e perspectivas</i>	85
<i>Referências</i>	88
<i>Apêndice A</i>	91
<i>Equação da onda acústica</i>	91
<i>Apêndice B</i>	96
<i>Intensidade acústica</i>	96
B.1 – Intensidade acústica em ondas planas	96
B.2 – Intensidade complexa para campos acústicos harmônicos	99
B.3 – Intensidade do monopolo	101
<i>Apêndice C</i>	103
<i>Impedância acústica específica para ondas esféricas e fonte pontual</i>	103
<i>Apêndice D</i>	105
<i>Transformada de Fourier Espacial Discreta</i>	105
D.1 – Problema Uni-dimensional	105
D.2 – Problema Bi-dimensional	109
D.3 – Problema Tri-dimensional	118

Apêndice E..... 120
Esquema do atuador..... 120

Index

<i>Figure list</i>	<i>i</i>
<i>Table list</i>	<i>vi</i>
<i>Nomenclature</i>	<i>vii</i>
<i>Chapter 1</i>	<i>1</i>
<i>Introduction</i>	<i>1</i>
<i>Chapter 2</i>	<i>5</i>
<i>Acoustic systems</i>	<i>5</i>
2.1 – Introduction	<i>5</i>
2.2 – Mechanical Analogy	<i>5</i>
2.3 – Inhomogeneous wave equation.....	<i>11</i>
2.4 – Mode shape visualization in acoustic systems	<i>13</i>
<i>Chapter 3</i>	<i>15</i>
<i>Numerical and analytical modal analysis of a rectangular cavity</i>	<i>15</i>
3.1 – Introduction	<i>15</i>
3.2 – Analytical solution.....	<i>16</i>
3.3 – Finite Element model.....	<i>20</i>
<i>Chapter 4</i>	<i>32</i>
<i>One-microphone actuator development</i>	<i>32</i>
4.1 – Introduction	<i>32</i>
4.2 – Duct theory revision	<i>33</i>
4.3 – One-microphone actuator	<i>36</i>
4.4 – Mathematical formulation.....	<i>39</i>
4.5 – Experimental validation	<i>40</i>

<i>Chapter 5</i>	47
<i>Two-microphone acoustic actuator development</i>	47
5.1 – Introduction	47
5.2 – Mathematical formulation.....	48
5.3 – Experimental validation.....	55
5.4 – Volume acceleration	56
5.5 – Active acoustic power.....	59
<i>Chapter 6</i>	68
<i>Results and discussions</i>	68
6.1 – Introduction	68
6.2 – Shaker-driven piston actuator experiment	71
6.3 – One-microphone actuator experiment.....	73
6.4 – Two-microphone actuator experiment.....	76
6.5 – General analysis.....	78
6.6 – Pressure and particle velocity fields visualization	81
<i>Chapter 7</i>	85
<i>Conclusions and perspectives</i>	85
<i>References</i>	88
<i>Appendix A</i>	91
<i>Acoustic wave equation</i>	91
<i>Appendix B</i>	96
<i>Acoustic intensity</i>	96
B.1 – Acoustic intensity in plane wave fields.....	96
B.2 – Complex intensity for harmonic acoustic fields.....	99
B.3 – Monopole intensity	101
<i>Appendix C</i>	103
<i>Acoustic specific impedance for a spherical wave diverging from a point source</i>	103
<i>Appendix D</i>	105
<i>Spatial Discrete Fourier Transform</i>	105
D.1 – One-dimensional problem.....	105
D.2 – Two-dimensional problem	109
D.3 – Three-dimensional problem	118

Appendix E..... 120
Actuators' scheme..... 120

Figure list

<i>Figure 2.2.1 – Pipe element</i>	6
<i>Figure 2.2.2 – Cavity element</i>	7
<i>Figure 2.2.3 – Automotive exhaust system</i>	8
<i>Figure 2.2.4 – Exhaust system mechanical analog</i>	10
<i>Figure 2.3.1 – Monopole oscilation</i>	12
<i>Figure 3.1.1 – Rectangular cavity</i>	15
<i>Figure 3.3.1 – Two-dimensional domain</i>	21
<i>Figure 3.3.2 – Linear triangular element</i>	23
<i>Figure 3.3.3 – Triangular element</i>	25
<i>Figure 4.1.1 – Acoustic actuator calibrated with one microphone</i>	32
<i>Figure 4.2.1 – Flanged open-ended tube</i>	34
<i>Figure 4.2.2 – Specific acoustic impedance</i>	35
<i>Figure 4.2.3 – Unflanged open-ended tube</i>	35
<i>Figure 4.3.1 – Constructed socket</i>	38
<i>Figure 4.3.2 – Driver loudspeaker connected to the flexible tube</i>	38
<i>Figure 4.5.1 – Experiment in a room simulating a free-field</i>	40
<i>Figure 4.5.2 – Measurement locations</i>	41
<i>Figure 4.5.3 – Auto power spectral densities (21.8cm far from the source)</i>	41
<i>Figure 4.5.4 – Auto power spectral densities in 5 points (all located 21.8cm far from the source)</i>	42
<i>Figure 4.5.5 – Transfer function H constructed ($r = 0.2m$)</i>	42
<i>Figure 4.5.6 – Volume acceleration comparison ($r = 0.40m$)</i>	44

<i>Figure 4.5.7 – Active power comparison ($r = 0.40m$)</i>	44
<i>Figure 4.5.8 – Microphone positioning inside the socket</i>	45
<i>Figure 4.5.9 – Volume acceleration comparison ($r = 0.40m$) with correction</i>	45
<i>Figure 4.5.10 – Active power comparison ($r = 0.40m$) with correction</i>	46
<i>Figure 5.2.1 – Traveling waves and microphone positioning in the socket</i>	49
<i>Figure 5.2.2 – Estimate of phase shift between microphones 1 and 2</i>	54
<i>Figure 5.2.3 – Amplitude $(e^{i\phi} + 1)/2$ using the estimate of the phase shift</i>	54
<i>Figure 5.3.1 – Two-microphone actuator socket constructed</i>	55
<i>Figure 5.4.1 – Comparison between volume acceleration calculated from A and B (arithmetic average) and from the monopole theory applied to $p(r = 0.40m) - 0$ to 3.2kHz</i>	55
<i>Figure 5.4.2 – Comparison between volume acceleration calculated from A and B (arithmetic average) and from the monopole theory applied to $p(r = 0.40m) - 300$ to 2500Hz</i>	55
<i>Figure 5.4.3 – Comparison between volume acceleration calculated from A and B (arithmetic average) and from the monopole theory applied to $p(r = 0.40m) - 0$ to 3.2kHz</i>	55
<i>Figure 5.4.4 – Comparison between volume acceleration calculated from A and B (arithmetic average) and from the monopole theory applied to $p(r = 0.40m) - 0$ to 6.4kHz</i>	55
<i>Figure 5.4.5 – Volume acceleration calculated from A and B (arithmetic average) varying Δ_2 from 0.060m to 0.065m – 0 to 6.4kHz</i>	55
<i>Figure 5.5.1 – Magnitudes of A and B for a free-field experiment</i>	55
<i>Figure 5.5.2 – Magnitudes of A and B for the rectangular cavity experiment</i>	55
<i>Figure 5.5.3 – Comparison of the active acoustic power calculated from the radiation impedance applied to u_{AB} and from the monopole theory applied to $p(r=0.4m) - 0-6.4kHz$</i>	55
<i>Figure 5.5.4 – Comparison of the active acoustic power calculated from A and B and from the monopole theory applied to $p(r=0.4m) - 0-6.4kHz$</i>	55
<i>Figure 5.5.5 – Comparison of the pressure at the socket termination calculated from A and B with correction and from the radiation impedance applied to $u_{AB} - 0-6.4kHz$</i>	55

<i>Figure 5.5.6 – Comparison of the pressure at the socket termination calculated from A and B using $\Delta_2 = 0.062m$ and from the radiation impedance applied to $u_{AB} - 0-6.4kHz$</i>	55
<i>Figure 5.5.7 – Comparison of the pressure at the socket termination calculated from A and B with correction and from the radiation impedance applied to $u_{AB} - 0-6.4kHz$</i>	55
<i>Figure 5.5.8 – Comparison of the active acoustic power calculated from A and B with correction and from the monopole theory applied to $p(r=0.4m) - 0-6.4kHz$</i>	55
<i>Figure 5.5.9 – Comparison of the reactive acoustic power calculated from A and B and from the radiation impedance applied to $u_{AB} - 0-6.4kHz$</i>	55
<i>Figure 5.5.10 – Comparison of the reactive acoustic power calculated from A and B with correction and from the radiation impedance applied to $u_{AB} - 0-6.4kHz$</i>	55
<i>Figure 5.5.11 – Comparison of the active acoustic power calculated from A and B and from the geometric average of $S_{12} - 0-6.4kHz$</i>	55
<i>Figure 6.1.1 – Shaker-driven piston actuator assembly</i>	55
<i>Figure 6.1.2 – One-microphone actuator</i>	55
<i>Figure 6.1.3 – Constructed cavity</i>	55
<i>Figure 6.1.4 – Rectangular cavity FEM mesh</i>	55
<i>Figure 6.2.1 – Shaker-driven piston (left) and the experimental setup (right)</i>	55
<i>Figure 6.2.2 – Comparison between the analytical and experimental FRFs at the points 53 (left) and 80 (right)</i>	55
<i>Figure 6.2.3 – Coherence (between the microphone inside the cavity and the accelerometer mounted on the piston) and FRFs at the points 53 (left) and 80 (right)</i>	55
<i>Figure 6.3.1 – Experimental setup for the application of the one-microphone actuator</i>	55
<i>Figure 6.3.2 – Comparison between the FRFs constructed using H and the radiation impedance without correction (left) and with correction (right) at the point 53</i>	55
<i>Figure 6.3.3 – Comparison between the FRFs constructed using H and the radiation impedance without correction (left) and with correction (right) at the point 80</i>	55

<i>Figure 6.3.4 – Comparison between the analytical and experimental (using the radiation impedance with correction) FRFs at the points 53 (left) and 80 (right)</i>	55
<i>Figure 6.3.5 – Coherence between the microphones, and FRFs at the points 53 (left) and 80 (right)</i>	55
<i>Figure 6.4.1 – Experimental setup for the application of the two-microphone actuator</i>	55
<i>Figure 6.4.2 – Comparison between the analytical and experimental FRFs at the points 53 (left) and 80 (right)</i>	55
<i>Figure 6.4.3 – Coherence between the microphones, and FRFs at the points 53 (left) and 80 (right)</i>	55
<i>Figure 6.5.1 – Comparison between the analytical and numerical(FEM) FRFs at the points 53 (left) and 80 (right)</i>	55
<i>Figure 6.5.2 – Comparison between the experimental FRFs using the shaker-driven piston actuator and the two-microphone actuator at the points 53 (left) and 80 (right)</i>	55
<i>Figure 6.5.3 – Comparison between the experimental FRFs using the one-microphone actuator (using the radiation impedance) and the two-microphone actuator at the points 53 (left) and 80 (right)</i>	55
<i>Figure 6.6.1 – Original (left) and mirrored (right) experimental pressure field for the 3rd mode (1100Hz)</i>	55
<i>Figure 6.6.2 – Analytical particle velocity field in x-(left) and y-(right) directions for the 3rd mode (1100Hz)</i>	55
<i>Figure 6.6.3 – Particle velocity field from DFT in x-(left) and y-(right) directions for the 3rd mode (1100Hz)</i>	55
<i>Figure 6.6.4 – Original (left) and filtered (right) FFT of the pressure field for the 3rd mode (1100Hz)</i>	55
<i>Figure 6.6.5 – Particle velocity field from filtered data in x-(left) and y-(right) directions for the 3rd mode (1100Hz)</i>	55
<i>Figure 6.6.6 – Wire-frame representation of the particle displacement field for the 3rd mode (1100Hz);</i>	55
<i>Figure 7.1 – Microphone mounting in the tube wall</i>	55

<i>Figure 7.2 – Improved acoustic actuator</i>	<i>55</i>
<i>Figure A.1 – Mass flux through a fluid control volume in the x direction</i>	<i>55</i>
<i>Figure A.2 – Pressure gradient in the x direction</i>	<i>55</i>
<i>Figure B.2.1 – Phase shift between pressure and particle velocity.....</i>	<i>55</i>
<i>Figure D.1.1 – Function $f(x)$ for $A = 1$ and $L = 3$.....</i>	<i>55</i>
<i>Figure D.1.2 – Analytical (—) and from DFT/IDFT (•) first derivative of $f(x)$</i>	<i>55</i>
<i>Figure D.2.1 – Pressure field for the 8th mode (1850Hz).....</i>	<i>55</i>
<i>Figure D.2.2 – x-component of the particle velocity for the 8th mode.....</i>	<i>55</i>
<i>Figure D.2.3 – y-component of the particle velocity for the 8th mode.....</i>	<i>55</i>
<i>Figure D.2.4 – Pressure field for the 12th mode (438Hz).....</i>	<i>55</i>
<i>Figure D.2.5 – Pressure field for the 12th mode (438Hz).....</i>	<i>55</i>
<i>Figure D.2.6 – θ-component of the particle velocity for the 12th mode</i>	<i>55</i>
<i>Figure D.2.7 – r-component of the particle velocity for the 12th mode.....</i>	<i>55</i>
<i>Figure D.3.1 – Pressure field for the 43th mode (1964Hz).....</i>	<i>55</i>
<i>Figure D.3.2 – x-component of the particle velocity for the 43th mode.....</i>	<i>55</i>
<i>Figure D.3.3 – Particle displacement (left) and pressure (right) fields for the 43th mode.....</i>	<i>55</i>

Table list

<i>Table 6.5.1 – Errors in the numerical natural frequencies with respect to the analytical value.....</i>	<i>55</i>
<i>Table 6.5.2 – Modal parameters from the application of the three actuators.....</i>	<i>55</i>
<i>Table 6.5.3 – Errors in the experimental natural frequencies with respect to the analytical value.....</i>	<i>55</i>

Nomenclature

p	<i>acoustic pressure</i>
u	<i>particle velocity</i>
c	<i>thermodynamic speed of sound</i>
k	<i>wave number</i>
p_0	<i>mean pressure</i>
q, Q	<i>volume velocity</i>
\dot{q}, \dot{Q}	<i>volume acceleration</i>
s	<i>condensation, switched microphones</i>
i	$\sqrt{-1}$
a	<i>tube radius</i>
r	<i>distance to the source</i>
S_{xy}	<i>two-sided cross power spectral density</i>
S_{xx}	<i>two-sided auto power spectral density</i>
$*$	<i>complex conjugate</i>
$\langle \ \rangle$	<i>average</i>

Greek letter symbols

ρ	<i>fluid mass density</i>
ρ_0	<i>mean fluid density</i>
ω	<i>angular frequency</i>

ω_r	<i>natural angular frequency</i>
ω'_r	<i>damped natural angular frequency</i>
η	<i>damping loss factor</i>
ζ	<i>viscous damping factor</i>
Δ_1	<i>microphone separation</i>
Δ_2	<i>distance from microphone p_1 to the tube termination</i>
ϕ	<i>phase angle</i>
γ	<i>ratio of heat capacities</i>

Capítulo 1

Introdução

A importância prática da análise modal acústica tem aumentado nos últimos anos. No campo experimental, algumas dificuldades ainda não foram superadas e o presente trabalho apresenta um estudo sobre algumas delas. São elas: correções de unidades que permitam a comparação entre resultados analítico, numérico e experimental; a realização da excitação acústica calibrada; e a visualização dos modos acústicos.

Na atual literatura envolvendo sistemas acústicos, pouca atenção tem sido dada na definição de variáveis acústicas de excitação e resposta, fundamentais na análise modal experimental. Augusztinovicz e Sas (1996) trataram este assunto e apresentaram uma formulação onde a aceleração de volume é a variável de entrada e a pressão a variável de resposta nas equações dinâmicas de sistemas acústicos. A pressão é facilmente medida com microfones, enquanto que a aceleração de volume pode ser produzida por um fonte sonora calibrada, tal como um alto-falante em configuração especial.

Nieter e Singh (1982) desenvolveram uma metodologia para a análise modal acústica onde as mesmas ferramentas aplicadas na mecânica dos sólidos (analisadores de Fourier, métodos de extração de parâmetros modais, etc.) são usadas. A técnica não apresenta problemas com respeito às medidas de pressão, que podem ser feitas com microfones ou transdutores de pressão bastante sensíveis, mas tem que lidar com a excitação acústica (aceleração de volume do fluido) que não

possui medição direta devido à falta de um transdutor de velocidade de partícula¹ confiável e preciso numa larga faixa de frequência. A solução encontrada foi o uso de um pistão movimentado por um *shaker*, sendo que a medida de aceleração de volume é obtida pelo sinal de aceleração (dado por um acelerômetro conectado ao pistão) multiplicado pela área do pistão. Um trabalho posterior de Singh e Kung (1985) propõe uma outra solução que utiliza um alto-falante do tipo *driver*, onde a aceleração de volume é monitorada por um microfone montado numa pequena cavidade de volume conhecido na parte traseira do *driver*. Este dispositivo de excitação foi então aplicado diretamente no ponto de excitação do sistema acústico testado.

O problema relacionado com a visualização dos modos acústicos foi tratado por Whear e Morrey (1996), que usaram uma sonda com três microfones alinhados para, a partir do cálculo de diferenças finitas de segunda ordem, obterem a derivada espacial de segunda ordem da pressão. Como a primeira derivada espacial relaciona-se (equação de Euler) diretamente com a aceleração de partícula, a derivada espacial de segunda ordem irá exibir o mesmos nós e anti-nós da distribuição de pressão. A desvantagem deste método é o efeito de amplificação do ruído gerado pela dupla diferenciação do campo de pressão medido. Outra metodologia é apresentada por Byrne (1985), que usa a pressão medida numa sequência de pontos no domínio acústico experimental para extrair funções aproximadas formadas por polinômios para calcular o gradiente de pressão numa determinada direção. Tendo o gradiente de pressão, a aceleração de partícula é calculada aplicando-se a equação de Euler.

No presente trabalho, uma geometria simples (cavidade retangular) é usada no estudo da metodologia da análise modal acústica. Modelos analíticos e numéricos serão desenvolvidos para posterior comparação com resultados experimentais, que serão obtidos com o uso de três diferentes dispositivos de excitação. O primeiro consiste de um pistão, movimentado por um *shaker*, que desloca uma membrana elástica, como feito por Arruda e Huallpa (1999). O segundo utiliza um alto-falante do tipo *driver* e é similar a um modelo desenvolvido por um projeto europeu (Van Tol e Verheij, 1993). Esta configuração possui uma vantagem sobre a aplicação do *driver* diretamente no ponto de excitação que é o uso de um tubo conduzindo a excitação sonora, permitindo que o atuador seja facilmente posicionado em diferentes pontos de um espaço confinado. Este atuador possui um bocal, instrumentado com um microfone, que é instalado na

¹ Muito recentemente um transdutor de velocidade de partícula comercial para aplicações acústicas se tornou disponível (Bree et al., 2000), mas sua faixa de frequência é ainda muito limitada. Veja os comentários do capítulo 2.

terminação do tubo. Sua calibração baseia-se na hipótese de que a impedância acústica do atuador é muito maior do que a impedância do meio em que ele atua. O terceiro atuador possui a mesma estrutura deste último, mas usa dois microfones em seu bocal. A impedância do meio não é mais ignorada, mas a técnica dos dois microfones utilizada possui alguns problemas intrínsecos (i.e., defasagem entre os microfones) que serão discutidos (as referências utilizadas serão apresentadas no capítulo 5).

A questão relacionada à visualização dos modos acústicos é discutida e um método que utiliza as transformadas espaciais multi-dimensionais de Fourier do campo de pressão medido é proposto para a construção do campo de deslocamento de partícula.

Uma segunda aplicação dos atuadores acústicos que usam um ou dois microfones é a medida de potência acústica ativa que é injetada no meio. Este assunto é de grande importância em Análise Energética Estatística Experimental (ESEA) e é tratado nos capítulos 4 e 5. O principal objetivo do presente trabalho com relação ao desenvolvimento de atuadores acústicos é a correta medição de aceleração de volume que é injetada no meio. Dos resultados preliminares das medidas de potência acústica ativa foi possível entender este problema que está em aberto e propor soluções para trabalhos futuros.

A seguir, uma breve descrição do conteúdo de cada capítulo é apresentada.

Capítulo 2

Este capítulo apresenta o primeiro passo dado neste trabalho, que foi a compreensão das características e peculiaridades do estudo de sistemas acústicos. Uma analogia mecânica é usada para melhor compreensão das variáveis acústicas utilizadas na excitação e na resposta do sistema. A equação não-homogênea da onda e o termo fonte são estudados e uma discussão sobre a visualização dos modos acústicos é feita. O apêndice D apresenta o desenvolvimento matemático do método proposto e o capítulo 6 sua aplicação em um campo de pressão experimental.

Capítulo 3

Os modelos analítico e numérico da cavidade acústica retangular são desenvolvidos neste capítulo. A Função de Resposta em Frequência (FRF) para cada modelo é deduzida e as correções de unidades necessárias para a comparação com as FRFs experimentais são apresentadas.

Capítulo 4

Este capítulo inicia-se com uma breve revisão da teoria de dutos, que será de grande importância no estudo e desenvolvimento dos atuadores que usam um tubo conectado a um alto-falante. A formulação matemática para o atuador que usa um microfone é dada e os resultados experimentais, obtidos numa sala onde as paredes foram tratadas para simular um campo livre, são apresentados.

Capítulo 5

O desenvolvimento do atuador que usa dois microfones é apresentado neste capítulo. Como mencionado acima, alguns problemas intrínsecos à técnica dos dois microfones são estudados e as referências apresentadas. Resultados experimentais obtidos numa sala onde as paredes foram tratadas para simular um campo livre são mostrados e discutidos.

Capítulo 6

Os resultados da aplicação dos três atuadores acústicos na cavidade retangular são apresentados e a análise modal é realizada. As FRFs analíticas são comparadas com os resultados experimentais e numéricos. Finalizando este capítulo, o método apresentado no capítulo 2 e no apêndice D é aplicado num campo pressão experimental da cavidade retangular e o campo de velocidade de partícula obtido é analisado.

Capítulo 7

Este capítulo apresenta as conclusões e perspectivas.

Chapter 2

Acoustic systems

2.1 – Introduction

The description of an acoustic system can be easily understood when an analogy with a mechanical system is made. Nevertheless, attention must be paid when defining excitation and response variables as the nature of the problem is different. In this chapter a simple acoustic model – supposing that frequency is low enough – is discretized into lumped elements and compared to its mechanical analog. As shown in (Augustinovicz, 2000), this analysis is very insightful and the extension to the study of acoustic systems with distributed parameters (where the dimensions of the acoustic system are not small compared to the wavelength of interest) is straightforward. After the choice of input and output acoustic variables is understood, an analysis over the inhomogeneous wave equation will be carried out in order to understand the physical meaning of different types of acoustic excitations and the type of excitation suitable for modal analysis. The chapter ends with a discussion on the mode shape visualization in an acoustic system.

2.2 – Mechanical Analogy

A very insightful way of understanding what the acoustic variables represent in an acoustic system is the development of a mechanical analogy. This is possible when the frequency range of

analysis is low enough (wavelengths much bigger than the dimensions of the system or subsystem) to allow the use of concentrated (or lumped) acoustic parameters. The following formulation is developed as in (Arruda and Huallpa, 1999), where the impedance for two acoustic elements of interest (pipes and cavities) are found. In the case of the pipe (Figure 2.2.1), the excitation will be the volume velocity q and the response the pressure p . If an oscillating piston is put at the pipe termination, the air volume inside the pipe will move as a rigid body and, according to the Newton's law, the force exerted by the piston can be written:

$$F = p A = \rho_0 A L \frac{d^2 x}{d^2 t} \quad (2.2.1)$$

and the pressure is readily calculated:

$$p = \rho_0 L \frac{d u}{d t} \quad (2.2.2)$$

where u is the particle velocity.

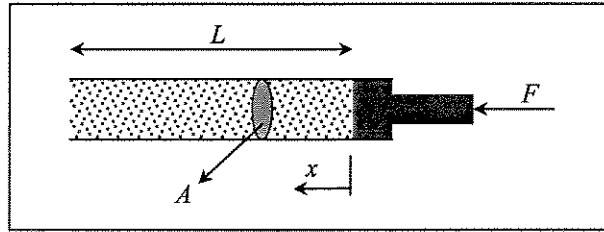


Figure 2.2.1 – Pipe element

In the frequency domain, assuming a harmonic oscillation, the pressure can be expressed as:

$$\hat{p} = i \omega \rho_0 L \hat{u} \quad (2.2.3)$$

The pressure \hat{p} is finally written in terms of volume velocity \hat{q} (particle velocity times area):

$$\hat{q} = A \hat{u} \rightarrow \hat{p} = \frac{\rho_0 L}{A} i \omega \hat{q} \quad \text{or} \quad \hat{p} = \frac{\rho_0 L}{A} \hat{q} \quad (2.2.4)$$

The term $\frac{\rho_0 L}{A}$ is called *acoustic inertance* and will be represented here by the letter M .

In the case of a cavity (figure 2.2.2), the displacement x produced by the piston will cause a change in the volume V and, consequently, a condensation:

$$s = \frac{\Delta\rho}{\rho} = -\frac{\Delta V}{V} = \frac{Ax}{V} \quad (2.2.5)$$

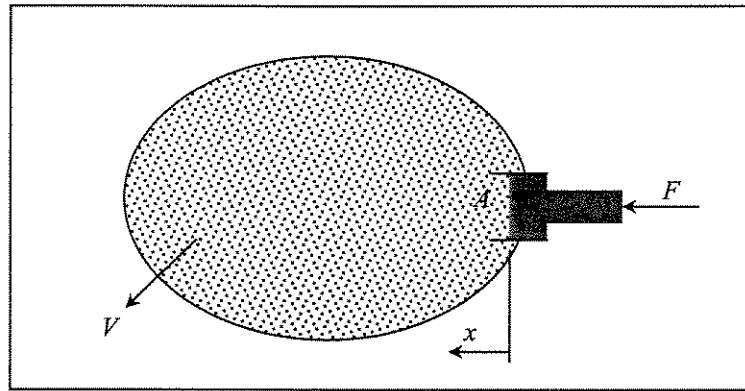


Figure 2.2.2 – Cavity element

From equation (A.5) and the definition of sound speed ($c = \sqrt{\gamma P_0 / \rho_0}$), the pressure can be written as:

$$p = c^2 \rho_0 s \quad (2.2.6)$$

The force exerted by the piston is readily calculated:

$$F = pA = \frac{\rho_0 c^2 A^2}{V} x \quad (2.2.7)$$

Combining the two last equations, it results:

$$\hat{p} = \frac{\rho_0 c^2 A}{V} \hat{x} \rightarrow \hat{p} = \frac{\rho_0 c^2 A}{V} \frac{\hat{u}}{i\omega} \quad (2.2.8)$$

The volume velocity as function of the pressure is finally written:

$$\hat{q} = i\omega \frac{V}{\rho_0 c^2} \hat{p} \quad (2.2.9)$$

where the term $\frac{V}{\rho_0 c^2}$ is known as *acoustic compliance*, which in a mechanical analogy would represent the inverse of the spring stiffness ($1/k$).

To complete the mechanical analogy, a dissipative term (generated by the friction between the fluid and the boundaries, an opening to the free-field, or the absorption by some material present in the acoustic domain) analog to the mechanical damping is defined as *acoustic resistance*. It is represented by a constant ratio between pressure and volume velocity.

A simple example of the application of the theory showed above is an exhaust system consisting of three acoustic inertances and 2 acoustic compliances. Figure 2.2.3 shows schematically this acoustic system with its mechanical analog. The real part of the impedances at the open ends was neglected and thus the system is undamped.

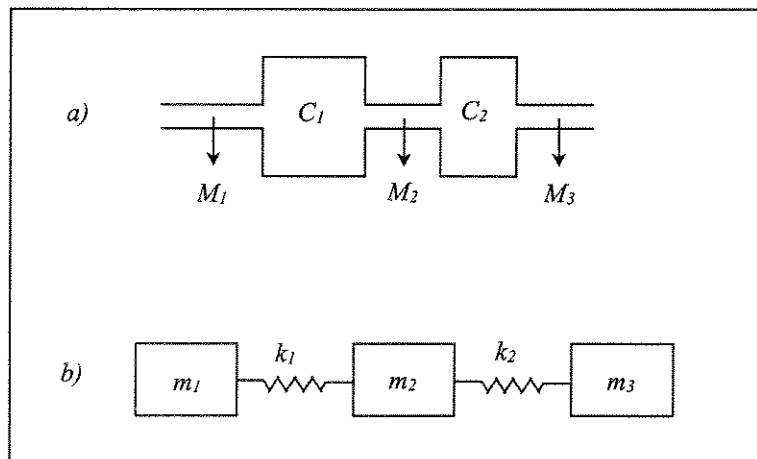


Figure 2.2.3 – Automotive exhaust system
a) Acoustic model b) Mechanical analog

Introduction

The practical importance of the acoustic modal analysis has increased in recent years. In the experimental domain, some difficulties are still to be solved and the present work addresses some of them, namely the unit corrections which are necessary to allow the comparison between analytical, numerical and experimental results, the acoustic excitation realization, and the mode shape visualization.

In the current literature on acoustical systems, little attention is paid to defining excitation and response acoustic variables such that an experimental modal analysis is feasible. Augusztinovicz and Sas (1996) have addressed this problem. They have proposed a formulation where volume acceleration is the input variable and pressure the response variable in the dynamic equations of the acoustic system. Pressure may be easily measured with microphone, while volume acceleration can be produced by calibrated sound sources such as loudspeakers in specially designed configurations.

Nieter and Singh (1982) developed a methodology for acoustical modal analysis where the same tools applied in solid mechanics (Fourier analyzers, modal parameter extraction methods, etc.) are used. The technique faces no problem with respect to the pressure measurement, which can be done with microphones or very sensitive pressure transducers, but has to deal with the acoustic input (volume acceleration of the fluid) that has no direct measurement due to the lack of a reliable and accurate broad-band particle velocity transducer¹. The solution found was the use of a piston driven by a shaker with an accelerometer attached. Later work by Singh and Kung (1985) proposes another solution, based on a driver loudspeaker, where the volume velocity is monitored by a microphone mounted on a small enclosure of known volume at the back of the driver. The acoustic driver was mounted directly at the point of excitation in the acoustic system being tested.

The problem related to the acoustic mode visualization is treated by Whear and Morrey (1996) where a probe with three aligned microphones gives, using a second-order finite difference calculation, the second-order derivative of the pressure relative to the space. Given that, the first-order derivative is related (Euler's equation) to the particle acceleration, the second-order derivative, while being directional, will still exhibit the same nodes and antinodes as the pressure distribution. The disadvantage of this method is the noise amplification effect of differentiating twice the measured pressure field. Another approach is given by Byrne (1985) who uses the pressure measured at an array of points in the acoustic experimental domain to extract approximating functions formed by polynomials to calculate the pressure gradient in one specific direction. Given the pressure gradient, the particle acceleration is readily calculated by applying the Euler's relation.

In the present work, a simple geometry (rectangular shallow cavity) is used to investigate the acoustical modal analysis methodology. Analytical and numerical models are developed for the comparison with the experimental results, which are constructed using three different excitation devices. The first one consists of shaker-driven piston which thrusts against a thin elastic membrane as done by Arruda and Huallpa (1999). The second one is based on a driver loudspeaker and is similar to a model developed by an EEC project (Van Tol and Verheij, 1993). It presents an advantage over the direct use of the driver located at the excitation point which is the use of a tube conducting the sound excitation, allowing the actuator to be easily placed at different locations in a confined space. This actuator has a socket which is instrumented with one microphone and placed at the tube termination. Its calibration is supported by the hypothesis that the actuator acoustic impedance is much higher than the impedance of the surrounding medium where it acts in. The third actuator has the same structure as this last one, but uses two microphones at the socket. The surrounding impedance is no longer ignored, but the use of the two microphone technique has some intrinsic problems (i.e., phase mismatch between the microphones) which will be discussed (the references used are presented in Capítulo 5).

The question related to the mode shape visualization is discussed and a method using multi-dimensional spatial Fourier transforms of the array of pressure measurements is proposed for the construction of the particle displacement field.

A secondary application of the acoustic actuators using one or two microphones is the measurement of the active acoustic power being injected into the medium. This subject is of significant importance in Experimental Statistical Energy Analysis (ESEA) and is treated in Capítulos 4 and 5. The main objective of the present work concerning the actuator development is the correct measurement of the volume acceleration being injected into the medium. From the preliminary results on the active acoustic power measurement it was possible to understand this open problem and to propose solutions for future works.

Following, a brief description of the contents of each Capítulo is presented.

Capítulo 2

This Capítulo presents the first step given in this work, which is the understanding of the characteristics and particularities of the study of acoustic systems. A mechanical analogy is used in order to make the definitions of input and output acoustic variables more clear. The inhomogeneous wave equation and the source term are studied and the discussion on the mode shape visualization is done. Apêndice D presents the mathematical development of the proposed method and Capítulo 6 its application to an experimental pressure field.

Capítulo 3

The analytical and numerical models of the rectangular acoustic cavity are developed in this Capítulo. The Frequency Response Functions (FRF) for each model are derived and the unit corrections needed for the comparison with the experimental FRFs are given. -

¹ Very recently a commercial particle velocity transducer for acoustic applications has become available (Bree et al., 2000) but its frequency range is still quite limited. See comments in Capítulo 2.

Capítulo 4

This Capítulo starts with a brief review on the duct theory that will be of great importance in the study of the actuators using a tube attached to a driver loudspeaker. The mathematical formulation for the actuator using one microphone is given and the experimental results, obtained in a room where the walls were treated to simulate a free-field, are presented.

Capítulo 5

The development of the actuator using two microphones is presented in this Capítulo. As mentioned above, some intrinsic problems related to the use of the two-microphone technique are investigated and references presented. Experimental results obtained in a room simulating a free-field are shown and discussed.

Capítulo 6

The results of the application of the three acoustic actuators into the rectangular cavity are presented and the modal analysis performed. Analytical FRFs are compared with experimental and numerical results. Finalizing the Capítulo, the method presented in Capítulo 2 and Apêndice D is applied to an experimental pressure field and the particle velocity field obtained is analyzed.

Capítulo 7

This Capítulo presents the conclusions and perspectives.

The inertances are given by $M_i = \frac{\rho_0 L}{A}$ and the compliances by $C_i = \frac{V}{\rho_0 c^2}$. The dynamic set of equations will be obtained in two ways: in the first case the pressure will be used as the excitation variable and the volume velocity will be the response; in the second case the volume velocity will be the excitation variable and pressure the response variable. In the first case, the dynamic set of equations are found by application of the equilibrium of pressures (the mechanical analog of this dynamic formulation is shown in figure 2.2.4 (a)):

$$\begin{aligned}
 i\omega M_1 \hat{q}_1 + \frac{1}{i\omega} \frac{1}{C_1} \hat{q}_1 - \frac{1}{i\omega} \frac{1}{C_1} \hat{q}_2 &= \hat{p}_1 \\
 i\omega M_2 \hat{q}_2 - \frac{1}{i\omega} \frac{1}{C_1} \hat{q}_1 + \frac{1}{i\omega} \left(\frac{1}{C_1} + \frac{1}{C_2} \right) \hat{q}_2 - \frac{1}{i\omega} \frac{1}{C_2} \hat{q}_3 &= \hat{p}_2 \\
 i\omega M_3 \hat{q}_3 - \frac{1}{i\omega} \frac{1}{C_2} \hat{q}_2 + \frac{1}{i\omega} \frac{1}{C_2} \hat{q}_3 &= \hat{p}_3
 \end{aligned} \tag{2.2.10}$$

where $\hat{q}_{1,2,3}$ are the volume velocities in the pipes, and $\hat{p}_{1,2,3}$ the excitation pressures at the left side of each pipe. These equations are grouped and result in what would be called an *impedance* matrix system:

$$\left\{ i\omega \begin{bmatrix} M_1 & 0 & 0 \\ 0 & M_2 & 0 \\ 0 & 0 & M_3 \end{bmatrix} + \frac{1}{i\omega} \begin{bmatrix} \frac{1}{C_1} & -\frac{1}{C_1} & 0 \\ -\frac{1}{C_1} & \left(\frac{1}{C_1} + \frac{1}{C_2} \right) & -\frac{1}{C_2} \\ 0 & -\frac{1}{C_2} & \frac{1}{C_2} \end{bmatrix} \right\} \begin{Bmatrix} \hat{q}_1 \\ \hat{q}_2 \\ \hat{q}_3 \end{Bmatrix} = \begin{Bmatrix} \hat{p}_1 \\ \hat{p}_2 \\ \hat{p}_3 \end{Bmatrix} \tag{2.2.11}$$

The second formulation uses the mass conservation to write the dynamic set of equations (analog to the mechanical dynamic system shown in figure 2.2.4 (b)):

$$\begin{aligned}
 i\omega C_1 \hat{p}_1 + \frac{1}{i\omega} \left(\frac{1}{M_1} + \frac{1}{M_2} \right) \hat{p}_1 - \frac{1}{i\omega} \frac{1}{M_2} \hat{p}_2 &= \hat{q}_1 \\
 i\omega C_2 \hat{p}_2 - \frac{1}{i\omega} \frac{1}{M_2} \hat{p}_1 + \frac{1}{i\omega} \left(\frac{1}{M_2} + \frac{1}{M_3} \right) \hat{p}_2 &= \hat{q}_2
 \end{aligned} \tag{2.2.12}$$

Its matrix form can be expressed as:

$$\left\{ i\omega \begin{bmatrix} C_1 & 0 \\ 0 & C_2 \end{bmatrix} + \frac{1}{i\omega} \begin{bmatrix} \frac{1}{M_1} + \frac{1}{M_2} & -\frac{1}{M_2} \\ -\frac{1}{M_2} & \frac{1}{M_2} + \frac{1}{M_3} \end{bmatrix} \right\} \begin{Bmatrix} \hat{p}_1 \\ \hat{p}_2 \end{Bmatrix} = \begin{Bmatrix} \hat{q}_1 \\ \hat{q}_2 \end{Bmatrix} \quad (2.2.13)$$

Multiplied by $i\omega$, an *accelerance* matrix system is constructed:

$$\left\{ \begin{bmatrix} \frac{1}{M_1} + \frac{1}{M_2} & -\frac{1}{M_2} \\ -\frac{1}{M_2} & \frac{1}{M_2} + \frac{1}{M_3} \end{bmatrix} - \omega^2 \begin{bmatrix} C_1 & 0 \\ 0 & C_2 \end{bmatrix} \right\} \begin{Bmatrix} \hat{p}_1 \\ \hat{p}_2 \end{Bmatrix} = \begin{Bmatrix} i\omega \hat{q}_1 \\ i\omega \hat{q}_2 \end{Bmatrix} = \begin{Bmatrix} \hat{\dot{q}}_1 \\ \hat{\dot{q}}_2 \end{Bmatrix} \quad (2.2.14)$$

In (Arruda and Huallpa, 1999), this simple system is tested and this analytical solution (equation (2.2.13)) is compared to numerical and experimental results. Good agreement was obtained. A particularity of this *accelerance* formulation is that it "loses" the rigid body mode, which appears in the *impedance* formulation, as shown in (Augusztinovicz and Sas, 1996). This resulted from the decreasing of one degree of freedom.

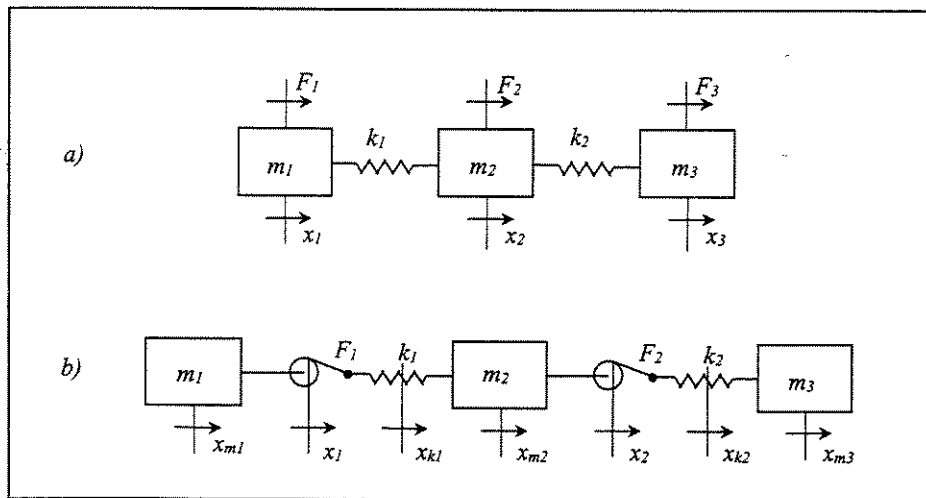


Figure 2.2.4 – Exhaust system mechanical analog

- a) Force as excitation variable and displacement as response variable
- b) Displacement as excitation variable and force as response variable

It should be noted that this last matrix formulation is more suitable for experimental validation as pressure (response variable) is easily measured with a microphone and volume acceleration (excitation variable) can be produced by loudspeakers in a specially designed configuration. The measurement of particle velocity has had great development in recent years and the development of a sensor called Microflowⁿ (Bree, 2000) is a proof of that. Although it still presents limitations in its frequency range, further developments can envisage the use of particle velocity probes as response and microphones as excitation transducers. Current practice of using the acceleration formulation in acoustic modal analysis would change to the impedance formulation, with the advantage of the miniaturization sensors such as the Microflowⁿ, leading to a transducer measuring particle velocity in the three directions with minimum interference on the acoustic field.

The analysis of an acoustic system with distributed parameters can be done using the finite element theory where the matrix dynamic system (Augusztinovicz and Sas, 1996) can be written:

$$\left[[H] + i\omega[C] + \omega^2[E] \right] \{p\} = \{\dot{q}\} \quad (2.2.15)$$

where $[H]$, $[C]$ and $[E]$ are usually referred as *acoustic mass matrix*, *acoustic damping matrix* and *acoustic stiffness matrix*, respectively, and their developments are shown in chapter 3. It must be clear that, as "force" (pressure) is the response variable and "displacement" (volume acceleration) the excitation variable, the analogy with mechanical systems, where these variables are used in an inverse way, is not direct. Therefore the use of "mass matrix", "damping matrix" and "stiffness matrix" make it easier the understanding of each term of the dynamic matrix system, but have poor physical meaning when direct analogy with mechanical systems is made.

2.3 – Inhomogeneous wave equation

In Appendix A, the linear homogeneous acoustic wave equation is developed for regions not containing acoustic sources. To take into account the presence of a source it is necessary to

include a source term in the fluid dynamic equations. There are several types of sources and three types (Fahy, 1995) will be considered here:

1) *Fluctuating volume (or mass) source* – in a certain region of the acoustic domain, an unsteady volume outflow of fluid is generated. The produced effect is a mass injection which is introduced into the linearized mass conservation equation (A.9):

$$\rho_0 \nabla \cdot \vec{V} + \frac{\partial \rho}{\partial t} = G(\vec{r}, t) \quad (2.3.1)$$

where $G(\vec{r}, t)$ is the rate of mass introduced per volume unit $\left(\frac{kg}{s \ m^3}\right)$. The inhomogeneous wave equation becomes:

$$\nabla^2 p - \frac{1}{c^2} \frac{\partial^2 p}{\partial t^2} = -\frac{\partial G(\vec{r}, t)}{\partial t} \quad (2.3.2)$$

The classical example of this type of source is the monopole point source (figure 2.3.1), where an omnidirectional sound field is generated. For any physical source to be an approximation of a monopole it has to produce an unsteady volume outflow from a region that is very small in comparison with the wavelength. Examples (Dowling, 1997) of sources working nearly as a monopole are: pulsating bubbles, sirens and unsteady combustion.

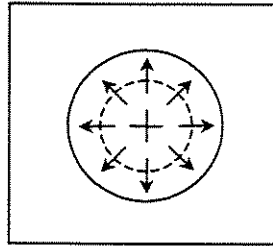


Figure 2.3.1 – Monopole oscillation

2) *Fluctuating force sources* – when there is a mechanism by which an external force acts on the fluid. In the linearized momentum equation (A.17) a new term is added:

$$\nabla^2 p + \rho_0 \frac{\partial \nabla \cdot \vec{V}}{\partial t} = \vec{F}(\vec{r}, t) \quad (2.3.3)$$

where $\vec{F}(\vec{r}, t)$ represents the external force vector per unit volume. The inhomogeneous wave equation becomes:

$$\nabla^2 p - \frac{1}{c^2} \frac{\partial^2 p}{\partial t^2} = \nabla \cdot \vec{F}(\vec{r}, t) \quad (2.3.4)$$

The most common examples of this type of source (Fahy, 1995) is an unsteady flow of fluid over a rigid surface, such as a turbulent boundary layer, or the impingement of an air jet on a solid body – being particularly the edges of such bodies effective sources.

3) *Fluctuating excess momentum sources* – it is a source associated with unsteady fluid flow in the absence of solid bodies (i.e., turbo-jet exhausts) (Fahy, 1995). It is a phenomenon not comprised in the basis of linearized fluid dynamic equations and has the particularity of being a very inefficient acoustic source.

Concerning the acoustic modal analysis, a punctual source is needed. Therefore, when dealing with experiments the source should present a monopole-like behavior in the frequency range of interest. As the subject is not a closed one, one of the aims of this work is the development of this type of source, and chapter 4 and 5 will discuss further this question.

2.4 – Mode shape visualization in acoustic systems

The acoustic mode shape visualization can be made using either the pressure or the particle displacement fields. In the three-dimensional case, the use of orthogonal plane slices allows the visualization of the entire volume. The particle displacement mode shape can be computed from the pressure mode shape in the wave number domain using the spatial Discrete Fourier Transform (two-dimensional DFT for two-dimensional fields and three-dimensional DFT for three-dimensional pressure fields). In the wave number domain it is straightforward to compute the pressure gradient which is related to the particle displacement by the Euler's relation. The difficulty with using the DFT is that its implicit *periodization* introduces high-frequency components that account for the sharp edges present in the *wrapped-around* data. This

phenomenon is known as *leakage*. In the data smoothing process, leakage is prejudicial, as it causes distortion of the low-pass filtered data. When dealing with acoustic modes this problem does not exist for rigid boundaries, but may become critical depending on the type of boundaries present. The usual way to reduce leakage is windowing, but this technique is not suitable in the case of finite length, spatial domain data. To overcome the leakage problem, a technique which consists of representing the data by a two-dimensional regressive discrete Fourier series (RDFS), proposed by Arruda (1992) can be used. In the application of this technique in chapter 6 and appendix D, the presence of rigid boundaries allowed the use of a simpler technique to avoid leakage. It was applied a data *mirroring* to achieve a periodic field, which is very efficient but has the disadvantage of doubling the data to be processed. Good references on the subject are (Mitchell et al., 1991) and (Sun and Mitchell, 1991).

Appendix D presents the application of the spatial DFT for one-, two- and three-dimensional acoustic fields. When using particle displacement mode shapes, there is no difficulty in visualizing modes in three-dimensions using a wire-frame representation, as it is usually done in structural modal analysis.

Chapter 3

Numerical and analytical modal analysis of a rectangular cavity

3.1 – Introduction

A classical, simple, and yet important case in the study of acoustics is the rectangular cavity (figure 3.1.1). The hypothesis of rigid boundaries leads to a well-known formulation, which is valuable in basic studies like the present work. This chapter is consecrated to the development of the analytical solution and to the development of a finite element model for a rectangular shallow cavity. Results of both approaches will be compared to experimental results and will be of great importance in the discussion of acoustic actuators performed in chapters 4 and 5.

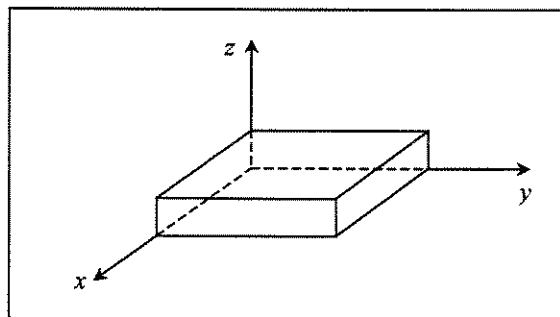


Figure 3.1.1 – Rectangular cavity

3.2 – Analytical solution

The departure hypothesis for the analytical formulation of the present problem is the rigid boundaries. In this case the normal particle velocity is null at the boundaries, and using the linearized Euler's relation (A.16) it results:

$$\begin{aligned}
 \left(\frac{\partial p}{\partial x}\right)_{x=0} &= \left(\frac{\partial p}{\partial x}\right)_{x=L_x} = 0 \\
 \left(\frac{\partial p}{\partial y}\right)_{y=0} &= \left(\frac{\partial p}{\partial y}\right)_{y=L_y} = 0 \\
 \left(\frac{\partial p}{\partial z}\right)_{z=0} &= \left(\frac{\partial p}{\partial z}\right)_{z=L_z} = 0
 \end{aligned} \tag{3.2.1}$$

The general solution can be written as a linear combination of each mode r (l, m, n):

$$p_r = \sum_r A_r \phi_r \tag{3.2.2}$$

where $\phi_r = \cos(k_{xl} x) \cos(k_{ym} y) \cos(k_{zn} z)$ is found from the variable separation method (Kinsler et al., 1982) and the boundary conditions, and A_r is the mode amplitude contribution. The l , m and n variables are integers representing the number of half wavelengths of the modes in x , y and z directions, respectively. The wave numbers are also determined by the boundary conditions:

$$\begin{aligned}
 k_{xl} &= \frac{l\pi}{L_x} & l &= 0, 1, 2, \dots \\
 k_{ym} &= \frac{m\pi}{L_y} & m &= 0, 1, 2, \dots \\
 k_{zn} &= \frac{n\pi}{L_z} & n &= 0, 1, 2, \dots
 \end{aligned} \tag{3.2.3}$$

Substitution of the analytical expression of the pressure,

$$p_{lmn} = A_{lmn} \cos(k_{xl} x) \cos(k_{ym} y) \cos(k_{zn} z) e^{i\alpha x} \tag{3.2.4}$$

into the homogeneous wave equation (A.19) gives the natural frequencies of vibration:

$$\omega_{lmn} = c \sqrt{\left(\frac{l\pi}{L_x}\right)^2 + \left(\frac{m\pi}{L_y}\right)^2 + \left(\frac{n\pi}{L_z}\right)^2} \quad (3.2.5)$$

The terms of the homogeneous wave equation can be written as:

$$\nabla^2 p = \frac{\partial^2 p}{\partial x^2} + \frac{\partial^2 p}{\partial y^2} + \frac{\partial^2 p}{\partial z^2} = -(k_{xl}^2 + k_{ym}^2 + k_{zn}^2) p_{lmn} = -\frac{\omega_{lmn}^2}{c^2} p_{lmn} \quad (3.2.6)$$

and

$$\frac{\partial^2 p}{\partial t^2} = -\omega^2 p_{lmn} \quad (3.2.7)$$

The general solution will be found by solving the inhomogeneous wave equation. The source term (a monopole excitation) in equation (2.3.2) is placed in the coordinates (x_0, y_0, z_0) and is mathematically written as:

$$d = D \delta(x_0, y_0, z_0) e^{i\omega t} \quad (3.2.8)$$

Combination of equations (2.3.2), (3.2.2), (3.2.6) and (3.2.7) gives the modal superposition equation for a certain circular frequency ω :

$$\sum_r \left(\frac{\omega^2 - \omega_r^2}{c^2} \right) A_r \phi_r = D \delta(x_0, y_0, z_0) \quad (3.2.9)$$

Multiplication of both sides of this equation by ϕ_n and integration in the three directions (x, y, z) results:

$$\sum_r \left(\frac{\omega^2 - \omega_r^2}{c^2} \right) A_r \int_0^{L_x} \int_0^{L_y} \int_0^{L_z} \phi_r \phi_n dx dy dz = D \int_0^{L_x} \int_0^{L_y} \int_0^{L_z} \delta(x_0, y_0, z_0) \phi_n dx dy dz \quad (3.2.10)$$

Application of the orthogonality property,

$$\int_0^{L_x} \int_0^{L_y} \int_0^{L_z} \phi_r \phi_n dx dy dz = 0 \quad \text{if } r \neq n \quad (3.2.11)$$

leads to a simplified equation:

$$\sum_r \left(\frac{\omega^2 - \omega_r^2}{c^2} \right) A_r \int_0^{L_x} \int_0^{L_y} \int_0^{L_z} \phi_r^2 dx dy dz = D \int_0^{L_x} \int_0^{L_y} \int_0^{L_z} \delta(x_0, y_0, z_0) \phi_r dx dy dz \quad (3.1.12)$$

where

$$\int_0^{L_x} \int_0^{L_y} \int_0^{L_z} \phi_r^2 dx dy dz = \int_0^{L_x} \int_0^{L_y} \int_0^{L_z} \cos^2(k_x x) \cos^2(k_y y) \cos^2(k_z z) dx dy dz \quad (3.2.13)$$

For the x direction, this integration results:

$$\int_0^{L_x} \cos^2\left(\frac{l\pi}{L_x} x\right) dx = \int_0^{L_x} \frac{1 + \cos 2\left(\frac{l\pi}{L_x} x\right)}{2} dx = \begin{cases} L_x & \text{if } l=0 \\ \frac{L_x}{2} & \text{if } l \neq 0 \end{cases} \quad (3.2.14)$$

The source term integral is developed:

$$D \int_0^{L_x} \int_0^{L_y} \int_0^{L_z} \delta(x_0, y_0, z_0) \phi_n dx dy dz = D \phi_n(x_0, y_0, z_0) = Q \left[\frac{kg}{m^3 s^2} m^3 = \frac{kg}{s^2} \right] \quad (3.2.15)$$

The pressure amplitude for each mode r is finally calculated for a certain frequency ω :

$$A_r = Q \frac{c^2}{I_r (\omega^2 - \omega_r^2)} \quad (3.2.16)$$

where

$$I_r = \int_0^{L_x} \int_0^{L_y} \int_0^{L_z} \phi_r^2 dx dy dz \quad (3.2.17)$$

The pressure in a point (x, y, z) of the acoustic domain is rewritten in a frequency notation:

$$\hat{p}(x, y, z, \omega) = \sum_{r=1}^{\infty} A_r \phi_r(x, y, z) \quad (3.2.18)$$

For an unit excitation of each mode r $\left(D = 1 \frac{kg}{m^3 s^2}\right)$ in a point (x_0, y_0, z_0) , the reconstructed pressure equation becomes the Frequency Response Function (FRF), and is written as:

$$\text{FRF}(x, y, z, \omega) = \sum_{r=1}^{\infty} \frac{\phi_r(x_0, y_0, z_0) \phi_r(x, y, z)}{\mu_r (\omega^2 - \omega_r^2)} \quad (3.2.19)$$

where $\mu_r = \frac{I_r}{c^2}$. The calculated FRF does not present though suitable units if experimental or numerical data are to be compared with. A multiplication by the fluid density is necessary for this sake:

$$\text{FRF}(x, y, z, \omega) = \sum_{r=1}^{\infty} \frac{\phi_r(x_0, y_0, z_0) \phi_r(x, y, z)}{\mu_r (\omega^2 - \omega_r^2)} \left[\frac{Pa}{kg/s^2} \right] \times \rho_0 \left[\frac{kg}{m^3} \right] = \text{FRF} \left[\frac{Pa}{m^3/s^2} \right] \quad (3.2.20)$$

This model represents the undamped case, and dissipation can be taken into account using the hypothesis of proportional damping (Ewins, 1984). The complex eigenvalues become:

$$\omega'_r = \omega_r \sqrt{1 + i\eta_r}, \quad (3.2.21)$$

where η_r is the damping loss factor (twice the viscous damping factor ζ_r) associated to each mode r . It must be clear that the assumption of proportional damping when comparing analytical results to experimental data is a good approximation for this case because, as shown in chapter 6, the constructed cavity walls are rigid and the dissipation caused by the friction with these walls can be considered equally distributed.

3.3 – Finite Element model

The construction of the finite element model will be based on (Kwon and Bang, 1997) and the central hypothesis here is that one dimension of the rectangular cavity is much smaller than the other two. The problem becomes two-dimensional for the range frequency below a cut-off frequency related to the first mode in the direction with smaller dimension. The chosen element is the linear triangular element for its simplicity.

The two-dimensional wave equation in the Cartesian system is:

$$\frac{\partial^2 p}{\partial x^2} + \frac{\partial^2 p}{\partial y^2} - \frac{1}{c^2} \frac{\partial^2 p}{\partial t^2} = d(x, y) \quad \text{in the two - dimensional domain } \Omega \quad (3.3.1)$$

The boundary conditions in Ω are:

$$p = \bar{p} \quad \text{on } \Gamma_e \quad (3.3.2)$$

and

$$\frac{\partial p}{\partial n} = \bar{q} \quad \text{on } \Gamma_n \quad (3.3.3)$$

where \bar{p} and \bar{q} express the pressure and partial derivative of pressure (proportional to particle velocity) in the normal direction, and n the normal vector pointing outward at the boundary. Γ_e and Γ_n are boundaries for essential and natural boundary conditions, and are related by the following relations:

$$\Gamma_e \cup \Gamma_n = \Gamma \quad \text{and} \quad \Gamma_e \cap \Gamma_n = \emptyset \quad (3.3.4)$$

The integrated weighted residuals of the differential equation and boundary condition are:

$$I = \int_{\Omega} w \left(\frac{\partial^2 p}{\partial x^2} + \frac{\partial^2 p}{\partial y^2} - \frac{1}{c^2} \frac{\partial^2 p}{\partial t^2} - d(x, y) \right) d\Omega - \underbrace{\int_{\Gamma} w \frac{\partial u}{\partial n} d\Gamma}_{=0} \quad (3.3.5)$$

The second term of the integrated weighted residual is null due to the boundary conditions (null normal particle velocity at the boundaries) for the rectangular cavity problem. The development of the weak formulation begins with the integration by parts of the first term inside integral:

$$\int_{\Omega} w \frac{\partial^2 p}{\partial x^2} d\Omega \quad (3.3.6)$$

In the two-dimensional domain, this integration is written:

$$\int_{y_1}^{y_2} \left(\int_{x_1}^{x_2} w \frac{\partial^2 p}{\partial x^2} dx \right) dy \quad (3.3.7)$$

where y_1 and y_2 are the minimum and maximum value of the domain in the y -axis as the strip dy (figure 3.3.1) along x moves in the y -axis.

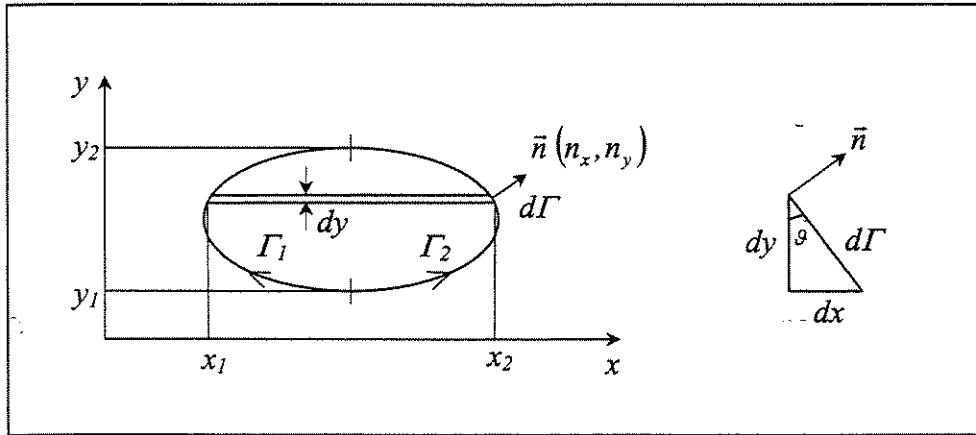


Figure 3.3.1 – Two-dimensional domain

From figure 3.3.1 it can be written:

$$dy = \cos(\vartheta) d\Gamma = n_x d\Gamma \quad (3.3.8)$$

The integration by parts in x results:

$$-\int_{y_1}^{y_2} \int_{x_1}^{x_2} \frac{\partial w}{\partial x} \frac{\partial p}{\partial x} dx dy + \int_{y_1}^{y_2} \left[w \frac{\partial p}{\partial x} \right]_{x_1}^{x_2} dy \quad (3.3.9)$$

Using the integration limits from the domain and the boundaries from figure 3.3.1, it results:

$$\int_{\Omega} \frac{\partial w}{\partial x} \frac{\partial p}{\partial x} d\Omega + \int_{\Gamma_2} w \frac{\partial p}{\partial x} n_x d\Gamma - \int_{\Gamma_1} w \frac{\partial p}{\partial x} n_x d\Gamma \quad (3.3.10)$$

where n_x is the x -component of the unit normal vector which is assumed positive in the outward direction. Combining the boundary integrals:

$$-\int_{\Omega} \frac{\partial w}{\partial x} \frac{\partial p}{\partial x} d\Omega + \oint_{\Gamma} w \frac{\partial p}{\partial x} n_x d\Gamma \quad (3.3.11)$$

where the boundary integral is in the counter-clockwise direction. The second term in the integral of (3.3.5) is developed in the same way as the first, giving:

$$-\int_{\Omega} \frac{\partial w}{\partial y} \frac{\partial p}{\partial y} d\Omega + \oint_{\Gamma} w \frac{\partial p}{\partial y} n_y d\Gamma \quad (3.3.12)$$

The integrated weighted residual is rewritten:

$$I = \int_{\Omega} \left(\frac{\partial w}{\partial x} \frac{\partial p}{\partial x} + \frac{\partial w}{\partial y} \frac{\partial p}{\partial y} \right) d\Omega + \oint_{\Gamma} w \frac{\partial p}{\partial n} d\Gamma - \frac{1}{c^2} \int_{\Omega} w \frac{\partial^2 p}{\partial t^2} d\Omega - \int_{\Omega} w d(x, y) d\Omega \quad (3.3.13)$$

where

$$\frac{\partial p}{\partial n} = \frac{\partial p}{\partial x} n_x + \frac{\partial p}{\partial y} n_y \quad (3.3.14)$$

The linear triangular element (figure 3.3.2) has three nodes (one in each vertice) and its variable interpolation within the element is linear in x and y :

$$p = a_1 + a_2x + a_3y \quad (3.3.15)$$

or

$$p = [1 \ x \ y] \begin{Bmatrix} a_1 \\ a_2 \\ a_3 \end{Bmatrix} \quad (3.3.16)$$

where $a_{1,2,3}$ are the constants to be determined.

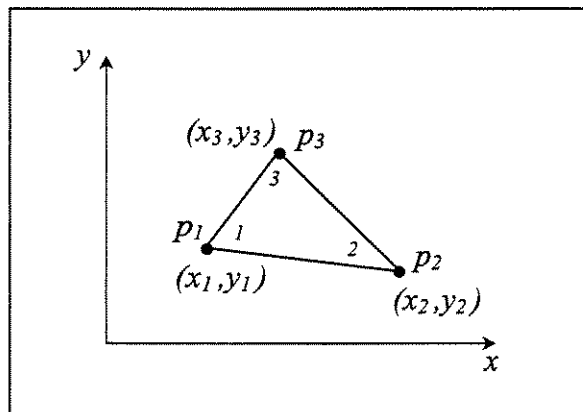


Figure 3.3.2 – Linear triangular element

The interpolation function (3.3.15) must represent the nodal variables in the three nodes. Substituting the x and y values at each nodal point gives:

$$\begin{Bmatrix} p_1 \\ p_2 \\ p_3 \end{Bmatrix} = \begin{bmatrix} 1 & x_1 & y_1 \\ 1 & x_2 & y_2 \\ 1 & x_3 & y_3 \end{bmatrix} \begin{Bmatrix} a_1 \\ a_2 \\ a_3 \end{Bmatrix} \quad (3.3.17)$$

Inversion of this matrix gives:

$$\begin{Bmatrix} a_1 \\ a_2 \\ a_3 \end{Bmatrix} = \frac{1}{2A} \begin{bmatrix} x_2y_3 - x_3y_2 & x_3y_1 - x_1y_3 & x_1y_2 - x_2y_1 \\ y_2 - y_3 & y_3 - y_1 & y_1 - y_2 \\ x_3 - x_2 & x_1 - x_3 & x_2 - x_1 \end{bmatrix} \begin{Bmatrix} p_1 \\ p_2 \\ p_3 \end{Bmatrix} \quad (3.3.18)$$

where

$$A = \frac{1}{2} \det \begin{bmatrix} 1 & x_1 & y_1 \\ 1 & x_2 & y_2 \\ 1 & x_3 & y_3 \end{bmatrix} \quad (3.3.19)$$

The magnitude of A is equal to the triangular element area. However its value is positive if the node numbering is in the counter-clockwise direction and negative otherwise.

Substitution of equation (3.3.18) into (3.3.16) gives:

$$p = SH_1(x, y)p_1 + SH_2(x, y)p_2 + SH_3(x, y)p_3 \quad (3.3.20)$$

where $SH_i(x, y)$ is the shape function for the linear triangular element and is given by:

$$\begin{aligned} SH_1 &= \frac{1}{2A} [(x_2y_3 - x_3y_2) + (y_2 - y_3)x + (x_3 - x_2)y] \\ SH_2 &= \frac{1}{2A} [(x_3y_1 - x_1y_3) + (y_3 - y_1)x + (x_1 - x_3)y] \\ SH_3 &= \frac{1}{2A} [(x_1y_2 - x_2y_1) + (y_1 - y_2)x + (x_2 - x_1)y] \end{aligned} \quad (3.3.21)$$

The shape functions satisfy the following conditions:

$$SH_i(x_j, y_j) = \delta_{ij} \quad (3.3.22)$$

and

$$\sum_{i=1}^3 SH_i = 1 \quad (3.3.23)$$

where δ_{ij} is the Kronecker delta:

$$\delta_{ij} = \begin{cases} 1 & \text{if } i = j \\ 0 & \text{if } i \neq j \end{cases} \quad (3.3.24)$$

The following approximation made by the finite elements will be based on the Galerkin method, where the weighting function w_i behaves as:

$$w_i = \frac{\partial p}{\partial a_i} \quad (3.3.25)$$

With this assumption, the weighting function w_i will be equal to the element shape function SH_i . The element acoustic mass matrix $[H^e]$, related to the term $\int_{\Omega} \left(\frac{\partial w}{\partial x} \frac{\partial p}{\partial x} + \frac{\partial w}{\partial y} \frac{\partial p}{\partial y} \right) d\Omega$, is constructed:

$$[H^e] = \int_{\Omega} \left(\frac{\partial w}{\partial x} \frac{\partial p}{\partial x} + \frac{\partial w}{\partial y} \frac{\partial p}{\partial y} \right) d\Omega = \int_{\Omega} \left(\begin{Bmatrix} \frac{\partial H_1}{\partial x} \\ \frac{\partial H_2}{\partial x} \\ \frac{\partial H_3}{\partial x} \end{Bmatrix} \left\{ \frac{\partial H_1}{\partial x} \frac{\partial H_2}{\partial x} \frac{\partial H_3}{\partial x} \right\} + \begin{Bmatrix} \frac{\partial H_1}{\partial y} \\ \frac{\partial H_2}{\partial y} \\ \frac{\partial H_3}{\partial y} \end{Bmatrix} \left\{ \frac{\partial H_1}{\partial y} \frac{\partial H_2}{\partial y} \frac{\partial H_3}{\partial y} \right\} \right) d\Omega \quad (3.3.26)$$

$$[H^e] = \begin{bmatrix} k_{11} & k_{12} & k_{13} \\ k_{21} & k_{22} & k_{23} \\ k_{31} & k_{32} & k_{33} \end{bmatrix} \quad (3.3.27)$$

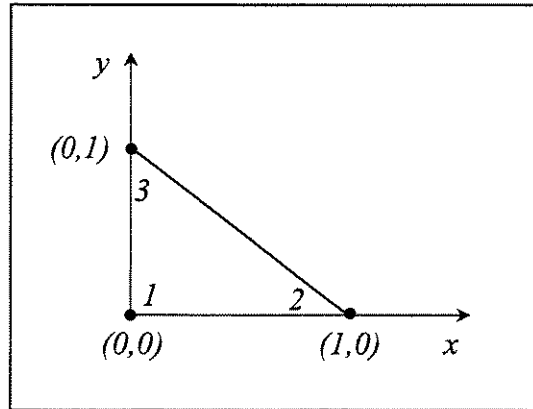


Figure 3.3.3 – Triangular element

Considering the triangular element as shown in figure 3.3.3, the constants are calculated:

$$k_{11} = \frac{1}{4A} [(x_3 - x_2)^2 + (y_2 - y_3)^2] \quad (3.3.28)$$

$$k_{12} = \frac{1}{4A} [(x_3 - x_2)(x_1 - x_3) + (y_2 - y_3)(y_3 - y_1)] \quad (3.3.29)$$

$$k_{13} = \frac{1}{4A} [(x_3 - x_2)(x_2 - x_1) + (y_2 - y_3)(y_1 - y_2)] \quad (3.3.30)$$

$$k_{21} = k_{12} \quad (3.3.31)$$

$$k_{22} = \frac{1}{4A} [(x_1 - x_3)^2 + (y_3 - y_1)^2] \quad (3.3.32)$$

$$k_{13} = \frac{1}{4A} [(x_1 - x_3)(x_2 - x_1) + (y_3 - y_1)(y_1 - y_2)] \quad (3.3.33)$$

$$k_{31} = k_{13} \quad (3.3.34)$$

$$k_{32} = k_{23} \quad (3.3.35)$$

$$k_{33} = \frac{1}{4A} [(x_2 - x_1)^2 + (y_1 - y_2)^2] \quad (3.3.36)$$

The time-dependent term in the integrated weighted residue $\left(\int_{\Omega} w \frac{\partial^2 p}{\partial t^2} d\Omega \right)$ will generate the element acoustic stiffness matrix $[E^e]$. The variable $p = p(x, y, t)$ is interpolated in the same way as done in the construction of the element acoustic mass matrix:

$$p(x, y, t) = \sum_{i=1}^n SH_i(x, y) p_i(t) \quad (3.3.37)$$

It is important to note that the shape function is used to interpolate the spatial variation over the element while the temporal variation is related to the nodal variable:

$$[E^e] = \int_{\Omega} \begin{Bmatrix} H_1 \\ H_2 \\ H_3 \end{Bmatrix} \{H_1 \ H_2 \ H_3\} d\Omega \begin{Bmatrix} \ddot{p}_1 \\ \ddot{p}_2 \\ \ddot{p}_3 \end{Bmatrix} \quad (3.3.38)$$

Solving this integral, it results:

$$[E^e] = \frac{A}{12} \begin{bmatrix} 2 & 1 & 1 \\ 1 & 2 & 1 \\ 1 & 1 & 2 \end{bmatrix} \quad (3.3.39)$$

The global acoustic stiffness and mass matrices are constructed from the grouping of the element matrices, so the mode shapes and natural frequencies can be determined. The constructed dynamic matrix system is:

$$[E] \{\ddot{p}\} + [H] \{p\} = \{D\} \quad (3.3.40)$$

The mode shapes are obtained from the homogenous system,

$$\{D\} = \{0\} \quad (3.3.41)$$

assuming an harmonic variation of the pressure:

$$\{p\} = \{\hat{P}\} e^{i\omega t} \quad (3.3.42)$$

Combination of (3.3.40), (3.3.41) and (3.3.42) produces:

$$([H] - \omega^2 [E]) \{\hat{P}\} e^{i\omega t} = \{0\} \quad (3.3.43)$$

The trivial solution of this system is:

$$\{\hat{P}\} = \{0\} \quad (3.3.44)$$

The natural frequencies ($\bar{\omega}_r^2$) are found from the determination of the non-trivial solution, given by:

$$|[H] - \omega^2 [E]| = 0 \quad (3.3.45)$$

Substitution of these natural frequencies into (3.3.45) determines the mode shape matrix $[\Psi_r]$ for each node of the system. The FRF is calculated from the non-homogeneous matrix system. Pressure and source harmonic variations are considered:

$$\{p\} = \{\hat{P}\} e^{i\omega t} \quad (3.3.46)$$

and

$$\{D\} = \{\hat{D}\} e^{i\omega t} \quad (3.3.47)$$

Substitution of (3.3.46) and (3.3.47) into (3.3.40) gives:

$$([H] - \omega^2[E])\{\hat{p}\} = \{\hat{D}\} \quad (3.3.48)$$

or

$$\{\hat{p}\} = ([H] - \omega^2[E])^{-1} \{\hat{D}\} \quad (3.3.49)$$

The FRF is finally calculated:

$$\text{FRF}_{ij} = \frac{\hat{P}_i}{\hat{D}_j} = ([H] - \omega^2[E])_{ij}^{-1} \quad (3.3.50)$$

or

$$\hat{P}_i = \sum_j ([H] - \omega^2[E])_{ij}^{-1} \hat{D}_j \quad (3.3.51)$$

This way of calculating the FRF demands a matrix inversion which can be strongly time-consuming if the number of nodes are high and the frequency range of interest is large (an inversion is needed for each analyzed frequency). An alternative method is presented in (Ewins, 1984) and exposed as follow.

Initially the matrices $[e_r]$ and $[h_r]$ are calculated:

$$[\Psi]^T [E] [\Psi] = [e_r] \quad (3.3.52)$$

and

$$[\Psi]^T [H] [\Psi] = [h_r] \quad (3.3.53)$$

These matrices can be called as *modal (or generalized) acoustic mass* and *stiffness of mode r*, respectively. The natural frequency matrix (a diagonal matrix) relates these matrices:

$$[\bar{\omega}_r^2] = [e_r]^{-1} [h_r] \quad (3.3.54)$$

A normalization of (3.3.53) and (3.3.54) is performed in what would be called an *acoustic mass-normalization*:

$$[\Phi]^T [E] [\Phi] = [I] \quad (3.3.55)$$

and

$$[\Phi]^T [H] [\Phi] = [\bar{\omega}_r^2] \quad (3.3.56)$$

The normalized *eigenvector* matrix is calculated:

$$[\Phi] = [\Psi] [e_r]^{-\frac{1}{2}} \quad (3.3.57)$$

From (3.3.51) it can be written:

$$\text{FRF}(\omega)^{-1} = ([H] - \omega^2 [E]) \quad (3.3.58)$$

Premultiplying both sides of this equation by $[\Phi]^T$ and posmultiplying it by $[\Phi]$, it results:

$$[\Phi]^T \text{FRF}(\omega)^{-1} [\Phi] = \underbrace{[\Phi]^T [H] [\Phi]}_{\{\omega_r^2\}} - \omega^2 \underbrace{[\Phi]^T [E] [\Phi]}_{[I]} \quad (3.3.59)$$

Premultiplication of (3.3.59) by $[\omega_r^2 - \omega^2]^{-1}$ gives:

$$[\omega_r^2 - \omega^2]^{-1} [\Phi]^T \text{FRF}(\omega)^{-1} [\Phi] = [I] \quad (3.3.60)$$

Premultiplication of the last equation by $[\Phi]$ results:

$$[\Phi] [\omega_r^2 - \omega^2]^{-1} [\Phi]^T \text{FRF}(\omega)^{-1} [\Phi] = [\Phi] \quad (3.3.61)$$

Finally, posmultiplicating (3.3.61) by $[\Phi]^T$, it produces:

$$[\Phi] [\omega_r^2 - \omega^2]^{-1} [\Phi]^T \text{FRF}(\omega)^{-1} \underbrace{[\Phi][\Phi]^T}_{[I]} = \underbrace{[\Phi][\Phi]^T}_{[I]} \quad (3.3.62)$$

The calculation of the FRF is simplified as the only inversion needed is of a diagonal matrix:

$$\text{FRF}(\omega) = [\Phi] [\omega_r^2 - \omega^2]^{-1} [\Phi]^T \quad (3.3.63)$$

Still, this FRF is not suitable for comparison with experimental results because their units are not the same. Below it is showed that the numerical FRF has the unit $[m^{-1}]$ and should be multiplied by the fluid density to be corrected.

In the inhomogeneous wave equation,

$$\nabla^2 p - \frac{1}{c^2} \ddot{p} = d \quad (3.3.64)$$

an area integration is done over the source term d , leading to the following unit:

$$\int_S d \left[\frac{kg}{m^3 s^2} \right] dS \times h = \left[\frac{kg}{s^2} \right] \quad (3.3.65)$$

where h is the dimension of the smaller dimension of the cavity.

In the same way, the matrices $[E]$ and $[H]$ are also integrated over the area and should be multiplied by the length h . The numerical FRF unit is readily calculated:

$$\frac{p[Pa]}{d[kg/s^2]} = \text{FRF}[m^{-1}] \quad (3.3.66)$$

To match the experimental units $\left[\frac{Pa}{m^3/s^2} = \frac{kg}{m^4} \right]$, the fluid density should multiply the numerical FRF:

$$\text{FRF} = \rho_0 \left[\frac{kg}{m^3} \right] \times \text{FRF}[m^{-1}] = \left[\frac{kg}{m^4} \right] \quad (3.3.67)$$

The approximated solution found with the finite element method was derived for the undamped case and, as in the analytical solution, a proportional damping will be assumed and numerical eigenvalues will be modified as in (3.2.21) to account for the energy dissipation.

This chapter starts with a brief revision of the duct theory for a better comprehension of the physics involved with the use of the tube – some analytical formulation will be of great importance in the development and validation of the actuator principles. The theoretical development of the two actuators is presented and their relative advantages and disadvantages are discussed.

4.2 – Duct theory revision

In the present application of the duct the main interest lays in a frequency range where only plane waves can propagate. In this condition an omnidirectional behavior of the acoustic radiated field from an open-ended tube is obtained for wavelengths much higher than the tube radius (Morse and Ingard, 1986). In (Kinsler et al., 1982) it is shown that the first non-planar mode of a rigid-walled circular waveguide has the following frequency:

$$f_{1,1} \approx \frac{101}{a} \quad (4.2.1)$$

where a is the radius of the tube (i.e., for a diameter of 1cm , as in the actuators developed here, this frequency is 20.2kHz).

If the termination of the tube is rigid, it can be considered that the *specific acoustic impedance* z ($= p/u$) is infinite and the incident wave is totally reflected. For an open-ended tube the common simplification of null impedance at the termination is not correct since the tube radiates sound into the surrounding medium. From the calculation of a baffled piston (Kinsler, 1982), the radiation impedance of a flanged open-ended tube (figure 4.2.1) for $\lambda \gg a$ ($ka \ll 1$) can be written:

$$z_{flanged} = \rho_0 c \left[\frac{1}{2}(ka)^2 + i \frac{8}{3\pi} ka \right] \quad (4.2.2)$$

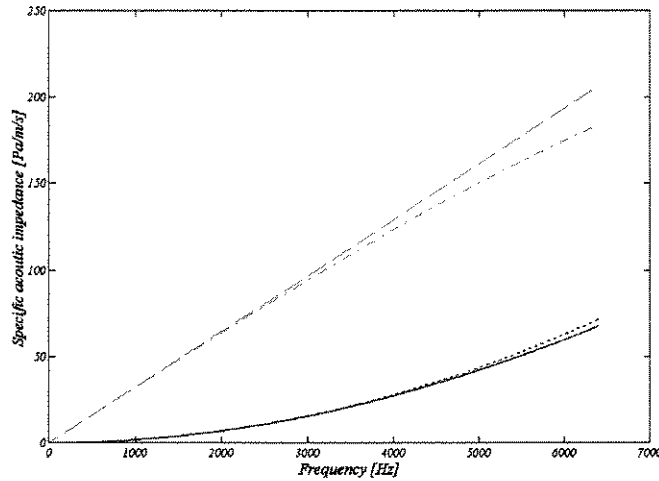


Figure 4.2.2 – Specific acoustic impedance
 (– – Reactance (low frequency assumption), – . – Reactance
 . . . Resistance (low frequency assumption), — Resistance)

The impedance for the unflanged open-ended tube (figure 4.2.3) for $ka \ll 1$ is given in (Kinsler et al., 1982) as:

$$z_{\text{unflanged}} = \rho_0 c \left[\frac{1}{4} (ka)^2 + i 0.6133 ka \right] \quad (4.2.4)$$

The complete formulation (for any ka) is developed in (Levine and Schwinger, 1948), where the exact end correction value of $0.6133a$ was for the first time calculated.

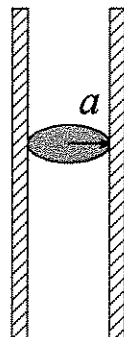


Figure 4.2.3 – Unflanged open-ended tube

An important detail when dealing with open-ended tubes at low frequencies (relative to the tube radius) is that the reflection coefficient is nearly -1 at the opened termination. When using two microphones for the determination of the incident and reflected wave amplitudes, small errors in this measurement can lead to wrong results for the pressure. As these waves have a phase difference of almost 180°, when calculating pressure a small value is found and may be of the order of the error of the instrumentation. The calculation of the particle speed from these amplitudes is less affected by the measurement errors as the incident and reflected amplitudes are almost in phase. It is interesting to note the fact that, while the particle velocity at the tube end is nearly doubled, the value of the pressure is very small, leading to a low transmitted power to the medium.

4.3 – One-microphone actuator

The use of cone loudspeakers in acoustic modal analysis has been a current practice for a long time. As the frequency range of interest is increasing in the recent years (i.e., high frequency analysis using statistical methods like SEA), the use of simple loudspeakers has become a factor that limits the experimental analysis (as they do not behave as rigid pistons at higher frequencies). At higher frequencies, the loudspeaker cone mode shapes make it difficult to characterize it as a calibrated sound source. In this context, a new generation of acoustic actuators appears (Van Tol and Verheij, 1993) in an attempt to fulfill the following requirements:

1. The source has to produce enough acoustic power;
2. Its frequency range must be much larger than that of the former actuators;
3. It has to behave as a monopole (i.e., omnidirectional directivity pattern) in this frequency range;
4. The source should be as much as possible independent of the surrounding medium it acts in. Thus requiring an acoustic impedance much higher than that of this medium.

The solution found was the use of high impedance loudspeakers called *drivers* in a special configuration. These units do not have good efficiency at low frequencies and are normally used

with a horn attached for a better performance in this frequency range. As acoustic actuators, the idea is to connect this loudspeaker to an instrumented socket by a flexible tube. The requirement of large power by the source in this case is fundamental, as it has to overcome the tube impedance and inject enough acoustic power into the medium.

The main advantage of this configuration is that an effective acoustic source behaving as monopole (remember from the previous discussion on ducts that the monopole behavior is dependent upon the relation between wavelength and duct radius) in larger frequency range is constructed with a tube with a cross-sectional area much smaller than the loudspeaker radiation area. Problems should be expected at low frequencies where both loudspeakers and radiation from a duct are inefficient. The solution for this problem may be the use of cone loudspeakers if the analyzed frequencies are low enough to match the frequency range where this loudspeaker behaves as a piston, or the use of large tube diameters working with a driver as described above. It is important to notice that the pressure measured in the socket will present peaks and dips related to the natural frequencies of the tube, but this behavior will be canceled out when the Frequency Response Functions are constructed.

One of the major concerns related to the one-microphone actuator application is the required independence of the surrounding impedance. In (Van Tol and Verheij, 1993) some critical situations were tested (i.e., the actuator was put close to a hard wall) and this requirement was fulfilled. A situation that can be seen as limit is that of a small reverberant cavity. In this case the cavity acoustic impedance may be of the order of the actuator impedance and this type of instrumentation (one microphone) may not be suitable. This is exactly what will be studied in this work: a small rectangular cavity with rigid walls will be tested and the performance of this actuator analyzed.

The constructed actuator makes use of a driver (figure 4.3.2) from *NOVIK* (model ND 2500), which has a nominal impedance of 8Ω at $1.2kHz$ with power of $50W_{RMS}$ above $500Hz$ and $70W_{RMS}$ above $1.2kHz$. Its frequency range of response is between $330Hz$ and $7.6kHz$.

A reinforced flexible tube $3m$ long and with a diameter of $12.7mm$ was used, and the socket (figure 4.3.1) had an inner diameter of $1cm$ and was instrumented with a $1/4"$ microphone from *The Modal Shop Inc.* put in a channel parallel to the main channel. The scheme showing the dimensions of this actuator is shown in appendix E.

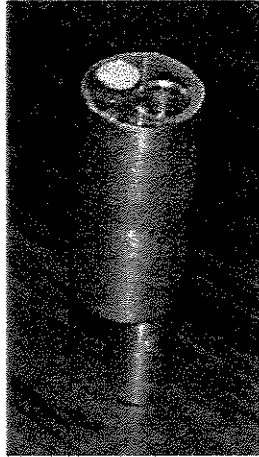


Figure 4.3.1 – Constructed socket

In what follows, the mathematical formulation is presented and the tests performed in an anechoic² room are discussed. These tests have the objectives of proving the monopole behavior and checking the analytical expressions for an unflanged tube radiating in a free-field.

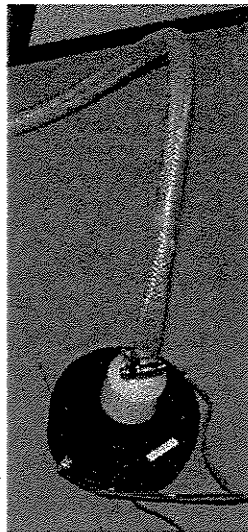


Figure 4.3.2 – Driver loudspeaker connected to the flexible tube

² The anechoic room is actually just a normal room of approximately $3 \times 3 \times 3 \text{m}$ with foam glued to the walls, ceiling, and floor. It is effective above approx. 400Hz in terms of sound absorption, but it is not mechanically isolated.

4.4 – Mathematical formulation

The pressure free field generated by a monopole (Kinsler et al., 1982) is:

$$p(r,t) = i\rho_0 ck \frac{Q}{4\pi r} e^{i(\omega t - kr)} \quad (4.4.1)$$

The complex source strength (Q), which represents the volume velocity at the mouth of the actuator, can be written as a function of the complex pressure amplitude at a distance r from the source:

$$Q = \hat{p}(r) \frac{4\pi r}{i\rho_0 ck} \quad (4.4.2)$$

As the directivity pattern of the radiation from a monopole is omnidirectional, a complex transfer function relating the pressure at r and the pressure at the source ($r = 0$) can be constructed:

$$\hat{H} = \frac{\hat{p}(r)}{\hat{p}(0)} \quad (4.4.3)$$

The source strength is rewritten:

$$Q = \hat{p}(0) \hat{H} \frac{4\pi r}{i\rho_0 ck} = \hat{p}(0) \hat{H} \frac{4\pi r}{i\rho_0 \omega} \quad (4.4.4)$$

The volume acceleration is readily calculated:

$$\dot{Q} = i\omega Q = \frac{4\pi r}{\rho_0} \hat{H} \hat{p}(0) \quad (4.4.5)$$

The monopole behavior is verified using the auto power spectral densities at the source ($G_{00} = \langle \hat{p}(0)^* \cdot \hat{p}(0) \rangle$) and at the distance r ($G_{rr} = \langle \hat{p}(r)^* \cdot \hat{p}(r) \rangle$), and the cross power spectral density between these two points ($G_{0r} = \langle \hat{p}(0)^* \cdot \hat{p}(r) \rangle$).

The transfer function can then be written:

$$\hat{H} = \frac{G_{0r}}{G_r} \quad (4.4.6)$$

The complex pressure amplitude at r is:

$$\hat{p}(r) = \hat{H} \hat{p}(0) \quad (4.4.7)$$

The auto power spectral density at r ,

$$G_r = \langle \hat{p}(r)^* \cdot \hat{p}(r) \rangle = |\hat{H}|^2 G_{00} \quad (4.4.8)$$

will be compared to the direct measurement at r , and the agreement between these two values will indicate whether the source behaves as a monopole or not.

4.5 – Experimental validation

The experiments took place in a small anechoic room (figure 4.5.1), behaving as a free-field above 400Hz approximately.

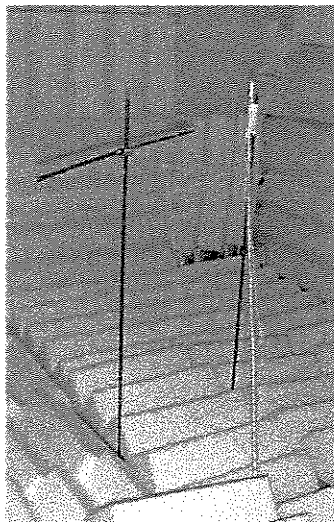


Figure 4.5.1 – Experiment in a room simulating a free-field

In the present work, all measurements were acquired using a measurement system from HP (model 35650). The source was excited with a continuous random noise output type and the signal was acquired using a Hanning window, 3200 frequency lines and 30 averages.

Figure 4.5.2 shows schematically the locations where measurements were made. The odd locations are 21.8cm far from the source and the even locations 40cm.

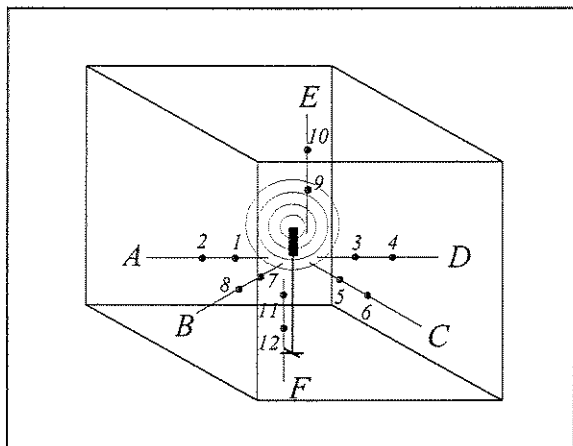


Figure 4.5.2 – Measurement locations

Figure 4.5.3 shows the results for the response of one microphone located 21.8cm from the source. Figure 4.5.4 presents the power spectral densities for five different locations far 21.8cm from the source.

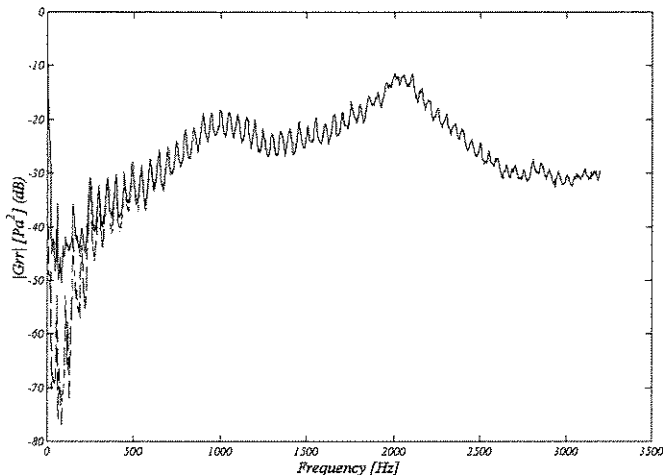


Figure 4.5.3 – Auto power spectral densities (21.8cm far from the source)
 (— measured, - - calculated from the source measurement)

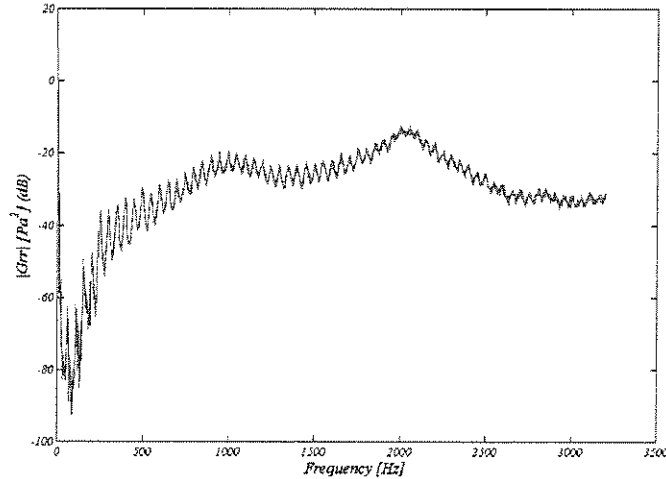


Figure 4.5.4 – Auto power spectral densities in 5 points (all located 21.8cm far from the source)

In all measurements there was good agreement between the power spectral densities calculated from the source measurement and the direct measurement. The coincident curves (figure 4.5.4) for different locations equally spaced from the source prove the monopole behavior (the same results were obtained for a distance of 40cm from the source). The bad results at frequencies lower than 400Hz are due to the room's cut-off frequency (400Hz) and the poor efficiency of the actuator below 300Hz. The transfer function \hat{H} was constructed using a microphone placed 0.2m from the socket mouth and it is showed in figure 4.5.5. This result will be used in chapter 6 where the one-microphone actuator is applied to the rectangular cavity.

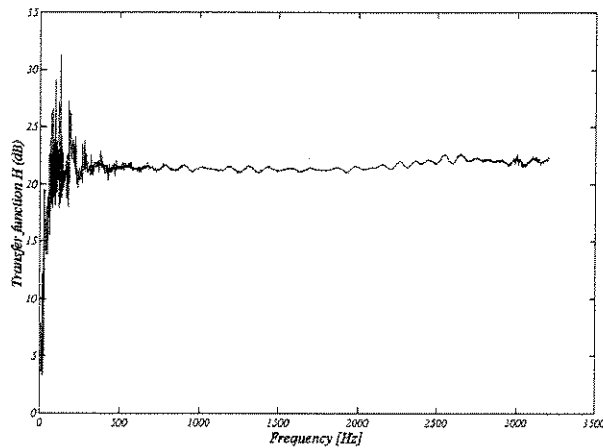


Figure 4.5.5 – Transfer function H constructed ($r = 0.2m$)

Using the acoustic impedance for unflanged tube (4.2.2) applied to the pressure measured at the socket in a free-field, it is, in principle, possible to calculate the volume acceleration:

$$\dot{Q} = i\omega \frac{\hat{p}(0)}{\hat{z}_{unflanged}} S \quad (4.4.9)$$

where S is the cross-sectional area of the socket. From (4.4.2) the volume acceleration for a monopole depends on the distance r to the source and the pressure at r :

$$\dot{Q} = \frac{4\pi r}{\rho_0} \hat{p}(r) \quad (4.4.10)$$

Also, the active power injected (the derivation of the following equation can be found in appendix B) can be calculated:

$$P_a = \frac{1}{2} \text{Re}\{p u^*\} S \quad (4.4.11)$$

where S denotes area (πa^2 for the tube throat, and $4\pi r^2$ for the distance r from the source) and $*$ the complex conjugate. Figures 4.5.6 and 4.5.7 show the comparison between volume acceleration and active power calculated from the pressure measured 40cm (use of the monopole theory. Appendix C presents the deduction of the acoustic specific impedance for a spherical wave diverging from a point source, used to find the particle speed at r) from the source and from the pressure at the socket (use of the radiation impedance for unflanged tube).

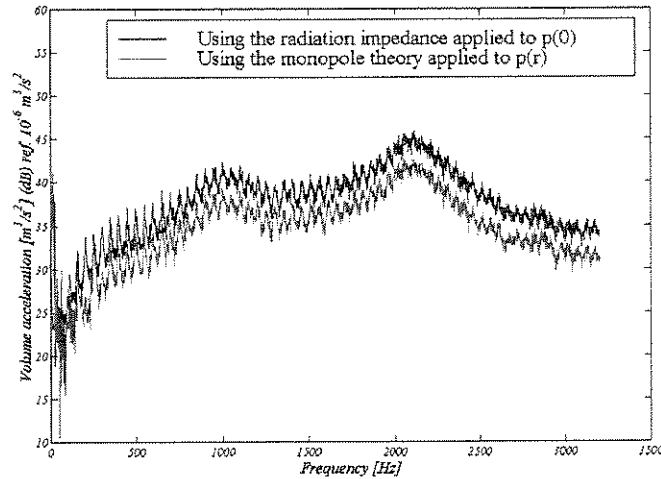


Figure 4.5.6 – Volume acceleration comparison ($r = 0.40m$)

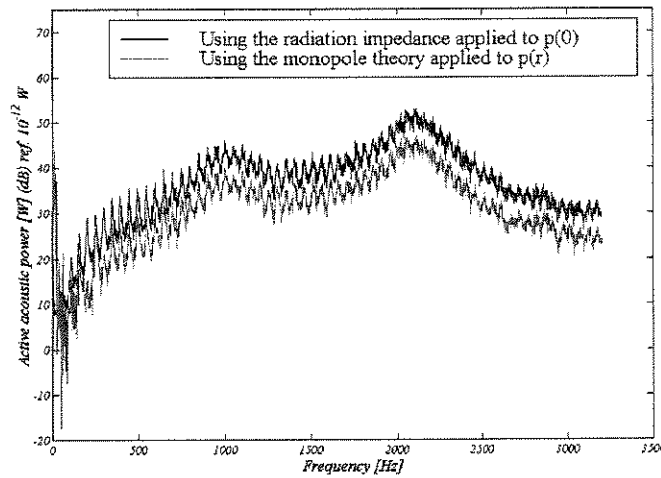


Figure 4.5.7 – Active power comparison ($r = 0.40m$)

It can be seen from these last two figures that the curves are very similar but shifted by a constant. This is due to the position of measurement microphone inside the tube (figure 4.5.8), which is $4.5mm$ (if it is considered that the measured pressure is located at the center of the hole connecting the microphone channel to the main channel) far from the termination. As the pressure decreases very fast in this region (almost a pressure antinode), even a small distance as the one used will not give the correct pressure. For this configuration (tube length and diameter,

and position of measurement inside the tube) it was found that the pressure should be divided by two in order to have a better estimation of the real pressure at the tube termination. Figures 4.5.9 and 4.5.10 show the results using this correction

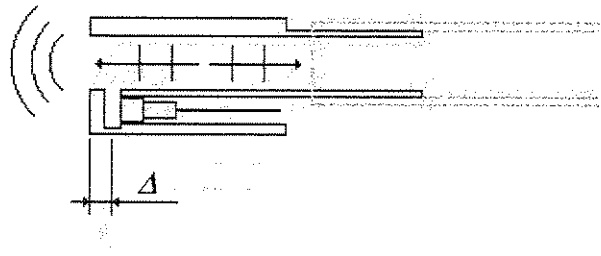


Figure 4.5.8 – Microphone positioning inside the socket

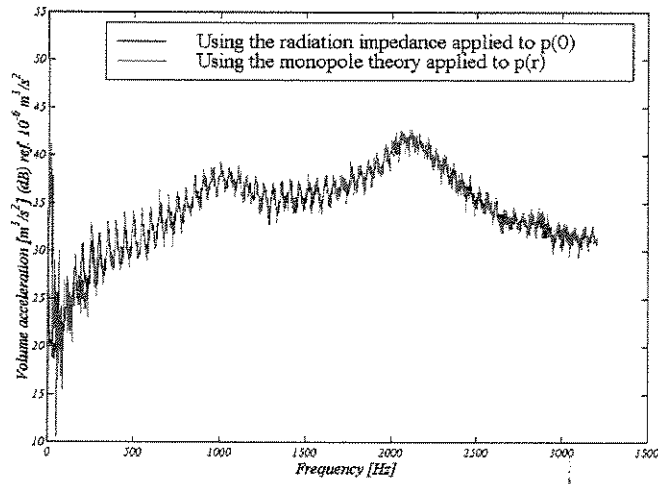


Figure 4.5.9 – Volume acceleration comparison ($r = 0.40m$) with correction

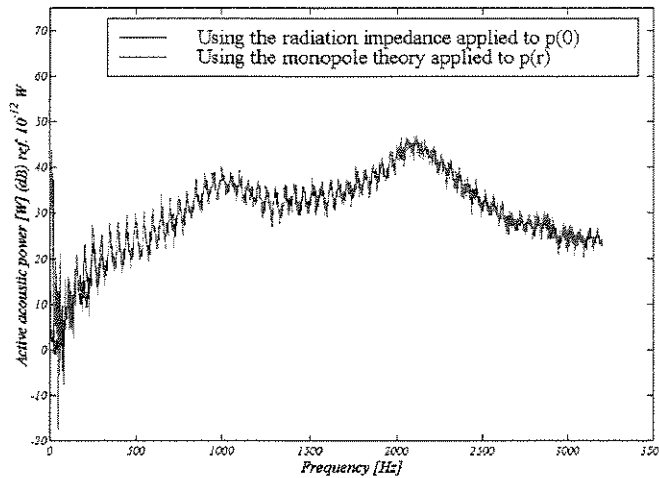


Figure 4.5.10 – Active power comparison ($r = 0.40m$) with correction

Applying the correction, the curves present excellent agreement and it is important to note that the use of the radiation impedance leads to a better result at low frequencies. This is an important result since it shows that the use of the radiation impedance is possible when the medium is approximately a free-field. This procedure has also the advantage that it does not require the construction of the complex calibration transfer function \hat{H} . The need for this transfer function is disadvantageous since it depends on the quality of the anechoic room used in the calibration of the source and normally it will present poor results at low frequencies. Also, it should be measured again if the tube length or the diameter is changed, thus decreasing the flexibility of utilization of this device.

The use of the radiation impedance in a medium presenting a very reverberant behavior will be discussed in chapter 6. It will be shown that the use of the radiation impedance gives the same results as the use of the transfer function \hat{H} , with the advantages discussed in the precedent paragraph. Nevertheless, both results are inaccurate, and the development of a more reliable actuator using two microphones presented in the next chapter is of great importance.

Chapter 5

Two-microphone acoustic actuator development

5.1 – Introduction

The development of the one-microphone actuator presented in the precedent chapter was based in the principle that the acoustic impedance of this type of actuator is so high that any practical surrounding it would act in can be treated as a free-field. This is true for many cases and the wide spread use of this type of actuator nowadays can be considered as a proof of it. However, if a more general application is required, an actuator with a more robust conception must be developed. In this sense, the use of two microphones can be a good idea if the physical principles working in this device are carefully analyzed. The basic concept of the following development derives from the fact that there can only exist plane waves in the actuator tube for a quite large (depending on its diameter) frequency range. In this case, the pressure can be considered constant along the tube cross-section and the use of two microphones would, in principle, allow the calculation of the amplitudes of the waves going outward and inward the socket. If this calculation is made successfully, a method for the calculation of the volume acceleration can be derived with the important advantage of not depending upon the strong assumption that the surrounding impedance can be ignored.

The same sequence adopted in the development of the one-microphone actuator will be followed here. The mathematical formulation is presented and then results from the anechoic³ room tests are shown and discussed. Also, the capability of measuring the active acoustic power (active intensity times area) injected into the surrounding, which is of interest for experimental SEA, for example, is explored. It will be shown that the active acoustic power calculation using two microphones presents problems and has a limited frequency range

5.2 – Mathematical formulation

If the frequency range of analysis does not allow the existence of modes in the cross-section plane of the tube, only plane waves can exist. So, the pressure can be split into two components related to the inward (with amplitude B) and outward (with amplitude A) waves. In the frequency domain it can be written:

$$p(\omega) = A(\omega) e^{-ikx} + B(\omega) e^{ikx} \quad (5.2.1)$$

Supposing the reference ($x=0$) at the microphone 1 (figure 5.2.1):

$$p_1(\omega) = A(\omega) + B(\omega) \quad (5.2.2)$$

$$p_2(\omega) = A(\omega) e^{ik\Delta_1} + B(\omega) e^{-ik\Delta_1} \quad (5.2.3)$$

The wave amplitudes are then calculated:

$$B(\omega) = \frac{p_1(\omega) e^{ik\Delta_1} - p_2(\omega)}{2i \sin(k\Delta_1)} \quad (5.2.4)$$

³ The anechoic room is actually just a normal room of approximately 3x3x3m with foam glued to the walls, ceiling, and floor. It is effective above approx. 400Hz in terms of sound absorption, but it is not mechanically isolated.

where Δ_l is distance between the microphones.

$$A(\omega) = p_1(\omega) - B(\omega) = \frac{p_2(\omega) - p_1(\omega) e^{-ik\Delta_l}}{2i \sin(k\Delta_l)} \quad (5.2.5)$$

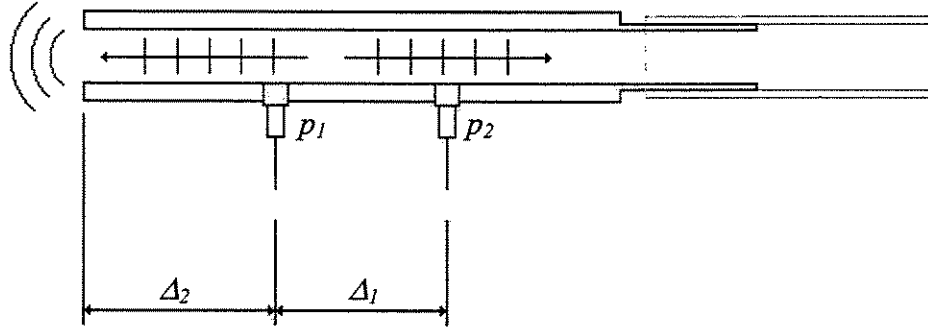


Figure 5.2.1 – Traveling waves and microphone positioning in the socket

The pressure at the socket mouth is readily deduced:

$$p_{\text{exit}}(\omega) = A(\omega) e^{-ik\Delta_2} + B(\omega) e^{ik\Delta_2} \quad (5.2.6)$$

Applying the Euler's relation into (5.2.1), the particle velocity is found:

$$u(\omega) = \frac{1}{\rho_0 c} [A(\omega) e^{-ikx} - B(\omega) e^{ikx}] \quad (5.2.7)$$

The volume acceleration at the socket mouth becomes:

$$\dot{Q} = \frac{i\omega}{\rho_0 c} [A(\omega) e^{-ik\Delta_2} - B(\omega) e^{ik\Delta_2}] S \quad (5.2.8)$$

where S is the cross-sectional area of the socket.

The Auto and Cross Power Spectral Densities related to A and B can be found from equations (5.2.4) and (5.2.5):

$$S_{AA} = \langle A^* \cdot A \rangle = \frac{S_{11} + S_{22} - 2\cos(k\Delta_1)\text{Re}\{S_{12}\} + 2\sin(k\Delta_1)\text{Im}\{S_{12}\}}{4\sin^2(k\Delta_1)} \quad (5.2.9)$$

$$S_{BB} = \langle B^* \cdot B \rangle = \frac{S_{11} + S_{22} - 2\cos(k\Delta_1)\text{Re}\{S_{12}\} - 2\sin(k\Delta_1)\text{Im}\{S_{12}\}}{4\sin^2(k\Delta_1)} \quad (5.2.10)$$

$$S_{AB} = \langle A^* \cdot B \rangle = \frac{S_{11}e^{i2k\Delta_1} - S_{22} - 2ie^{ik_1\Delta_1}\text{Im}\{S_{12}\}}{4\sin^2(k\Delta_1)} \quad (5.2.11)$$

Using the equations (5.2.1) and (5.2.7), and the three relations above, the Auto and Cross Power Spectral Densities related to pressure and particle velocity at a position x inside the tube are written:

$$S_{pp} = \langle p(x)^* \cdot p(x) \rangle = S_{AA} + S_{BB} + 2\cos(2kx)\text{Re}\{S_{AB}\} - 2\sin(2kx)\text{Im}\{S_{AB}\} \quad (5.2.12)$$

$$S_{uu} = \langle u(x)^* \cdot u(x) \rangle = \frac{S_{AA} + S_{BB} - 2\cos(2kx)\text{Re}\{S_{AB}\} + 2\sin(2kx)\text{Im}\{S_{AB}\}}{(\rho_0 c)^2} \quad (5.2.13)$$

$$S_{pu} = \langle p(x)^* \cdot u(x) \rangle = \frac{S_{AA} - S_{BB} - 2i\sin(2kx)\text{Re}\{S_{AB}\} - 2i\cos(2kx)\text{Im}\{S_{AB}\}}{\rho_0 c} \quad (5.2.14)$$

The main problem associated with the use of the two-microphone technique (Jacobsen, 1989) is the phase mismatch between the two filtered and amplified signals. Since volume acceleration and, as will be seen later in this chapter, the intensity depend on A and B , they will be affected by this phase mismatch between the two chains of measurement. The method used here for the phase correction is the *microphone switching technique*. This technique requires an extra measurement made where the microphones have their positions switched for the phase mismatch correction and is described below. It is a technique specially suited for the present case

as it can be guaranteed that the positions of the inverted microphones correspond exactly to the microphones positions before the inversion. The disadvantage of the technique in this case is that it is necessary to double the number of measurements. In (Sas, 2000) an alternative approach called *transfer function method* which avoid the necessity of doubling the number of measurements is presented. The methodology consists basically on exposing the two microphones to the same acoustic field and measuring directly the phase shift between them. However, this method relies on a perfectly behavior of the microphones and do not compensate for different environmental conditions and non-linearities. In (Chung, 1978) it is shown a technique which in principle eliminates the phase mismatch when calculating the active intensity based on the finite difference method by taking the geometric average of the Cross Spectral Density between the microphones. In the present work this methodology was used to correct S_{12} and, with this new value, the correct active acoustic power (section 5.5) was calculated. The result (figure 5.5.11) is in agreement with the results from arithmetic average, proving the validity of this last technique.

Below, the microphone switching technique using the arithmetic average is described. It will be shown that if the phase shift between the two chains of measurements is small, the arithmetic average of the waves amplitudes (A and B) calculated with the original microphone and switched positioning gives the correct phase angle.

The phase difference between the two measurement chains (of p_1 and p_2) is written as:

$$\phi_r = \phi_1 - \phi_2 \quad (5.2.15)$$

where ϕ_1 and ϕ_2 are the phase shift introduced by the measurement chains of microphones 1 and 2, respectively. Taking microphone 2 as a reference ($\phi_2 = 0$), it can be written:

$$p_1 = P_1 e^{i\phi_r} \quad (5.2.16)$$

$$p_2 = P_2 \quad (5.2.17)$$

The measurement with the switched microphones gives:

$$p_1^s = P_1 \quad (5.2.18)$$

$$p_2^s = P_2 e^{i\phi_r} \quad (5.2.19)$$

The wave amplitude B (equation (5.2.4)) is calculated using the original and switched microphone configuration measurements:

$$B = \frac{P_1 e^{i(k\Delta_1 + \phi_r)} - P_2}{2i \sin(k\Delta_1)} \quad (5.2.20)$$

$$B^s = \frac{P_1 e^{ik\Delta_1} - P_2 e^{i\phi_r}}{2i \sin(k\Delta_1)} \quad (5.2.21)$$

Application of the arithmetic average between these two amplitudes results:

$$\frac{B + B^s}{2} = \frac{(e^{i\phi_r} + 1) P_1 e^{ik\Delta_1} - P_2}{2 \cdot 2i \sin(k\Delta_1)} \quad (5.2.22)$$

For small phase shift between the two measurement chains $e^{i\phi_r}$ is approximately 1 and a corrected amplitude is found:

$$B_{corrected} = \frac{B + B^s}{2} \approx \frac{P_1 e^{ik\Delta_1} - P_2}{2i \sin(k\Delta_1)} \quad (5.2.23)$$

For the outward wave amplitude, the same procedure can be followed. Taking the two measurements,

$$A = \frac{P_2 - P_1 e^{i(-k\Delta_1 + \phi_r)}}{2i \sin(k\Delta_1)} \quad (5.2.24)$$

$$A^s = \frac{P_2 e^{i\phi_r} - P_1 e^{-ik\Delta_1}}{2i \sin(k\Delta_1)} \quad (5.2.25)$$

and applying the arithmetic average,

$$\frac{A + A^s}{2} = \frac{(e^{i\phi_r} + 1) P_2 - P_1 e^{-ik\Delta_1}}{2 \cdot 2i \sin(k\Delta_1)} \quad (5.2.26)$$

it can be found a corrected amplitude if the phase shift between the two microphones is small:

$$A_{corrected} = \frac{A + A^{inv}}{2} \approx \frac{P_2 - P_1 e^{-ik\Delta_1}}{2i \sin(k\Delta_1)} \quad (5.2.27)$$

An experimental estimate of the phase shift between microphones 1 and 2 was made in order to verify the error when using the arithmetic average. Taking the Cross Spectral Density between the two microphones in the original and switched configurations it can be written:

$$S_{12} = S_{12}^{correct} e^{i(\phi_2 - \phi_1)} \quad (5.2.28)$$

and

$$S_{12}^s = S_{12}^{correct} e^{i(\phi_1 - \phi_2)} \quad (5.2.29)$$

Dividing this two equations,

$$\frac{S_{12}^s}{S_{12}} = e^{i2(\phi_1 - \phi_2)} \quad (5.2.30)$$

and the phase shift can be estimated:

$$\phi_1 - \phi_2 = \frac{1}{2} \tan^{-1} \left(\frac{S_{12}^s}{S_{12}} \right) \quad (5.2.31)$$

Figure 5.2.2 shows the phase shift for a large range of frequency (0-6.4kHz).

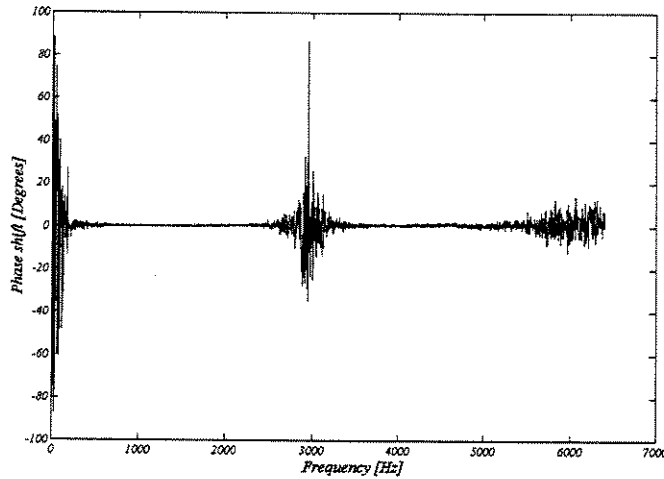


Figure 5.2.2 – Estimate of phase shift between microphones 1 and 2

The amplitude $(e^{i\phi} + 1)/2$ that appears in the arithmetic average of A and B is plotted in figure 5.2.3 using the estimate of the phase shift presented above. Except in the very low frequency range and in a region of approximately $3kHz$, the results approximate unity and prove that the use of the arithmetic average is reasonable. At $2.8kHz$, the phase difference between the microphones is 90° and, as the amplitude difference is maximum, the calculation is sensitive to small errors in the sensors.

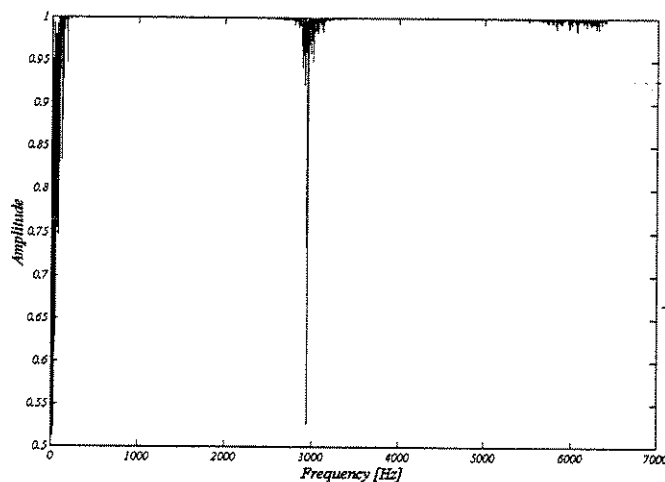


Figure 5.2.3 – Amplitude $(e^{i\phi} + 1)/2$ using the estimate of the phase shift

5.3 – Experimental validation

The constructed socket (figure 5.3.1) has the following dimensions:

□ *Microphone separation distance Δ_1*

When the phase difference approaches 180° , the calculation of A and B becomes highly sensitive to small phase and amplitudes measurements errors as the denominator tends to zero. Regarding this question, the microphones should be as close as possible. Nevertheless, when measuring low frequencies the phase difference between the microphones is small and if they are too close to each other small phase measurement errors become very important. The compromise found was a distance of 30mm . For the lower frequency of 300Hz the phase difference is 5° and for a maximum frequency of 5kHz it is 80° . With this separation distance, the phase difference becomes 180° at 5717Hz and this is the critical frequency of analysis.

□ *Socket diameter*

The tube used has an inner diameter of 12.7mm and the socket an inner diameter of 10mm . The first non-planar (equation (4.2.1)) mode will occur at 20.2kHz and the hypothesis of plane waves in the frequency range of analysis is fulfilled.

□ *Distance Δ_2 to the socket mouth*

The microphone 1 was put 56mm far from the socket mouth. This was done in an attempt to avoid edge effects influencing the calculation of A and B .



Figure 5.3.1 – Two-microphone actuator socket constructed

The same tube and driver used in the one-microphone actuator are used here. The microphones in this new configuration were put perpendicular to the socket and the measured pressure is considered to be related to the center of the microphones. The scheme showing the dimensions of this actuator is presented in appendix E.

Following, the analysis of volume acceleration and active acoustic power will be carried out separately. Both values will be compared to a measurement made in a distance r from the source, as done for the one-microphone actuator.

5.4 – Volume acceleration

In this section the experimental results for the volume acceleration obtained using A and B (equation (5.2.8)) are compared to the results of the monopole theory applied to a pressure measured at a distance r from the source (equation (4.4.10)). Figure 5.4.1 shows this comparison for the frequency range of 0 to 3.2kHz.

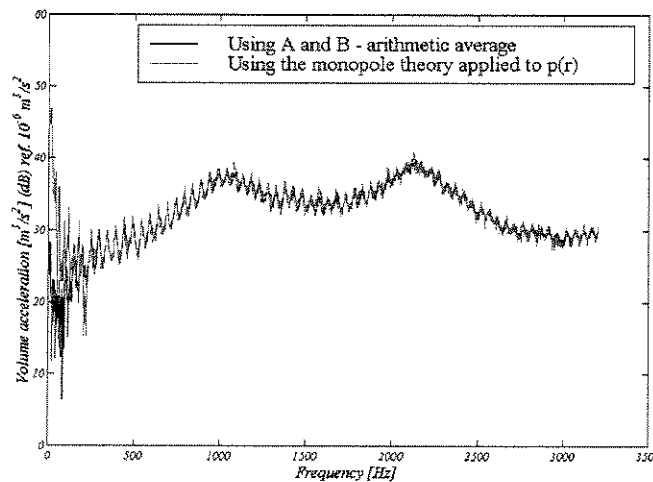


Figure 5.4.1 – Comparison between volume acceleration calculated from A and B (arithmetic average) and from the monopole theory applied to $p(r = 0.40m)$ – 0 to 3.2kHz

There is a very good agreement between the curves, but it can be noticed that in some very localized points the difference can be of the order of $2dB$. Figure 5.4.2 shows a zoom of the precedent figure and these localized points where there are some differences can be notice more clearly. The origins of this error are very difficult to identify and can be related to the quality of the microphones and the anechoic room, which could introduce excessive noise in the measurements, or even to random errors associated to the estimation of the Cross Power Spectral Densities.

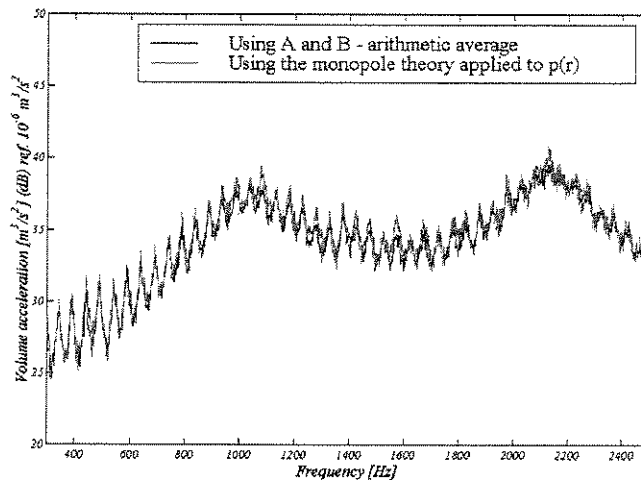


Figure 5.4.2 – Comparison between volume acceleration calculated from A and B (arithmetic average) and from the monopole theory applied to $p(r = 0.40m)$ – 300 to 2500Hz

Figure 5.4.3 shows, for a wide range of frequencies (0-6.4kHz), the volume acceleration calculated without making the arithmetic average. The results from the original configuration and with the switched microphones agree quite well below 3kHz, but start to diverge from this frequency. The more the frequency grows and approximates to a value where $k\Delta_l$ equals 180° (5.7kHz), the more equations (5.2.4) and (5.2.5) are sensitive to small errors in phase and amplitude. It is interesting to note that the result at a distance r seems to be the arithmetic average between the two configurations for most of this perturbed region. Figure 5.4.4 shows the result from the arithmetic average and, with the exception of the region close to 5.7kHz, it is in good agreement with the measurement at r .

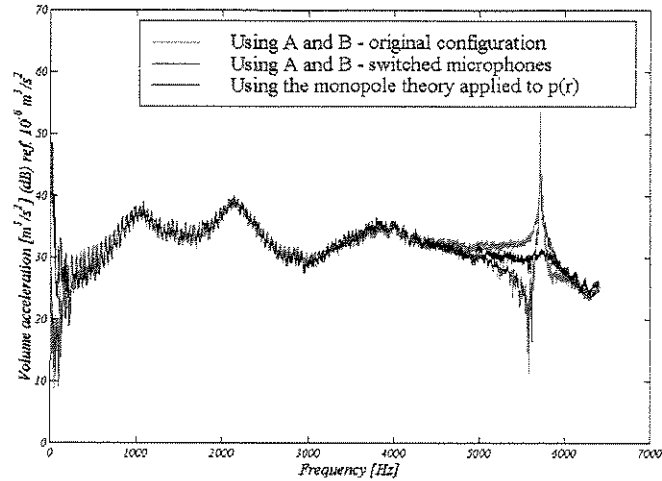


Figure 5.4.3 – Comparison between volume acceleration calculated from A and B (arithmetic average) and from the monopole theory applied to $p(r = 0.40m)$ – 0 to 3.2kHz

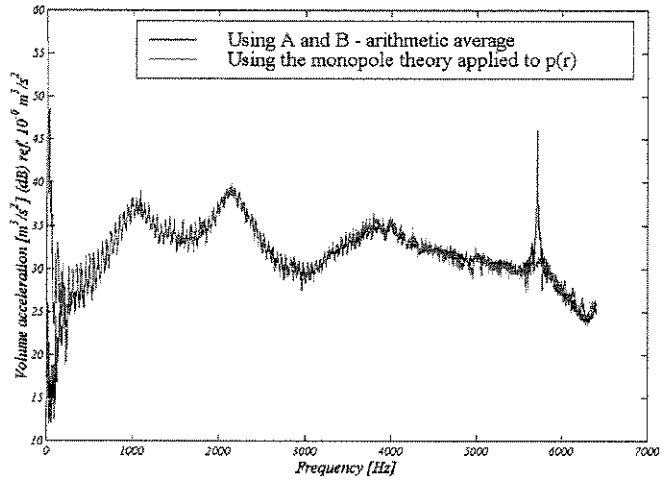


Figure 5.4.4 – Comparison between volume acceleration calculated from A and B (arithmetic average) and from the monopole theory applied to $p(r = 0.40m)$ – 0 to 6.4kHz

A question that will arise in the next section is related to the distance Δ_2 (from p_1 to the socket mouth). All the microphone area was exposed in the measurement and it was supposed that the pressure measured was the pressure at the center of this area. Considering this hypothesis,

A and B were constructed and figure 5.4.5 shows the variation of the volume acceleration near the socket mouth (from $\Delta_2 = 0.060m$ to $\Delta_2 = 0.065m$, position of the socket mouth).

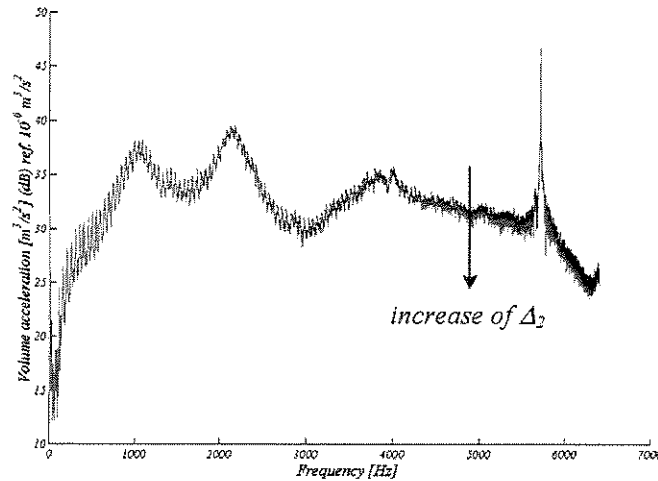


Figure 5.4.5 – Volume acceleration calculated from A and B (arithmetic average) varying Δ_2 from 0.060m to 0.065m – 0 to 6.4kHz

It is shown that the volume acceleration has little variation at the socket mouth, demonstrating that this parameter presents small sensitivity to the fact that all the area of the microphone is exposed to the tube channel.

5.5 – Active acoustic power

A possible use for the two-microphone actuator is its application in ESEA (Experimental Statistical Energy Analysis). A procedure based on the one-microphone actuator may lead to erroneous results as it calculates the acoustic power injected under the assumption of monopole in a free-field. The two-microphone actuator can take into account the surrounding impedance and, in principle, calculate in a more accurate fashion the pressure and particle velocity at its termination. Nevertheless, the calculation of the active intensity being injected can also lead to bad results when using the two microphones. The problem that arises is that A and B (figure 5.5.1 presents the results from the free-field experiment) have a very close magnitude, specially at low

frequencies (in the case of the used diameter it can be considered that this low frequency range is 0-2.5kHz). From equation (5.2.14) it can be seen that the active intensity ($1/2 \operatorname{Re}\{S_{pu}\}$) is expressed by the difference of the magnitudes of A and B :

$$I_a = \frac{1}{2\rho_0 c} (S_{AA} - S_{BB}) = \frac{1}{2\rho_0 c} \frac{\operatorname{Im}\{S_{12}\}}{\sin(k\Delta_1)} \quad (5.5.1)$$

The last equation shows that the calculation of the active intensity by using the two-microphone technique is highly sensitive to: the phase-mismatch between the sensors, the precision of amplitude measurement, and the distance between the microphones (when $k\Delta_1$ tends to 180° , the result is highly sensitive to small imprecision of the sensors).

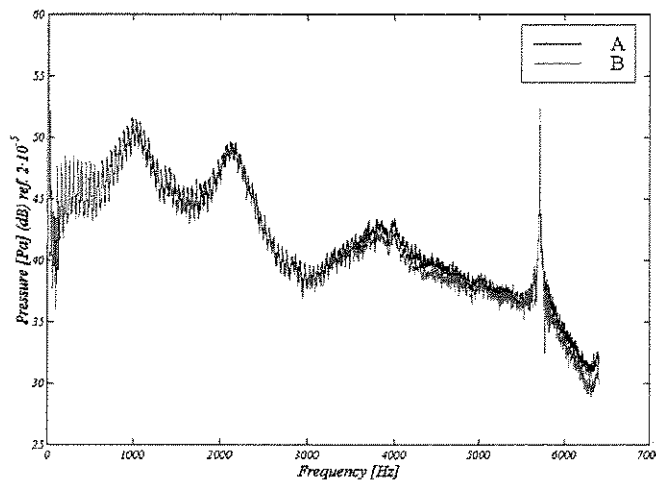


Figure 5.5.1 – Magnitudes of A and B for a free-field experiment

When the two-microphone actuator is placed in a medium that can not be considered a free-field, the magnitudes of A and B may change, but they are still close to each other (specially at low frequencies) and the calculation of the difference between S_{AA} and S_{BB} is critical. Figure 5.5.2 shows the magnitudes of A and B from the application of the two-microphone actuator to the small rectangular cavity studied in chapter 6. The curves are very close to each other, even in some regions of high frequency, and the identification of the active intensity becomes very imprecise in a very large range of frequencies.

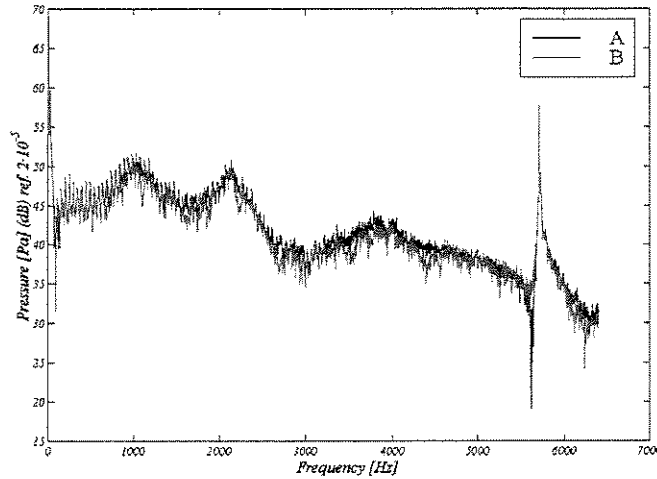


Figure 5.5.2 – Magnitudes of A and B for the rectangular cavity experiment

As seen in the precedent section, the volume velocity calculation presents good precision. So, using the radiation impedance for an unflanged tube applied to the particle velocity found at the tube mouth, the active acoustic power (active intensity times area) was calculated:

$$P_a = \frac{1}{2} \operatorname{Re} \left\{ \frac{u_{AB}}{z_{unflanged}} \cdot u_{AB}^* \right\} S \quad (5.5.2)$$

where u_{AB} is the particle velocity calculate at the tube mouth using A and B from arithmetic average, and S is the tube cross-section area. Figure 5.5.3 shows the comparison of this active acoustic power to the one measured at a distance r (using the monopole theory for the particle velocity calculation) from the actuator termination.

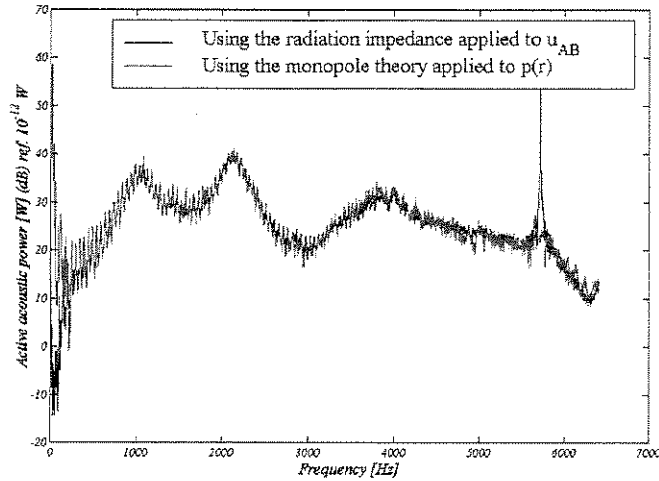


Figure 5.5.3 – Comparison of the active acoustic power calculated from the radiation impedance applied to u_{AB} and from the monopole theory applied to $p(r=0.4m)$ – 0-6.4kHz

Figure 5.5.4 shows the comparison between the active acoustic power calculated from A and B , and from the monopole theory applied to the pressure measure at a distance r .

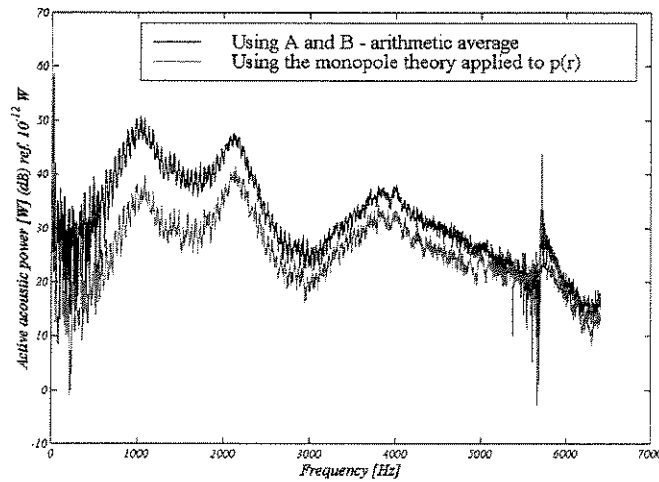


Figure 5.5.4 – Comparison of the active acoustic power calculated from A and B and from the monopole theory applied to $p(r=0.4m)$ – 0-6.4kHz

The curves seem to be shifted by a constant above $2.5kHz$. Analyzing the pressure at the socket mouth (figure 5.5.5) it can be noticed that the use of A and B over-predicts this pressure.

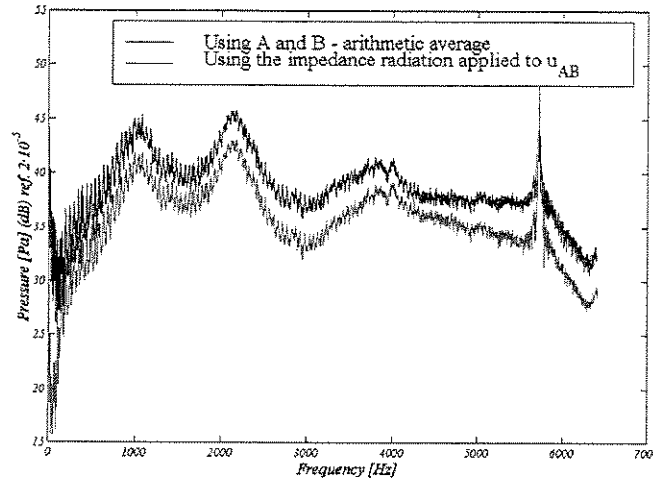


Figure 5.5.5 – Comparison of the pressure at the socket termination calculated from A and B with correction and from the radiation impedance applied to u_{AB} – 0-6.4kHz

The probable cause of this error is the microphone mounting in the socket, which has all its area exposed to the inner cylinder. Supposing the pressure measured as the pressure in the center of the microphone may lead to erroneous results. Figure 5.5.6 shows the pressure obtained considering the distance from p_1 to the socket mouth (Δ_2) equal to $0.062m$. As opposed to the particle velocity, the pressure varies a lot in the region near to the mouth due to the fact that the incident and reflected waves are almost in opposition of phase and that the socket mouth is almost a pressure node.

A procedure similar to what was done with the one-microphone actuator is done here. Taking the pressure that results from the application of the radiation impedance to u_{AB} as reference, a constant which the pressure calculated from A and B should be divided for is found. Its value is approximately 2 and figure 5.5.7 shows that this leads to a reasonable result.

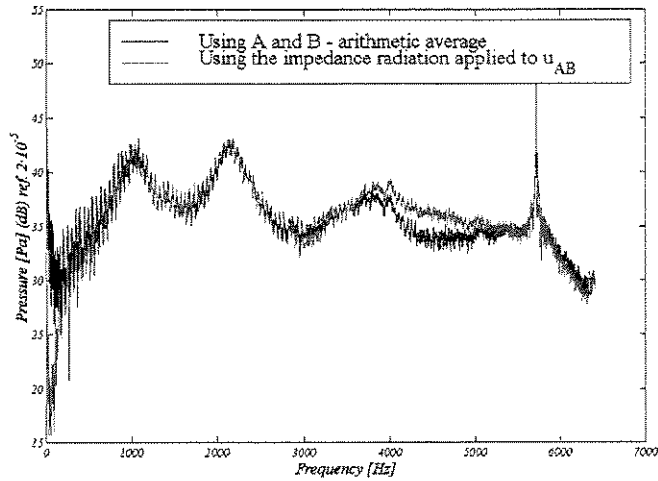


Figure 5.5.6 – Comparison of the pressure at the socket termination calculated from A and B using $\Delta_2 = 0.062m$ and from the radiation impedance applied to $u_{AB} - 0-6.4kHz$

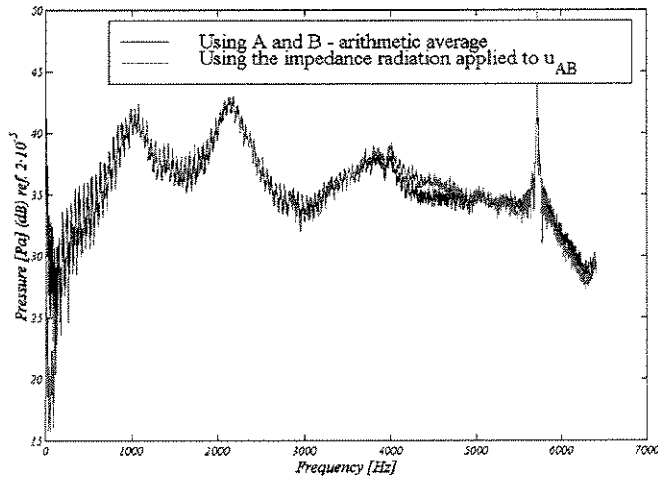


Figure 5.5.7 – Comparison of the pressure at the socket termination calculated from A and B with correction and from the radiation impedance applied to $u_{AB} - 0-6.4kHz$

Applying the correction proposed above to the pressure at the socket mouth, it can be noticed (figure 5.5.8) that the active acoustic power presents a better agreement when compared

to the measurement at a distance r . It is interesting to note that the results present better agreement after 2.5kHz , which is approximately the frequency (figure 5.5.1) that A seems to differ significantly from B .

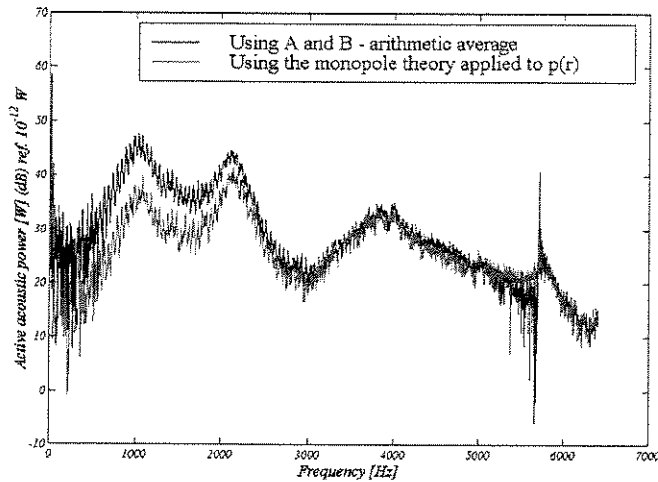


Figure 5.5.8 – Comparison of the active acoustic power calculated from A and B with correction and from the monopole theory applied to $p(r=0.4\text{m}) - 0-6.4\text{kHz}$

As a verification, the reactive acoustic power ($1/2 \text{Im}\{p \cdot u^*\}S$) was calculated. Figure 5.5.9 shows the original results and figure 5.5.10 the results with the corrected pressure. It is observed a very good agreement when the correction is applied.

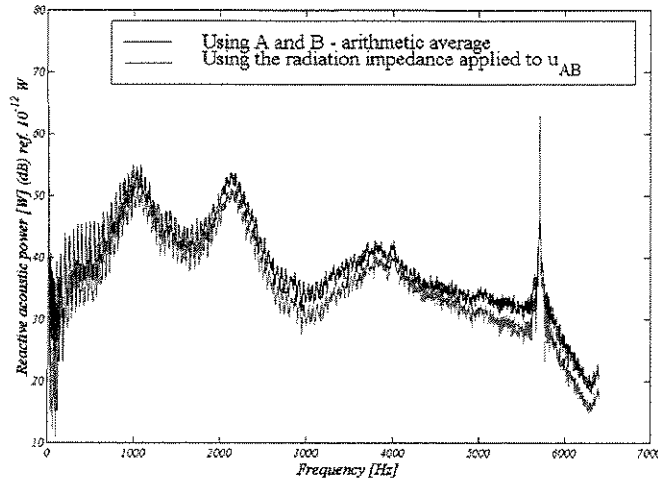


Figure 5.5.9 – Comparison of the reactive acoustic power calculated from A and B and from the radiation impedance applied to u_{AB} – 0-6.4kHz

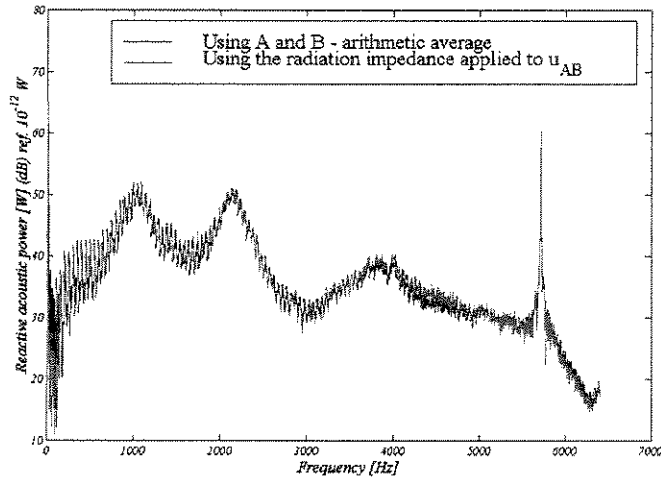


Figure 5.5.10 – Comparison of the reactive acoustic power calculated from A and B with correction and from the radiation impedance applied to u_{AB} – 0-6.4kHz

The technique of Chung, 1978, based on the geometric average of S_{12} measured in the original and with the microphones switched was tested. Figure 5.5.11 shows its comparison with use of the arithmetic average of A and B and the results present good agreement.

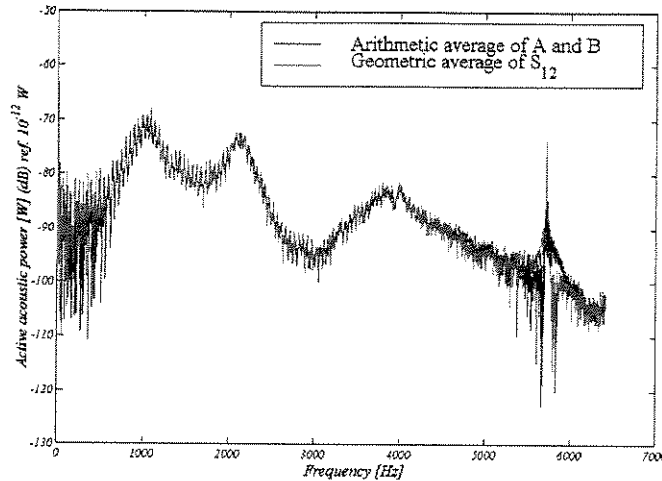


Figure 5.5.11 – Comparison of the active acoustic power calculated from A and B and from the geometric average of S_{12} – 0-6.4kHz

The general conclusion that can be made is that the two-microphone actuator constructed is able to measure correctly the volume acceleration it is injecting into the medium in a very large frequency range, but presents problems when measuring the acoustic power being injected. This is due basically to the strong impedance mismatch between the tube and the surrounding impedance, which leads to a very reflexive boundary at the socket mouth at low frequencies. In this frequency range A and B become very close to each other and the calculation of the active intensity is very sensitive to small amplitude and phase errors. For the actuator constructed (inner diameter of 1cm and microphone separation of 3cm) the range of frequency it is capable to measure active intensity is 2.5-5kHz (if the correction proposed is applied). If the active intensity is required for lower frequencies another actuator with higher inner diameter and microphone separation is needed.

Chapter 6

Results and discussions

6.1 – Introduction

This chapter presents the results of the acoustic modal analysis performed in a rectangular shallow cavity of small dimensions. As one of the dimensions was taken much smaller than the other two, the problem becomes two-dimensional in a wide frequency range. The walls were rigid, resulting in a strongly reverberant acoustic field.

Three acoustic actuators were used in this modal analysis:

- *Shaker-driven piston actuator*

The shaker-driven piston actuator (figure 6.1.1) was composed of a small shaker, a 21.5mm diameter PVC piston, a thin rubber membrane stretched flush to one of the cavity side walls covering a cylindrical hole, and a piezoelectric accelerometer. The air volume acceleration is given by the accelerometer signal times the piston area.

This device was used in the first experiments and its results served as a reference to the following development of the actuators based on the driver loudspeaker. Nevertheless, its use imposes some practical difficulties as the positioning – the piston has to be parallel to the stretched membrane – and the limited acoustic power it delivers.

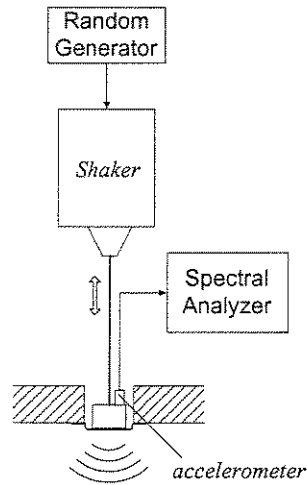


Figure 6.1.1 – Shaker-driven piston actuator assembly

□ *One-microphone actuator*

The developments of chapter 4 are analyzed with the application of this device (figure 6.1.2) into a cavity presenting high acoustic impedance. In this case, the basic assumption made in the development of the one-microphone actuator, that its impedance is much higher than the surrounding it acts in, becomes fragile and will be investigated.

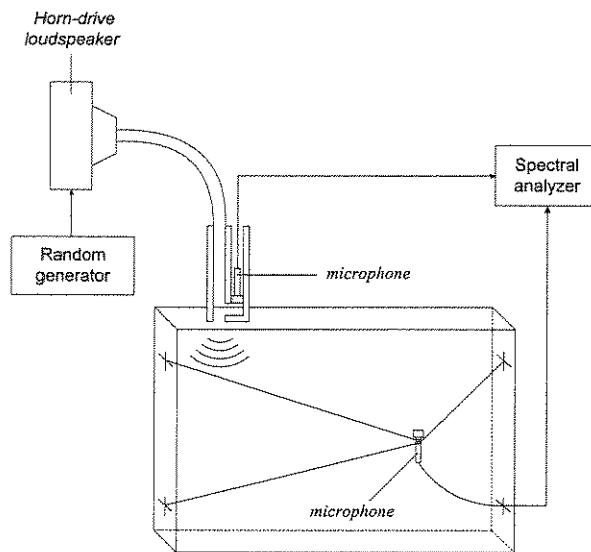


Figure 6.1.2 – One-microphone actuator

□ *Two-microphone actuator*

The use of two microphones showed (chapter 5) that the volume acceleration can be calculated correctly without assuming a condition for the surrounding where the actuator is placed. The experiment with the small rectangular cavity will verify if the two-microphone actuator can deal with a high impedance medium in terms of volume acceleration.

The box containing the cavity (figure 6.1.3) was built in wood, except for its upper wall, made of plexi-glass to facilitate the microphone positioning. One concern of this construction was the stiffness of the walls. A small cavity (254×199×30mm) with relative thick walls avoided the vibroacoustic coupling in the range of frequencies analyzed, leading to the study of the uncoupled acoustic modes only. The experimental scheme of the cavity instrumentation is presented in figure 6.1.2, where a 1/4" electret microphone has its positioning made by thin nylon strings.

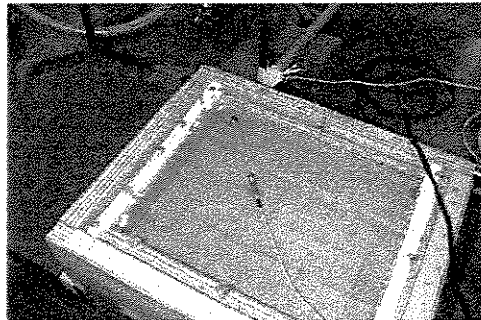


Figure 6.1.3 – Constructed cavity

The measurement points coincide with the nodes of the FEM mesh constructed (figure 6.1.4), with 10 elements in each direction, resulting in 121 measurement points.

Following, the results of the application of the three acoustic actuators are presented. The Frequency Response Functions are compared to the analytical solution, which takes into account a damping value of 0.01 ($\eta = 0.02$). This value was taken from table 6.5.2 and represents approximately the average of the modal damping of the first seven modes for the shaker-driven piston and two-microphone actuator experiments. The excitation point corresponds to the point

112 of figure 6.1.4 and for the analysis two points were chosen: one near to the excitation location (point 80 in figure 6.1.4) and another far from the excitation location (point 53 in figure 6.1.4). The other 119 points present the same behavior when compared to the analytical solution as these two points that will be analyzed.

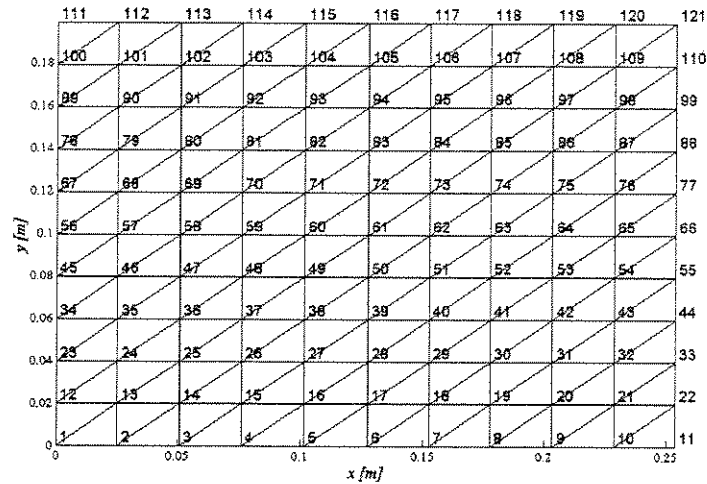


Figure 6.1.4 – Rectangular cavity FEM mesh

6.2 – Shaker-driven piston actuator experiment

As mentioned above, the experiment with the shaker-driven piston (figure 6.2.1) served as a reference. This actuator has the advantage that it has a good response at low frequencies.

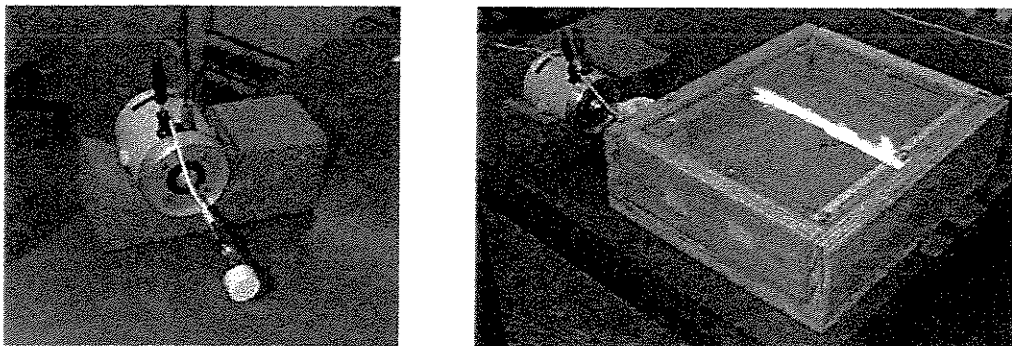


Figure 6.2.1 – Shaker-driven piston (left) and the experimental setup (right)

Figure 6.2.2 shows the comparison between the analytical and experimental FRFs for the points 53 and 80 in the frequency range of 0-3.2kHz. It can be observed an excellent agreement between the curves over all the frequency range. For point 80, near to the excitation, the first antiresonance presents some perturbation and it is probably due to the difficult positioning of the piston parallel to the elastic membrane.

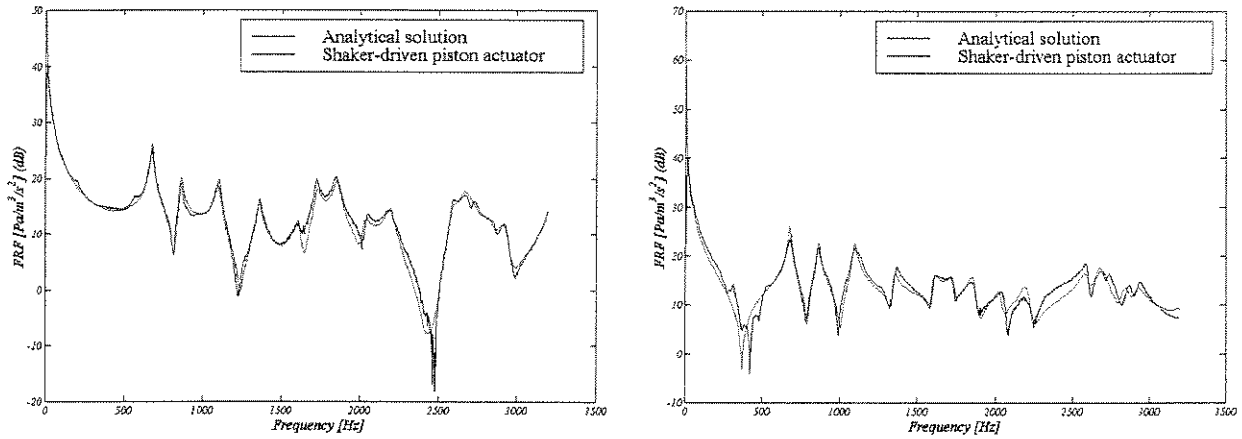


Figure 6.2.2 – Comparison between the analytical and experimental FRFs at the points 53 (left) and 80 (right)

The coherence between the microphone inside the cavity and the accelerometer attached to the piston (figure 6.2.3) is quite good outside the antiresonance regions, which is expected.

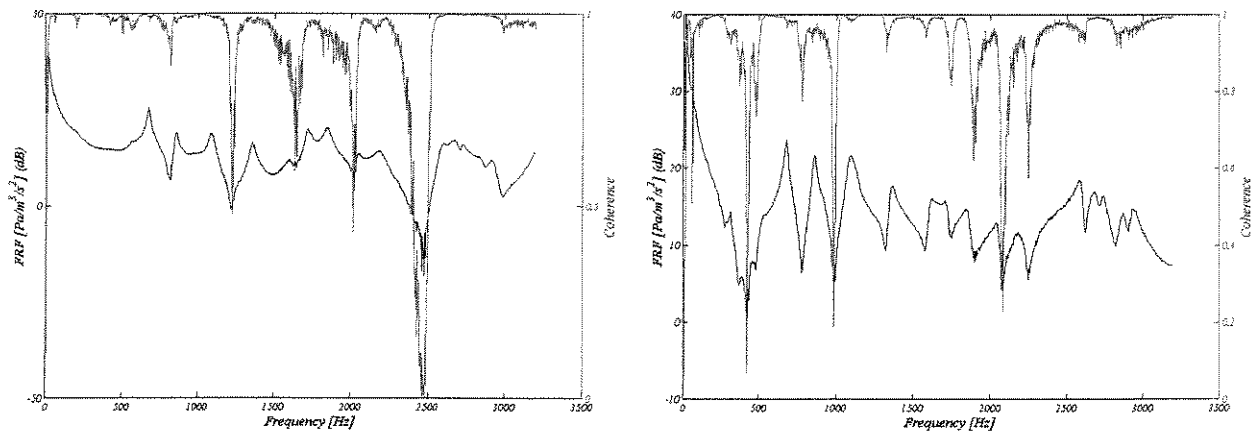


Figure 6.2.3 – Coherence (between the microphone inside the cavity and the accelerometer mounted on the piston) and FRFs at the points 53 (left) and 80 (right)

6.3 – One-microphone actuator experiment

The experimental setup for this experiment is presented in figure 6.3.1. The experimental FRFs will be constructed using both the transfer function \hat{H} and radiation impedance for a flanged tube (the actuator was placed flush to the surface of the side wall of the cavity).

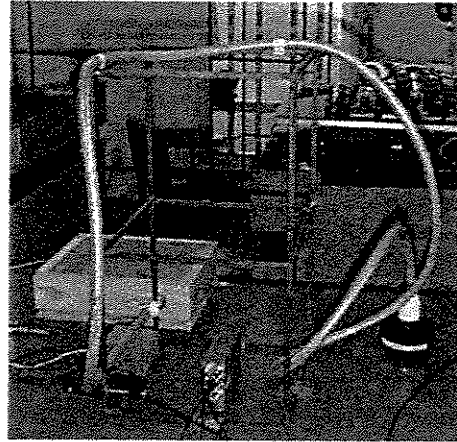


Figure 6.3.1 – Experimental setup for the application of the one-microphone actuator

Figures 6.3.2 (point 53) and 6.3.3 (point 80) show the comparison between the experimental FRFs constructed using \hat{H} and the radiation impedance. The use of the correction proposed in chapter 4 (division of the pressure of the socket by a constant, which was approximately 2 for the constructed actuator) demonstrates its validity and can be considered as a good option as it eliminates the need for the transfer function.

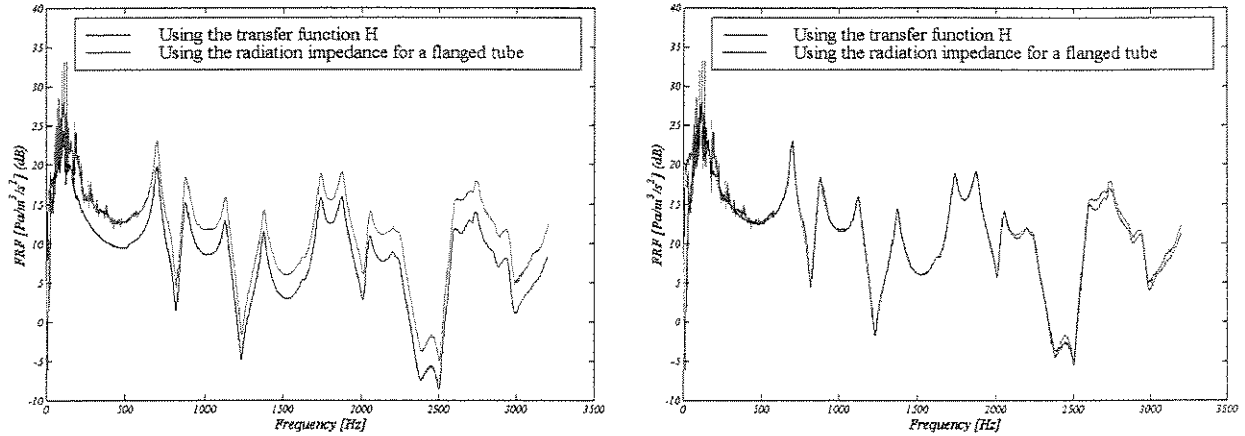


Figure 6.3.2 – Comparison between the FRFs constructed using H and the radiation impedance without correction (left) and with correction (right) at the point 53

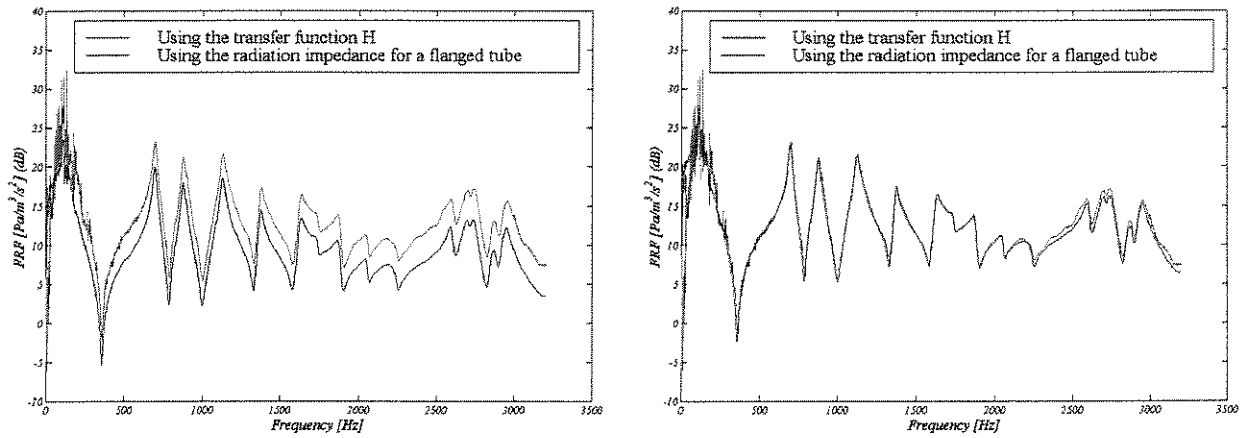


Figure 6.3.3 – Comparison between the FRFs constructed using H and the radiation impedance without correction (left) and with correction (right) at the point 80

The comparison of the experimental data with the analytical solution (figure 6.3.4) indicates that the basic assumption of this type of actuator can be misleading in a case where acoustic impedance of the medium is not negligible in relation to the actuator impedance.

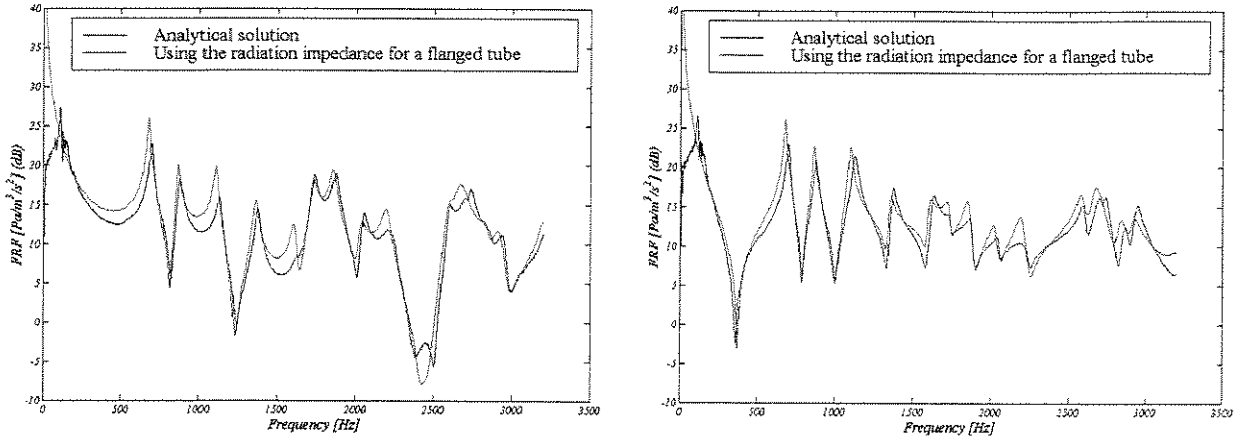


Figure 6.3.4 – Comparison between the analytical and experimental (using the radiation impedance with correction) FRFs at the points 53 (left) and 80 (right)

The coherence between the microphones, in the cavity and inside the actuator, is excellent. The inefficiency below approximately 300Hz is expected and is due to the driver limitation and to the poor efficiency of the radiation from the tube at low frequencies.

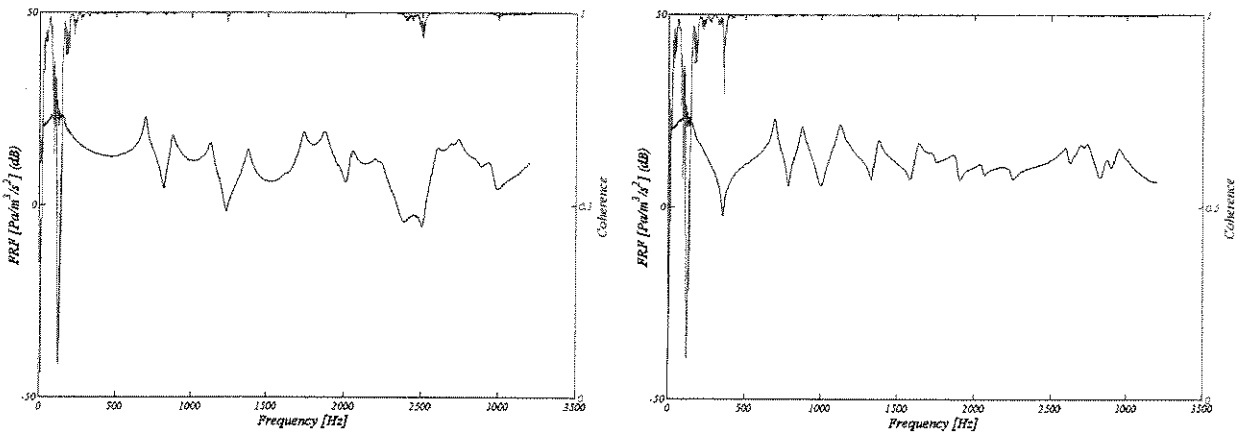


Figure 6.3.5 – Coherence between the microphones, and FRFs at the points 53 (left) and 80 (right)

6.4 – Two-microphone actuator experiment

The use of the two-microphone actuator (figure 6.4.1) is an attempt to measure correctly the volume acceleration being injected into the medium and the case of the rectangular cavity used can be considered an extreme case for the performance evaluation of this actuator.

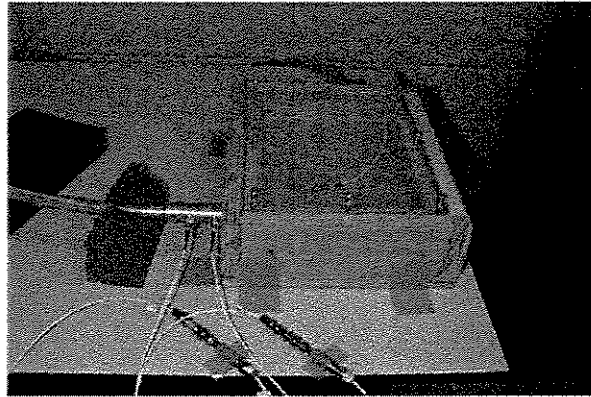


Figure 6.4.1 – Experimental setup for the application of the two-microphone actuator

Comparison between the experimental and analytical results (figure 6.4.2) shows good agreement and proves the efficiency of this new actuator in taking into account the surrounding impedance.

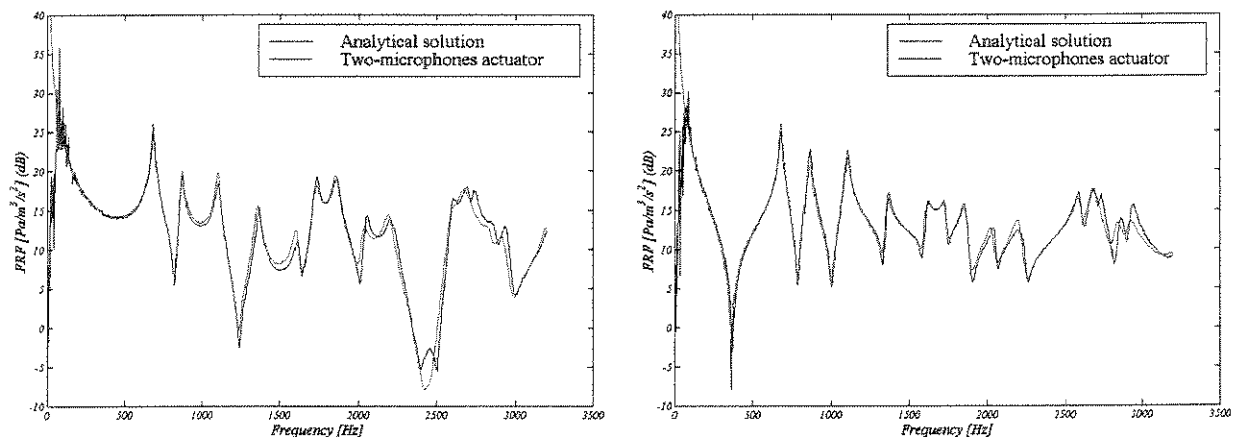


Figure 6.4.2 – Comparison between the analytical and experimental FRFs at the points 53 (left) and 80 (right)

In figure 6.4.2 (left) it can be noticed that in the antiresonance near $2.5kHz$ the experimental FRF presents a strange behavior. It appears also in the one-microphone experiment results and its origins are still to be investigated. Anyway, it happens in a region where the FRF reaches a very low value and does not weigh much in the modal parameter extraction process.

Another detail is that an "extra" resonance appears at approximately $2.7kHz$. It appears also in the FRFs using the shaker-driven piston and the one-microphone actuators, and the reason why it is no appearing in the analytical FRF may be due to a node exactly at this location or to some small imperfection in the constructed cavity that is not foreseen in the analytical model.

Figure 6.4.3 shows the coherence between the microphone in the cavity and the one (p_1) inside the socket closest to the tip. There is an excellent coherence with exception of a region near $3kHz$, where the radiation efficiency of the ensemble tube and socket is poor. Nevertheless, the small coherence in this region does not seem to strongly influence the FRFs.

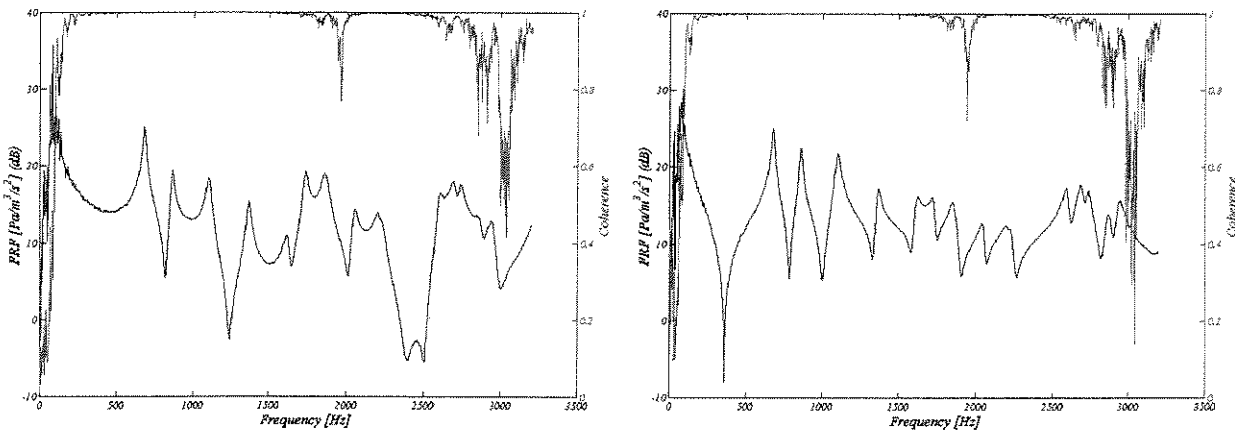


Figure 6.4.3 – Coherence between the microphones, and FRFs at the points 53 (left) and 80 (right)

6.5 – General analysis

A two-dimensional FEM model using linear triangular elements (chapter 3) was implemented in *MATLAB*[®] language in order to analyze the behavior of the numerical solution. The model consisted of 10 elements in each direction (figure 6.1.4) and the excitation was put in node 112. Following the criteria of a minimum number of 10 elements per wavelength, the maximum frequencies allowed for the analysis from the numerical model are 1350Hz (in the longer dimension - x) and 1724Hz (in the shorter dimension - y). Figure 6.5.1 shows a comparison between the numerical and analytical FRFs and there is excellent agreement until approximately 1500Hz, which obeys the criteria exposed above.

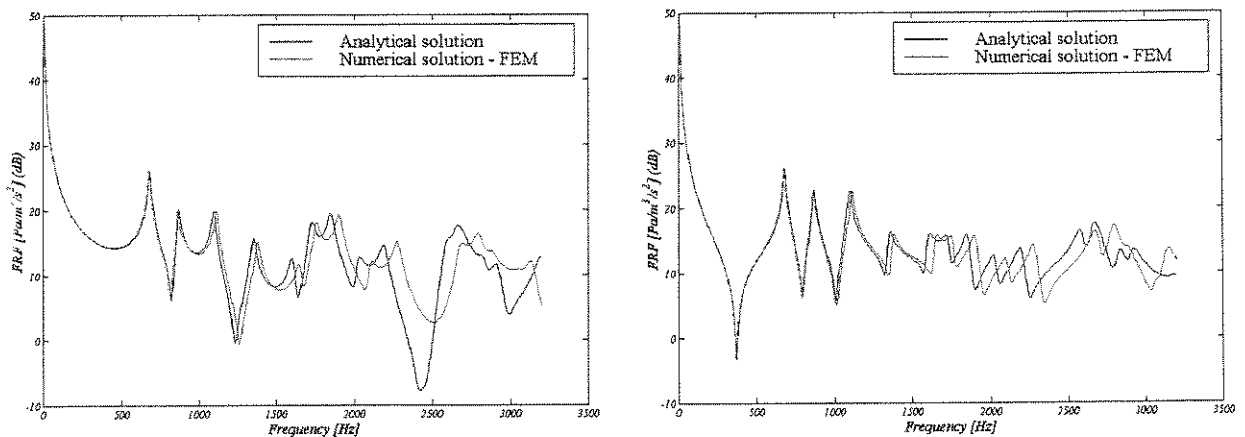


Figure 6.5.1 – Comparison between the analytical and numerical(FEM) FRFs at the points 53 (left) and 80 (right)

Table 6.5.1 compares the natural frequencies of the undamped analytical and numerical models and presents the error committed in the numerical result. As expected, the error tends to grow with frequency due to the chosen discretization.

Table 6.5.1 – Errors in the numerical natural frequencies with respect to the analytical value

<i>mode</i>	f_n (Hz) <i>Analytical</i>	f_n (Hz) <i>FEM</i>	<i>error (%)</i>
1	675.2	677.9	0.40
2	861.8	865.3	0.41
3	1094.8	1108.0	1.21
4	1350.4	1372.4	1.63
5	1602.0	1645.9	2.74
6	1723.6	1751.5	1.62
7	1851.1	1898.9	2.58

Figures 6.5.2 and 6.5.3 show the comparison between FRFs obtained using the two-microphone actuator and the other two actuators. The use of the one-microphone actuator in this cavity is problematic and the FRFs are distorted. The results from the shaker-driven piston actuator is in accordance with the two-microphone actuator results, but this last one fitted better the analytical solution.

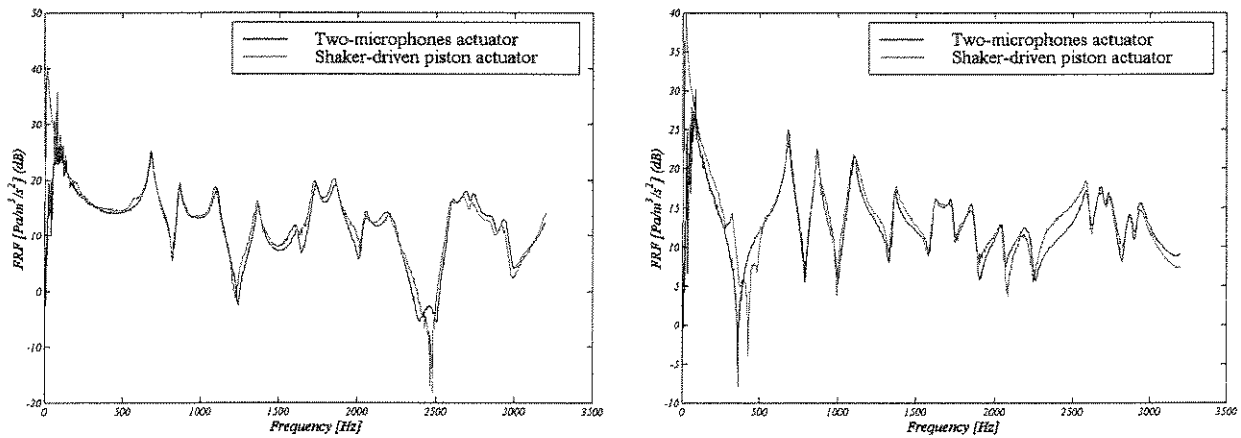


Figure 6.5.2 – Comparison between the experimental FRFs using the shaker-driven piston actuator and the two-microphone actuator at the points 53 (left) and 80 (right)

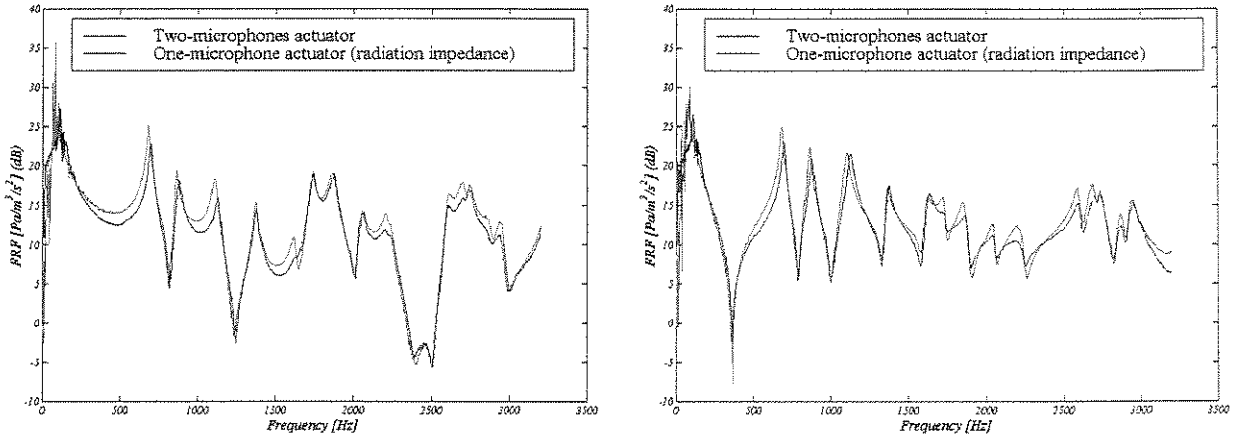


Figure 6.5.3 – Comparison between the experimental FRFs using the one-microphone actuator (using the radiation impedance) and the two-microphone actuator at the points 53 (left) and 80 (right)

For the modal parameter extraction, the Exponential Complex Method (Ewins, 1984) was used and table 6.5.2 shows the comparison between the results obtained with the three actuators. The damping extracted from the experiments with the shaker-driven actuator and with the two-microphone actuator agrees very well, and the use of the one-microphone actuator seems to overestimate the damping.

Table 6.5.2 – Modal parameters from the application of the three actuators

mode	ζ	f_n (Hz)	ζ	f_n (Hz)	ζ	f_n (Hz)
	Shaker-driven piston					
1	0.0138	676.8	0.0172	695.2	0.0099	678.0
2	0.0111	857.1	0.0161	875.0	0.0105	860.4
3	0.0169	1094.3	0.0172	1128.1	0.0121	1099.0
4	0.0100	1359.4	0.0130	1368.9	0.0086	1361.9
5	0.0101	1608.7	0.0109	1623.5	0.0108	1613.4
6	0.0081	1719.0	0.0088	1731.3	0.0072	1726.7
7	0.0110	1858.2	0.0095	1875.9	0.0104	1858.7

Table 6.5.3 presents the errors in the extracted natural frequencies with respect to the analytical ones. For the shaker-driven piston and the two-microphone actuators, the errors are smaller than 1%. For the one-microphone actuator, the errors are greater as expected.

Table 6.5.3 – Errors in the experimental natural frequencies with respect to the analytical value

<i>mode</i>	<i>Shaker-driven piston</i> (%)	<i>One-microphone actuator</i> (%)	<i>Two-microphone actuator</i> (%)
1	0.24	2.96	0.41
2	0.55	1.53	0.16
3	0.05	3.04	0.38
4	0.67	1.37	0.85
5	0.42	1.34	0.71
6	0.27	0.45	0.18
7	0.38	1.34	0.41

6.6 – Pressure and particle velocity fields visualization

In this section the idea presented in chapter 2 and developed in appendix D is applied to the experimental pressure field of the third mode (1100Hz). Figure 6.6.1 (left) presents this field and figure 6.6.1 (right) presents a "mirrored" field, which avoided the leakage in both directions when applying the DFT.

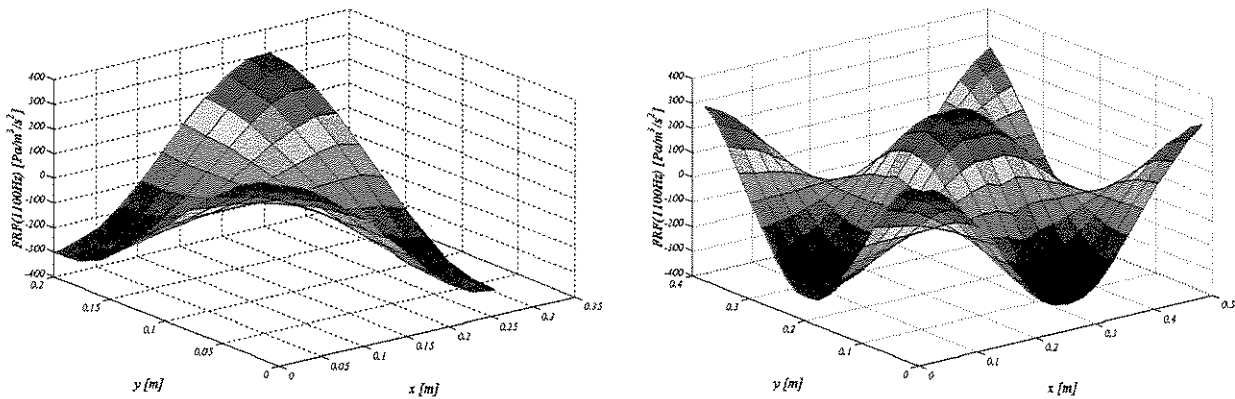


Figure 6.6.1 – Original (left) and mirrored (right) experimental pressure field for the 3rd mode (1100Hz)

The analytical solution for the particle velocity field (6.6.2) is presented in appendix D and serves as a reference for the particle velocity field calculated from the application of the DFT to the experimental pressure field.

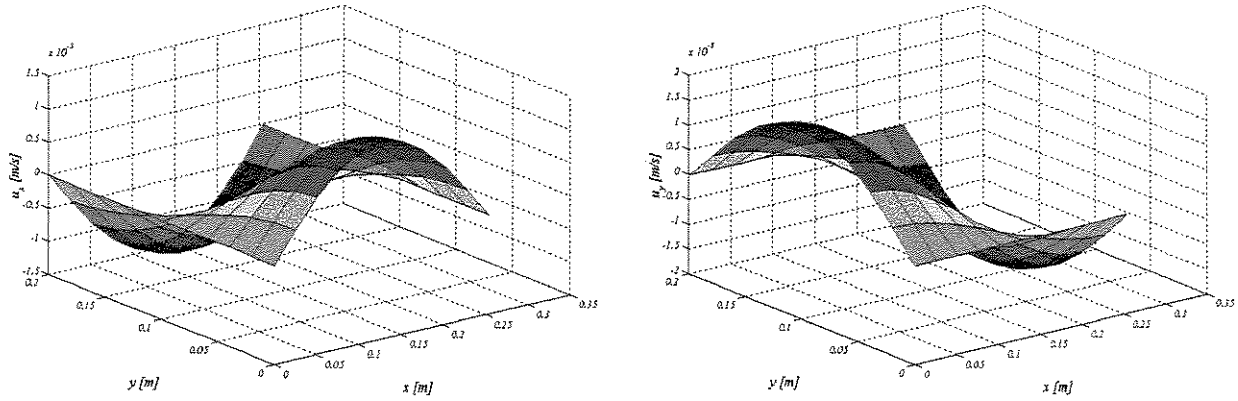


Figure 6.6.2 – Analytical particle velocity field in x-(left) and y-(right) directions for the 3rd mode (1100Hz)

The particle velocity field that resulted from the experimental data (figure 6.6.3) agrees well with the analytical field, but presents excessive distortions due to the influence of high wave number noise. When calculating the derivatives, each line in the wave number space must be multiplied by ik , so small distortions in high wave numbers are amplified in this procedure.

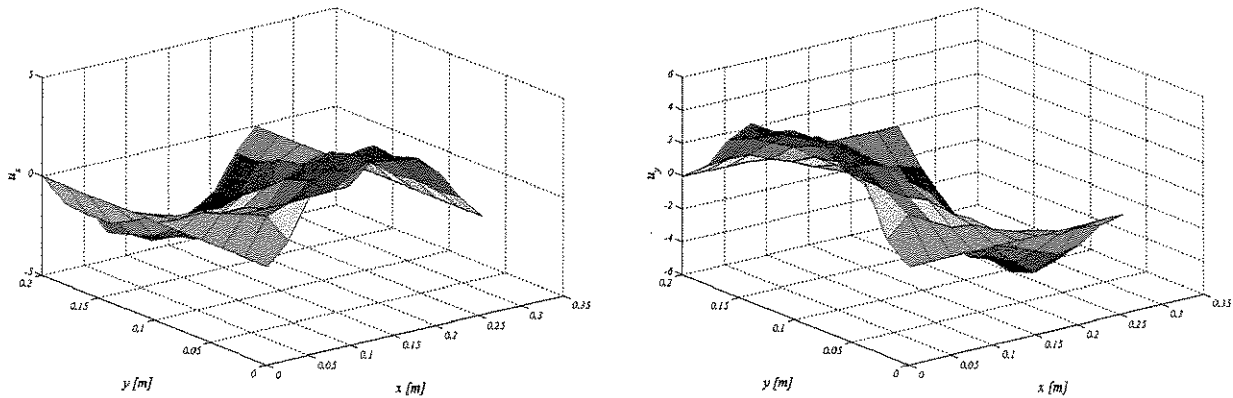


Figure 6.6.3 – Particle velocity field from DFT in x-(left) and y-(right) directions for the 3rd mode (1100Hz)

To avoid the presence of high wave number distortions, a simple filtering technique was used. The amplitudes of the higher wave number terms, which is very small in this case (figure 6.6.4 (left)), were taken to zero (figure 6.6.4 (right)).

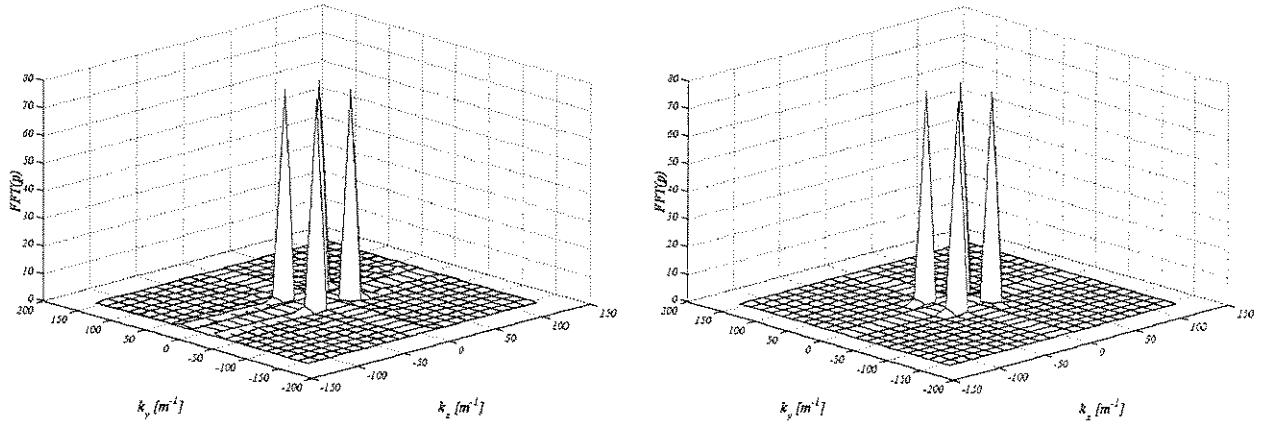


Figure 6.6.4 – Original (left) and filtered (right) FFT of the pressure field for the 3rd mode (1100Hz)

The particle velocity field that results from the filtered data is given in figure 6.6.5, and the agreement with the analytical field is excellent.

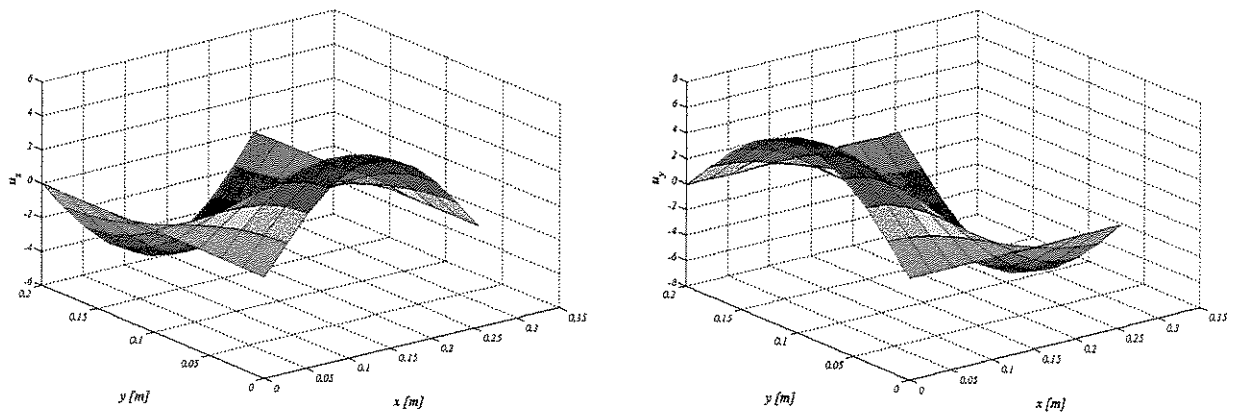


Figure 6.6.5 – Particle velocity field from filtered data in x-(left) and y-(right) directions for the 3rd mode (1100Hz)

Figure 6.6.6 shows the wire-frame representation of the particle displacement field, which is an alternative way of visualizing the acoustic field.

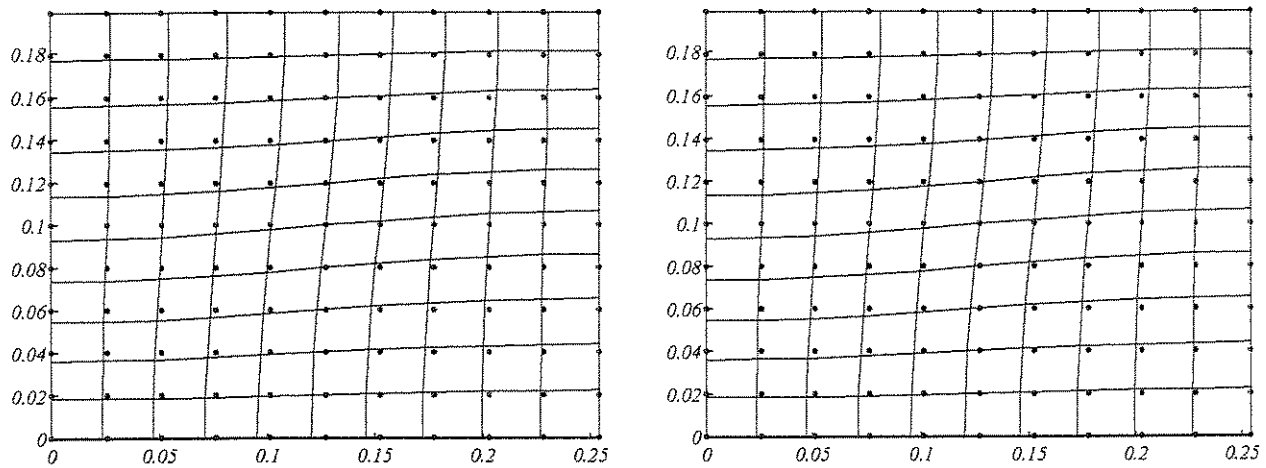


Figure 6.6.6 – Wire-frame representation of the particle displacement field for the 3rd mode (1100Hz); analytical (left) and experimental with filtered data (right) fields

The agreement between the experimental (with filtered data) and analytical results in figure 6.6.6 is excellent. An important remark is that the simple filtering technique used was possible because the pressure field was mirrored in a way that leakage was avoided. When boundary conditions are not as simple as the one present in the studied case, a surface smoothing technique, like the RDFS proposed by Arruda (1992) is necessary in order to control the leakage effects.

Capítulo 7

Conclusões e perspectivas

A análise modal acústica de uma cavidade retangular foi realizada. Para isto, quatro questões básicas foram tratadas: *i*) a definição de variáveis de entrada e saída em sistemas acústicos, *ii*) as correções de unidade nos modelos analítico e numérico necessárias para a comparação com as FRFs experimentais, *iii*) a visualização de um campo acústico, e *iv*) o desenvolvimento de atuadores acústicos calibrados.

Depois de responder às questões *i* (capítulo 2), *ii* (capítulo 3) e *iii* (capítulo 2 e apêndice D), o problema do dispositivo calibrado de excitação foi tratado nos capítulos 4 e 5. Um atuador que já está comercialmente disponível (atuador com um microfone) foi construído, mas apresentou sérias limitações quando aplicado num meio onde a impedância acústica é alta (cavidade pequena). Uma alternativa baseada no uso de dois microfones foi proposta e sua aplicação na análise modal apresentou bons resultados (capítulo 6). Entretanto, sua aplicação na Análise Estatística de Energia Experimental (ESEA), que requer a intensidade ativa injetada no meio, é ainda um problema em aberto. Os maus resultados no cálculo da intensidade ativa se deveram a problemas intrínsecos associados ao uso dos dois microfones (capítulo 5). Por outro lado, quando o meio se aproxima de um campo livre, o uso da impedância de radiação em tubos apresenta bons resultados. Sua aplicação nos atuadores com um e dois microfones numa sala anecóica demonstrou excelente concordância com relação à aceleração de volume e potência acústica ativa em comparação com medidas feitas a uma distância r do bocal do atuador.

Para futuros trabalhos, uma modificação na montagem do microfone é sugerida. Como discutido no capítulo 5, a exposição de toda área do microfone ao interior do tubo não é um fator

limitante para o cálculo de aceleração de volume, mas pode influenciar as medidas de intensidade ativa usando a técnica dos dois microfones. A figura 7.1 (esquerda) mostra como os microfones foram montados no atuador com dois microfones e a figura 7.1 (direita) apresenta a montagem proposta, que permite uma medida mais precisa da distância entre os dois microfones e entre os microfones e a terminação do tubo. O atuador com um microfone teve a montagem como a exposta na figura 7.1 (direita) e a coerência não parece ser afetada por esta opção geométrica.

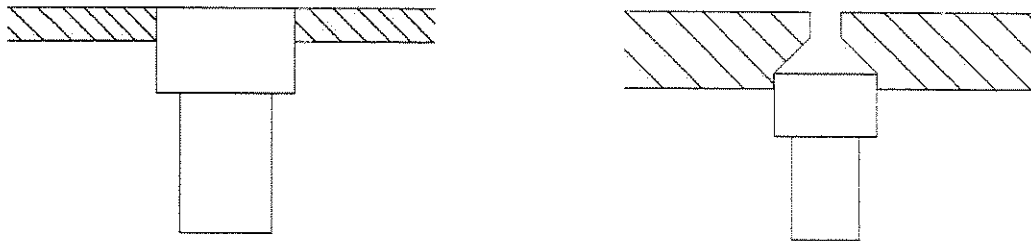


Figura 7.1 – Montagem do microfone na parede do tubo

Uma opção interessante para a medida de intensidade ativa é o uso de sensores de velocidade de partícula como o Microflown (Bree et al., 2000). Em publicações da empresa Microflown (podem ser obtidas no sítio www.microflown.com), uma sonda p-u que associa um microfone a um sensor de velocidade de partícula é testada e calibrada num tubo de ondas estacionárias e os resultados são bastantes encorajadores. Entretanto, este sensor de velocidade de partícula apresenta uma faixa de frequência limitada e, neste momento, parece que medidas confiáveis seriam limitadas à faixa de 500-3000Hz. A figura 7.2 mostra esquematicamente um atuador acústico aperfeiçoado que incorpora o sensor de velocidade de partícula e que, em princípio, permite a medida da aceleração de volume na terminação do tubo e da intensidade ativa sendo injetada no meio.

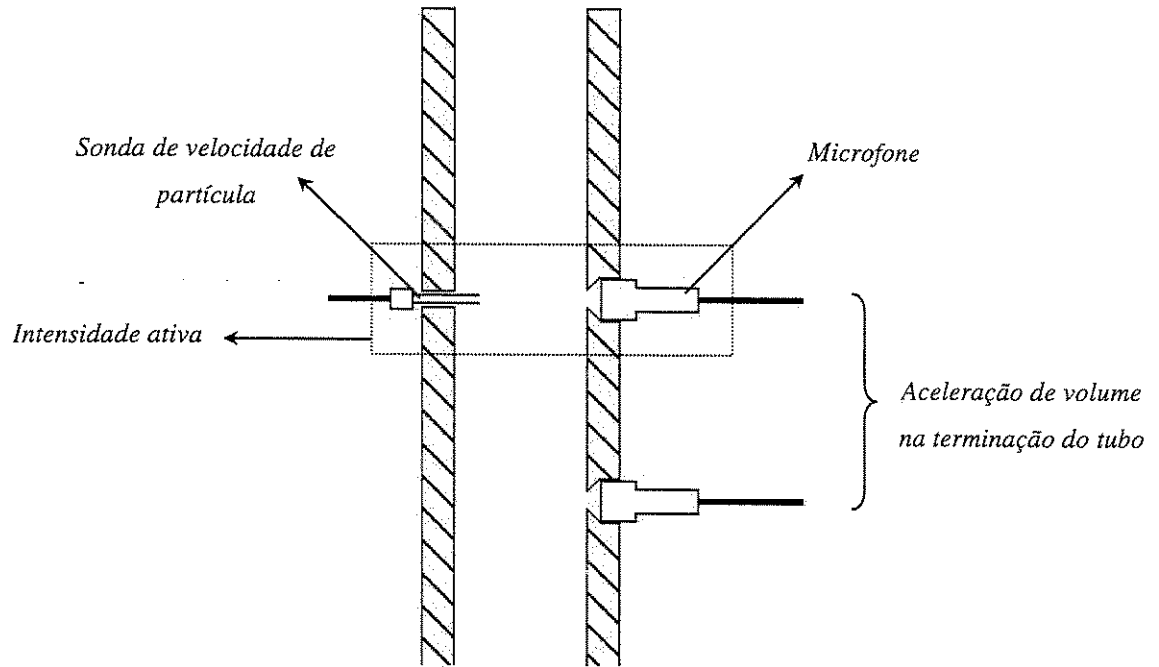


Figura 7.2 – Atuador acústico aperfeiçoado

Conclusions and perspectives

The experimental acoustic modal analysis of a rectangular shallow cavity was performed. For this, four basic issues were addressed: *i*) the definition of input and output variables in an acoustic system, *ii*) the unit corrections in the analytical and numerical models needed for the comparison with the experimental FRF, *iii*) the visualization of an acoustic field, and *iv*) the development of a calibrated acoustic actuator.

After answering the questions *i* (Capítulo 2), *ii* (Capítulo 3) and *iii* (Capítulo 2 and Apéndice D), the problem of the calibrated excitation device was tackled in Capítulos 4 and 5. An actuator which is already commercially available (the one-microphone actuator) was built, but it presented serious limitations when applied to a medium where the acoustic impedance is high (small shallow cavity). An alternative based on the use of two microphones was proposed and its application in the modal analysis was very successful (Capítulo 6). Nevertheless, its application in ESEA (Experimental Statistical Energy Analysis), which requires the active intensity being injected into the medium, is still an opened problem. The bad results in calculating the active intensity were due to the intrinsic problems associated with the use of the two microphones (Capítulo 5). When the medium approximates a free-field, the use of the radiation impedance for tubes can yield good results. Its application in the one-microphone and in the two-microphone actuators in an anechoic room demonstrated excellent agreement in volume acceleration and active acoustic power when compared to the measurement at a certain distance r .

For future works, one modification in the microphone mounting can be suggested. As discussed in Capítulo 5, the exposition of all the microphone area to the interior of the tube is not a limiting factor to the calculation of the volume acceleration, but it can influence the measurement of active intensity using the two-microphone technique. Figure 1 (left) shows how the microphones were mounted in the two-microphone actuator and figure 1 (right) presents the proposed mounting, which leads to a more reliable distance measured between the microphones and between the microphones to the tube termination. The one-microphone actuator had a microphone mounting as exposed in figure 7.1 (right) and the coherence does not seem to be affected by this geometrical choice.

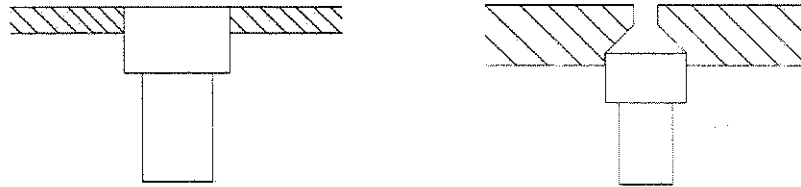


Figure 7.1 – Microphone mounting in the tube wall

An interesting option for the measurement of active intensity is the use of particle velocity sensors as the Microflow (Bree et al., 2000). In (Bree et al., downloaded paper) and (Van der Eerden et al., downloaded paper) a p-u probe associating a microphone to the particle velocity sensor is tested and calibrated in a standing wave tube and the results are very encouraging. However, this particle velocity sensor presents a limited frequency range and, for the moment, it seems that a reliable measurement would be limited to the 500-3000Hz range. Figure 7.2 shows schematically an improved acoustic actuator that incorporates the velocity particle sensor and would, in principle, allow the measurement of volume acceleration at the tube termination and the active intensity being injected.

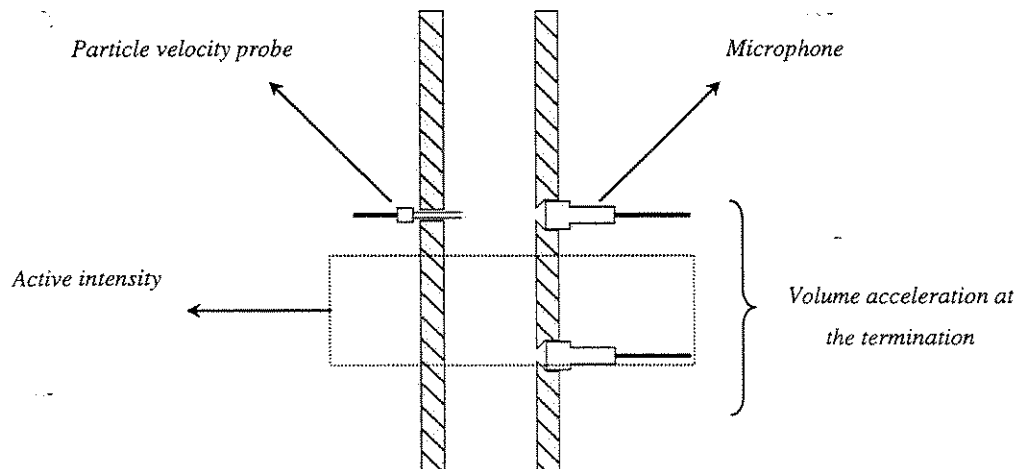


Figure 7.2 – Improved acoustic actuator

References

- Augusztinovicz, F., "*Acoustic Modal Analysis*", Proceedings of the 11th International Seminar on Applied Acoustics (ISAAC11), Seminar on Advanced Techniques in Applied and Numerical Acoustics, Leuven-Belgium, 2000.
- Augusztinovicz, F., Sas, P., "*Acoustic modal analysis at low frequencies: similarities and differences in formulation*", Proc. 21st Int. Seminar on Modal Analysis (Ed.: P. Sas), Vol. III, pp. 1650-1699, 1996.
- Arruda, J.R.F., "*Surface smoothing and partial spatial derivatives computation using a Regressive Discrete Fourier Series*", Mechanical Systems and Signal Processing, vol. 6(1), pp. 41-50, 1992.
- Arruda, J. R. F., Huallpa, B. N., "*Theoretical and Experimental Acoustic Modal Analysis of Reactive Filters in Piping System*", Proceedings of the 15th Brazilian Congress of Mechanical Engineering, Brazil, CD-ROM paper no. 487, 1999.
- Bree, H-E de, et al., "*A novel technique for measuring the reflection coefficient of sound absorbing materials*", ISMA25, International Conference on Noise and Vibration, September 13-15, Leuven, Belgium, 2000.
- Bree, H-E. de, Druyvesteyn, W.F., Elwenspoek, M., "*Realisation and calibration of a novel half inch p-u sound intensity probe*", paper downloaded from www.microflown.com.

- Brigham, E.O., *"The Fast Fourier Transform"*, Prentice-Hall, Inc., 1974.
- Byrne, K., *"The use of acoustic pressure measurement to determine the particle motions associated with the low order acoustic modes in enclosures"*, J. Acoust. Soc. Am., vol. 77(2), pp. 739-746, 1985.
- Chung, J.Y., *"Cross-spectral method of measuring acoustic intensity without error caused by instrument phase mismatch"*, J. Acoust. Soc. Am., vol. 64, pp. 1613-1616, 1978.
- Dowling, A. P., *"Steady-state radiation from sources"*, Encyclopedia of Acoustics (Ed.: Crocker, J. M.), pp. 107-125, John Wiley & Sons, Inc., 1997.
- Ewins, D. J., *"Modal Testing and Practice"*, RSP/John Wiley & Sons, 1984.
- Fahy, F. J., *"Sound Intensity"*, second edition, E & FN SPON, 1995.
- Jacobsen, F., *"A note on the accuracy of phase compensated intensity measurements"*, Journal of Sound and Vibration, vol. 128(2), pp. 247-257, 1989.
- Kinsler, L. E., Frey, A. R., Coppens, A. B., Sanders, J. V., *"Fundamentals of Acoustics"*, third edition, John Wiley & Sons, 1982.
- Kung, C-H., Singh, R., *"Experimental modal analysis for three-dimensional acoustic cavities"*, J. Acoust. Soc. Am., vol. 77(2), pp. 731-738, 1985.
- Kwon, Y. W., Bang, H., *"The finite element method using MATLAB"*, CRC Press, 1997.
- Levine, H., Schwinger, J., *"On the radiation of sound from an unflanged circular pipe"*, Phys. Rev., vol. 73(4), pp. 383-406, 1948.

- Mitchell, L.D., Kochersberger, K., Wicks, A.L., "*Structural angular velocity extraction using DFT/IDFT techniques*", Proceedings of IMAC-IX, vol. I, pp. 657-663, Florence - Italy, April 14-18, 1991.
- Morse, P.M., Ingard, K.U., "*Theoretical Acoustics*", Princeton University Press, 1986.
- Nieter, J.J, Singh, R., "*Acoustic modal analysis experiment*", J. Acoust. Soc. Am., vol. 72(2), pp. 319-326, 1982.
- Sas, P., "*Acoustic intensity measurements*", Proceedings of the 11th International Seminar on Applied Acoustics (ISAAC11), Seminar on Advanced Techniques in Applied and Numerical Acoustics, Leuven-Belgium, 2000.
- Sun, F.P., Mitchell, L.D., "*Two-dimensional velocity data smoothing and structural angular velocity extraction using a DFT/IDFT technique*", Proceedings of the Thirteenth Biennial ASME Conference, Mechanical Vibration and Noise, September 22-25, 1991.
- Van der Eerden, F.J.M., Bree, H-E. de, Tjeldeman, H., "*Experiments with a new acoustic particle velocity sensor in an impedance tube*", paper downloaded from www.microflown.com.
- Van Tol, F. H., Verheij, J. W., "*Loudspeaker for reciprocal measurements of near field sound transfer functions on heavy road vehicle engines*", TNO Institute of Applied Physics, 1993.
- Whear, F.R., Morrey, D., "*A technique for experimental acoustic modal analysis*", Proc. Instn. Mech. Engrs., vol. 210, pp. 143-151, 1996.

Appendix A

Acoustic wave equation

The physical phenomenon of sound waves in fluids (i.e., gases or liquids) is related basically to the normal stresses, or pressures, since shear stresses can not be sustained statically in fluids. Sound in gases is, instead of an isothermal process, nearly an adiabatic phenomenon. That is to say that there is insignificant exchange of thermal energy from one particle of fluid to another. For a gas under this condition, its behavior may be described by the adiabatic equation of state:

$$\frac{P}{P_0} = \left(\frac{\rho}{\rho_0} \right)^\gamma \quad (\text{A.1})$$

where γ is the ratio of the specific heats, P and ρ are the instantaneous pressure and density, P_0 and ρ_0 the mean pressure and density (the difference between P and P_0 represents the acoustic pressure p). For fluids in general, the adiabatic equation of state is more complicated and the Taylor expansion for the compression and expansion of the fluid about its equilibrium density can be written:

$$P = P_0 + \left(\frac{\partial P}{\partial \rho} \right)_{\rho_0} (\rho - \rho_0) + \frac{1}{2} \left(\frac{\partial^2 P}{\partial \rho^2} \right)_{\rho_0} (\rho - \rho_0)^2 + \dots \quad (\text{A.2})$$

If the fluctuations are small, only the lowest term in $(\rho - \rho_0)$ need to be retained. To give an idea of how this approach is valid for air, for a pressure level of 100 dB the ratio p/P_0 is 2×10^{-5} and the non-linearity represented by the higher order terms of the Taylor expansion are only

needed to be accounted for pressure levels above 135 dB. The present study is concerned with the analysis of the acoustics of cavities filled by air with zero mean velocity field and pressure levels under 100 dB, which has many applications (i.e., aircraft and automobile cabins). The linear relationship between pressure and density fluctuations becomes:

$$P - P_0 = p = \left(\frac{\partial P}{\partial \rho} \right)_{\rho_0} (\rho - \rho_0) \quad (\text{A.3})$$

Here the concept of '*bulk modulus*' is introduced. It is a coefficient relating pressure changes to small volumetric (dilatational) strains of a fluid ($= \rho_0 (\partial P / \partial \rho)_{\rho_0}$). For adiabatic changes, P/ρ^γ is constant and the bulk modulus can be rewritten:

$$\rho_0 \left(\frac{\partial P}{\partial \rho} \right)_{\rho_0} = \gamma P_0 \quad (\text{A.4})$$

and the acoustic pressure is simplified:

$$p = \gamma P_0 \frac{(\rho - \rho_0)}{\rho_0} = \gamma P_0 s \quad (\text{A.5})$$

where s is called condensation.

The wave equation is a result of mass and momentum conservation. Figure A.1 shows the mass flux in x direction with the velocity being expanded only in one term (linear in the control volume). For all directions, the rate of mass flow into the control volume is:

$$(\rho u_x) dy dz + (\rho u_y) dx dz + (\rho u_z) dx dy \quad (\text{A.6})$$

and the rate of mass flowing out is:

$$\left(\rho u_x + \left(\frac{\partial(\rho u_x)}{\partial x} \right) dx \right) dy dz + \left(\rho u_y + \left(\frac{\partial(\rho u_y)}{\partial y} \right) dy \right) dx dz + \left(\rho u_z + \left(\frac{\partial(\rho u_z)}{\partial z} \right) dz \right) dx dy \quad (\text{A.7})$$

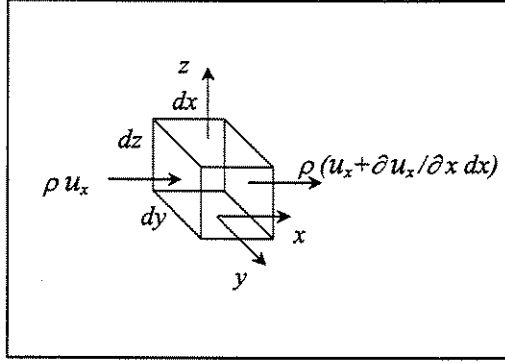


Figure A.1 – Mass flux through a fluid control volume in the x direction

The net mass outflow must be balanced by a decrease in the density of the volume:

$$\left[\frac{\partial(\rho u_x)}{\partial x} + \frac{\partial(\rho u_y)}{\partial y} + \frac{\partial(\rho u_z)}{\partial z} \right] dV = - \left(\frac{\partial \rho}{\partial t} \right) dV \quad (\text{A.8})$$

where $dV = dx dy dz$. Assuming that the density fluctuations are very small, the previous non-linear equation can be linearized:

$$\rho_0 \nabla \cdot \bar{u} + \frac{\partial \rho}{\partial t} = 0 \quad (\text{A.9})$$

where $\bar{u} = u_x \bar{i} + u_y \bar{j} + u_z \bar{k}$. Considering the fluid inviscid (no viscosity effects) and a small element dV (figure A.2) moving with the fluid, the net force $d\bar{f}$ on the element will accelerate it according to the Newton's second law ($d\bar{f} = \bar{A} dm$). In the x direction, the resulting force is:

$$df_x = - \frac{\partial p}{\partial x} dV \quad (\text{A.10})$$

For the complete force vector:

$$d\bar{f} = -\nabla p dV \quad (\text{A.11})$$

The particle acceleration is a function of time and space and a small increment in both variables gives the acceleration by the following relation:

$$\bar{a} = \lim_{dt \rightarrow 0} \frac{\bar{u}(x + u_x dt, y + u_y dt, z + u_z dt, t + dt) - \bar{u}(x, y, z, t)}{dt} \quad (\text{A.12})$$

A Taylor expansion (taking into account only the first terms),

$$\bar{u}(x + u_x dt, y + u_y dt, z + u_z dt, t + dt) = \bar{u}(x, y, z, t) + \frac{\partial \bar{u}}{\partial x} u_x dt + \frac{\partial \bar{u}}{\partial y} u_y dt + \frac{\partial \bar{u}}{\partial z} u_z dt + \frac{\partial \bar{u}}{\partial t} dt \quad (\text{A.13})$$

leads to the acceleration equation:

$$\bar{a} = \frac{\partial \bar{u}}{\partial t} + u_x \frac{\partial \bar{u}}{\partial x} + u_y \frac{\partial \bar{u}}{\partial y} + u_z \frac{\partial \bar{u}}{\partial z} = \frac{\partial \bar{u}}{\partial t} + (\bar{u} \cdot \nabla) \bar{u} \quad (\text{A.14})$$

Substitution into the Newton's second law equation gives the well-known non-linear Euler's equation:

$$\nabla p = -\rho \left(\frac{\partial \bar{u}}{\partial t} + (\bar{u} \cdot \nabla) \bar{u} \right) \quad (\text{A.15})$$

Supposing $|s| \ll 1$ and $|(\bar{u} \cdot \nabla) \bar{u}| \ll |\partial \bar{u} / \partial t|$, ρ can be approximated by ρ_0 and the term $(\bar{u} \cdot \nabla) \bar{u}$ dropped in (A.15). The linearized Euler's equation can then be written:

$$\nabla p = -\rho_0 \frac{\partial \bar{u}}{\partial t} \quad (\text{A.16})$$

The wave equation is the result of some manipulations between (A.5), (A.9) and (A.16). Application of the divergent operator in (A.16) produces:

$$\nabla^2 p = -\rho_0 \frac{\partial \nabla \cdot \bar{u}}{\partial t} \quad (\text{A.17})$$

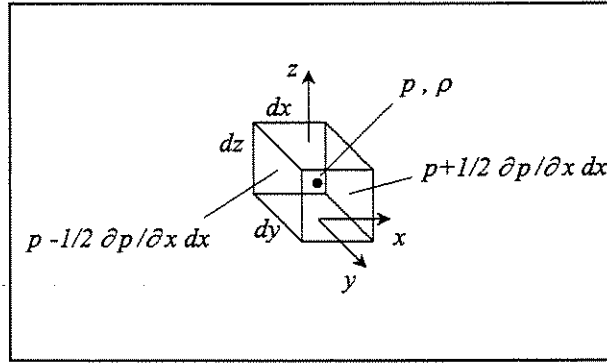


Figure A.2 – Pressure gradient in the x direction

The combination of equations (A.5) and (A.9) gives:

$$\nabla \cdot \vec{u} = -\frac{1}{\gamma P_0} \frac{\partial p}{\partial t} \quad (\text{A.18})$$

which, applied to (A.17), results in the wave equation:

$$\nabla^2 p - \frac{1}{c^2} \frac{\partial^2 p}{\partial t^2} = 0 \quad (\text{A.19})$$

where $c = \sqrt{\gamma P_0 / \rho_0}$ is the speed of propagation of sound in all regions where the linear approximation holds good.

Appendix B

Acoustic intensity

B.1 – Acoustic intensity in plane wave fields

The study of acoustic intensity in plane wave fields is made here due to the insightful results it may lead when analyzing active and reactive fields. Fahy (1995) treats the problem in detail and some of his ideas will be summarized here.

The instantaneous intensity,

$$I(t) = p(t)v(t) \tag{B.1.1}$$

in all time-stationary acoustic fields may be split into two components:

- *Active*: which the time-average (mean) value is non-zero, corresponding to local net transport of sound energy;
- *Reactive*: which the time-average value is zero, corresponding to local oscillatory transport of energy.

As an example, the active and reactive intensity will be derived for an one-dimensional plane interference field represented by the following pressure expression:

$$p(x,t) = P(x)e^{i(\omega t + \phi_p(x))} \tag{B.1.2}$$

where $P(x)$ is real (the dependence on x of P and ϕ will be dropped for typographical clarity). Using the Euler's relation, the particle velocity can be written:

$$u(x,t) = \frac{1}{\omega\rho_0} \frac{\partial p}{\partial x} = \frac{1}{\omega\rho_0} \left[-P \frac{d\phi_p}{dx} + i \frac{dP}{dx} \right] e^{i(\omega t + \phi_p(x))} \quad (\text{B.1.3})$$

The active component of intensity is given by the product of the components of pressure and particle velocity that are in phase:

$$I_a(x,t) = -\frac{1}{\omega\rho_0} \left[P^2 \frac{d\phi_p}{dx} + i \frac{dP}{dx} \right] \cos^2(\omega t + \phi_p(x)) \quad (\text{B.1.4})$$

and its mean value is

$$\bar{I}_a(x,t) = -\frac{1}{2\omega\rho_0} \left[P^2 \frac{d\phi_p}{dx} + i \frac{dP}{dx} \right] \quad (\text{B.1.5})$$

The reactive component of intensity results from the product of the components of pressure and particle velocity that are in quadrature:

$$I_{re}(x,t) = -\frac{1}{4\omega\rho_0} \left[\frac{dP^2}{dx} \right] \sin 2(\omega t + \phi_p(x)) \quad (\text{B.1.6})$$

From these intensity equations, we can see that the active component is related to the spatial gradient of phase, and the reactive component to the spatial gradient of mean square pressure. A very useful example in this study is the *standing wave* or *impedance* tube, which is used to measure the sound absorption of materials. Keeping the analysis below the lowest cut-off frequency of the tube leads to a one-dimensional plane wave problem. The material put at the end of the tube is modeled as having a complex pressure reflection coefficient represented by $R e^{i\theta}$. The pressure field is represented in complex exponential form by:

$$p(x,t) = A \left[e^{i(\omega t - kx)} + R e^{i\theta} e^{i(\omega t + kx)} \right] \quad (\text{B.1.7})$$

This pressure field may be expressed by:

$$p(x,t) = P e^{i\phi_p} e^{i\omega t} \quad (\text{B.1.8})$$

where

$$\phi_p = \tan^{-1} \left[\frac{R \sin(kx + \theta) - \sin(kx)}{R \cos(kx + \theta) + \cos(kx)} \right] \quad (\text{B.1.9})$$

and

$$P^2 = A^2 [1 + R^2 + 2R \cos(2kx + \theta)] \quad (\text{B.1.10})$$

The spatial gradients of these quantities are:

$$\frac{d\phi_p}{dx} = \frac{k(R^2 - 1)A^2}{P^2} \quad (\text{B.1.11})$$

and

$$\frac{dP^2}{dx} = -4A^2 k R \sin(2kx + \theta) \quad (\text{B.1.12})$$

Substitution of these gradient expressions in (B.1.5) and (B.1.6) gives the intensity equations for the *impedance* tube:

$$I_a(x,t) = \frac{A^2}{\rho_0 c} (1 - R^2) \cos^2(\omega t + \phi_p(x)) \quad (\text{B.1.13})$$

$$\bar{I}_a(x,t) = \frac{A^2}{2\rho_0 c} (1 - R^2) \quad (\text{B.1.14})$$

$$I_{re}(x,t) = \frac{A^2}{\rho_0 c} R \sin(2kx + \theta) \sin 2(\omega t + \phi_p(x)) \quad (\text{B.1.15})$$

Three important conclusions can be drawn from these equations: (i) the mean active intensity is independent of x and uniform along the tube length, relating clearly this variable to the net transport of sound energy; (ii) the mean reactive intensity is zero, characterizing the local oscillatory transport of energy; and (iii) the ratio of the magnitudes of active and reactive intensities vary with position: a maximum value of $R/(1-R^2)$ at the position of maximum and minimum square particle velocity, and a minimum value of zero at the maximum and minimum of square pressure, respectively.

B.2 – Complex intensity for harmonic acoustic fields

A generalized formulation for a complex harmonic acoustic field is easily found by introducing a complex harmonic pressure and particle velocity field,

$$p(x,t) = P e^{i\omega t} \quad (\text{B.2.1})$$

$$u(x,t) = U e^{i(\omega t + \phi)} \quad (\text{B.2.2})$$

where ϕ is the phase shift between pressure and particle velocity as shown in figure B.2.1, with P and U real positives.

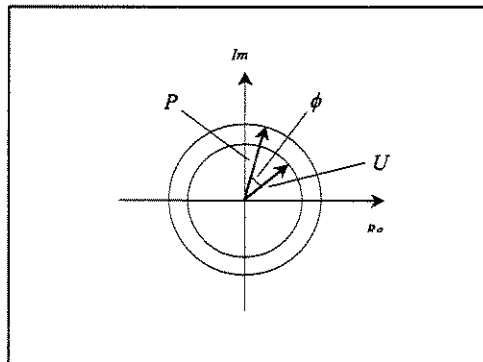


Figure B.2.1 – Phase shift between pressure and particle velocity

The instantaneous acoustic intensity (B.1.1) can be written:

$$I(t) = PU \left[\cos^2(\omega t) \cos(\phi) + \cos(\omega t) \sin(\omega t) \sin(\phi) \right] \quad (\text{B.2.3})$$

which leads to

$$I(t) = \frac{PU}{2} \left[(\cos(2\omega t) + 1) \cos(\phi) + \sin(2\omega t) \sin(\phi) \right] \quad (\text{B.2.4})$$

The term in cosines of ϕ has its average equal to:

$$\bar{I}_{\cos(\phi)} = \frac{PU}{2} \cos(\phi) \quad (\text{B.2.5})$$

and it is pulsating from an amplitude of zero to PU with the double of the excitation frequency. It is usually referred as active acoustic intensity, and it is related to the net energy transport represented by its average.

Averaging over the sinus term results zero, not contributing to the net energy transport and representing only the energy balance between potential and kinetic acoustic energy. This intensity component pulses from $-PU/2$ to $PU/2$ with the double of the excitation frequency and is usually referred as reactive acoustic intensity. Acoustic intensity is generally written as:

$$I = \bar{I}_{active} + I_{reactive} = \frac{PU}{2} \cos(\phi) + \frac{PU}{2} \sin(\phi) \sin(2\omega t) \quad (\text{B.2.6})$$

Interesting to note is that when ϕ is 90° there is a pure reactive field and the active intensity equals zero. In real cavities there is always some dissipation and the phase shift between pressure and particle velocity never reaches exactly 90° , leading always to the injection of active intensity by the source(s), even if it is small.

From the following complex notation,

$$PU^* = (P \cos(\phi_p) + iP \sin(\phi_p))(U \cos(\phi_p) - iU \sin(\phi_p)) = PU \cos(\phi) + iPU \sin(\phi) \quad (\text{B.2.7})$$

where $\phi = \phi_p - \phi_u$, the acoustic intensity can be written in a complex notation:

$$I = \bar{I}_{active} + I_{reactive} = \text{Re}\left\{\frac{PU^*}{2}\right\} + i \text{Im}\left\{\frac{PU^*}{2}\right\} \quad (\text{B.2.8})$$

B.3 – Monopole intensity

The pressure field generated by a monopole can be written as:

$$p(r,t) = \frac{A}{r} e^{i(\omega t - kr)} \quad (\text{B.3.1})$$

Applying the Euler's relation, the particle velocity field is found:

$$u(r,t) = \frac{A}{\omega \rho_0 r} \left(k - \frac{i}{r}\right) e^{i(\omega t - kr)} \quad (\text{B.3.2})$$

The active and reactive intensities are then calculated:

$$I_a(r,t) = \frac{A^2}{2r^2 \rho_0 \omega} [1 + \cos 2(\omega t - kr)] \quad (\text{B.3.3})$$

$$I_{re}(r,t) = \frac{A^2}{2r^3 \rho_0 \omega} \sin 2(\omega t - kr) \quad (\text{B.3.4})$$

The relation between active and reactive intensities becomes:

$$\frac{|I_a|}{|I_{re}|} = k r \tag{B.3.5}$$

This last relation shows that the reactive intensity dominates in the near field ($kr \ll 1$) while the active intensity dominates in the far field ($kr \gg 1$).

Appendix C

Acoustic specific impedance for a spherical wave diverging from a point source

The complex representation of a spherical wave diverging from a point source (monopole behavior) can be written (Kinsler, 1982) as:

$$p = \frac{A}{r} e^{i(\omega t - kr)} \quad (\text{C.1.1})$$

The particle velocity is obtained by applying the Euler's relation to the pressure expression:

$$\vec{u} = \nabla \Phi = \left(1 - \frac{i}{kr}\right) \frac{p}{\rho_0 c} \hat{r} \quad (\text{C.1.2})$$

It is clear from (C.1.1) that pressure and particle velocity are not in phase. The specific acoustic impedance is:

$$z = \rho_0 c \frac{kr}{\sqrt{1 + (kr)^2}} e^{i\theta} \quad (\text{C.1.3})$$

or

$$z = \rho_0 c \cos(\theta) e^{i\theta} \quad (\text{C.1.4})$$

where

$$\cot(\theta) = kr \tag{C.1.5}$$

Splitting (C.1.3) into real and imaginary parts, it becomes:

$$z = \rho_0 c \frac{(kr)^2}{1 + (kr)^2} + i\rho_0 c \frac{kr}{1 + (kr)^2} \tag{C.1.6}$$

Both the specific acoustic resistance (real part) and the reactance (imaginary part) approach zero for small values of kr . For large values of kr , the real term tends to $\rho_0 c$ (behavior of a plane wave) and the imaginary tends to zero. When $kr = 1$, both terms are equal to $\rho_0 c/2$ and the specific acoustic reactance has its maximum value.

Appendix D

Spatial Discrete Fourier Transform

D.1 – One-dimensional problem

The spatial Fourier transform of a continuous signal $f(x)$ is expressed as:

$$F(k_x) = \int_{-\infty}^{\infty} f(x) e^{-ik_x x} dx \quad (\text{D.1.1})$$

The Fourier Transform of the discretized signal $f_n = f(x = n\Delta x)$ can be calculated by approximating the integral by the sum $\sum_{n=0}^{N-1}$ multiplied by $\Delta k_x (= 1/L = 1/N\Delta x)$, and dx becomes the interval Δx between the discretized points (N is the number of sampled points). The spatial frequency (wave number) k_x is written:

$$k_x = \frac{2\pi}{L} \beta = \frac{2\pi}{N\Delta x} \beta \quad \beta = 0, \dots, N-1 \quad (\text{D.1.2})$$

The one-dimensional Discrete Fourier Transform (*DFT*) becomes:

$$F_\beta = \frac{1}{N} \sum_{n=0}^{N-1} f_n W_N^{-\beta n} \quad \beta = 0, \dots, N-1 \quad (\text{D.1.3})$$

where

$$W_N = e^{\frac{i2\pi}{N}} \quad (\text{D.1.4})$$

The steps followed above do not represent a rigorous proof of the *DFT* formulation and a more strict development can be found in (Brigham, 1974).

Equation (D.1.3) can be written in matrix notation:

$$\mathbf{F} = \frac{1}{N} \mathbf{W} \mathbf{f} \quad (\text{D.1.5})$$

where

$$\mathbf{W}_{\beta n} = \sum_{\beta=0}^{N-1} \sum_{n=0}^{N-1} W_N^{-\beta n} \quad (\text{D.1.6})$$

$$\mathbf{F}_{\beta} = F_{\beta} \quad \beta = 0, \dots, N-1 \quad (\text{D.1.7})$$

$$\mathbf{x}_n = x_n \quad n = 0, \dots, N-1 \quad (\text{D.1.8})$$

Due to the orthogonality property of the complex exponential, it can be written:

$$\mathbf{W}^H \mathbf{W} = N \mathbf{I} \quad (\text{D.1.9})$$

where \mathbf{I} is the identity matrix and the superscript H the complex conjugate transpose. The Inverse Discrete Fourier Transform (*IDFT*) is calculated with the combination of (D.1.5) and (D.1.9):

$$\mathbf{f} = \mathbf{W}^H \mathbf{F} \quad (\text{D.1.10})$$

The first spatial derivative of $f(x)$,

$$f(x) = \int_{-\infty}^{\infty} F(k_x) e^{ik_x x} dk_x \quad (\text{D.1.11})$$

can be found from the *IDFT* of $F(K_x)$ multiplied by iK_x :

$$\frac{df(x)}{dx} = \int_{-\infty}^{\infty} ik_x F(k_x) e^{ik_x x} dk_x \quad (\text{D.1.12})$$

The expression of the first derivative of $f(x)$ in matrix notation is:

$$\left[\frac{df}{dx} \right] = i [F(k_x)] [\text{diag}(k_x)] [\mathbf{W}]^T \quad (\text{D.1.13})$$

As an example, the first derivative of the following function (Figure D.1.1) will be calculated.

$$f(x) = A \left[\sin\left(\frac{2\pi x}{L}\right) + \sin\left(\frac{4\pi x}{L} + \frac{\pi}{4}\right) + \sin\left(\frac{6\pi x}{L} + \frac{3\pi}{2}\right) \right] \quad (\text{D.1.14})$$

The analytical expression of its first derivative is:

$$\frac{df(x)}{dx} = A \left[\frac{2\pi x}{L} \cos\left(\frac{2\pi x}{L}\right) + \frac{4\pi x}{L} \cos\left(\frac{4\pi x}{L} + \frac{\pi}{4}\right) + \frac{6\pi x}{L} \cos\left(\frac{6\pi x}{L} + \frac{3\pi}{2}\right) \right] \quad (\text{D.1.15})$$

and figure D.1.2 shows (for $A = 1$ and $L = 3$) the comparison between the results from the analytical expression and with use of the *DFT* and *IDFT*.

It is important to notice that some care must be taken to avoid distortions in the Fourier Transform of a sampled function (Brigham, 1974). The problem associated with the sampling frequency is called *aliasing* and it is avoided if the sampling spatial frequency ($1/\Delta x$) is higher or

equal the double of the maximum spatial frequency analyzed. The necessary truncation of the signal introduces an effect called *leakage* as discontinuities in the spatial domain generate side-lobes in the frequency domain. This problem can be controlled if appropriated windowing or a smoothing technique as proposed in (Arruda, 1992) is applied.

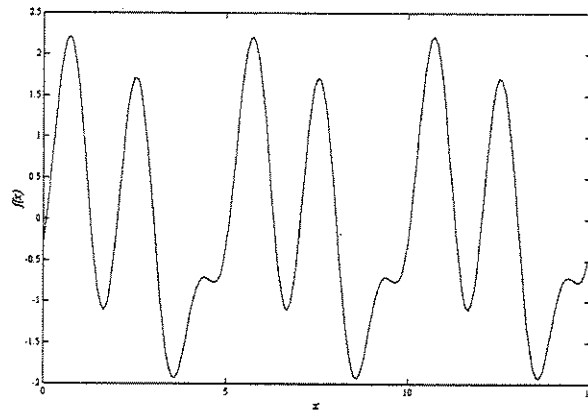


Figure D.1.1 – Function $f(x)$ for $A = 1$ and $L = 3$

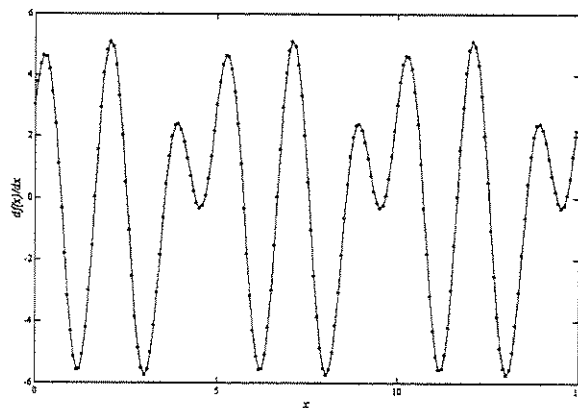


Figure D.1.2 – Analytical (—) and from DFT/IDFT (●) first derivative of $f(x)$

D.2 – Two-dimensional problem

The two-dimensional *DFT* in rectangular coordinates is obtained in a similar manner as the one-dimensional *DFT* applied to the x and y directions:

$$F(k_x, k_y) = \frac{1}{A} \frac{1}{B} \sum_{a=0}^{A-1} \sum_{b=0}^{B-1} f(b\Delta x, a\Delta y) e^{-ik_x b\Delta x} e^{-ik_y a\Delta y} \quad (\text{D.2.1})$$

where A and B are the number of points in y and x , respectively. The wave numbers are defined as:

$$k_x = \frac{2\pi}{L_x} k_1 = \frac{2\pi}{B\Delta x} k_1 \quad k_1 = 0, \dots, B-1 \quad (\text{D.2.2})$$

and

$$k_y = \frac{2\pi}{L_y} k_2 = \frac{2\pi}{A\Delta y} k_2 \quad k_2 = 0, \dots, A-1 \quad (\text{D.2.3})$$

In matrix notation the two-dimensional *DFT* becomes:

$$[F(k_x, k_y)]_{A \times B} = \frac{1}{A} \frac{1}{B} [W_A]_{A \times A} [f(x, y)]_{A \times B} [W_B]_{B \times B} \quad (\text{D.2.4})$$

where

$$[W_B] = \sum_{k_1=0}^{B-1} \sum_{b=0}^{B-1} e^{\frac{2\pi k_1 b}{B}} \quad (\text{D.2.5})$$

and

$$[W_A] = \sum_{k_2=0}^{A-1} \sum_{a=0}^{A-1} e^{\frac{2\pi k_2 a}{A}} \quad (\text{D.2.6})$$

The first spatial derivatives are found from the same procedure as followed in the one-dimensional case. For the x direction the DFT becomes:

$$F(k_x, y) = \frac{1}{B} \sum_{b=0}^{B-1} f(b\Delta x, y) e^{-ik_x b\Delta x} \quad (D.2.7)$$

Its matrix notation is:

$$[F(k_x, y)]_{A \times B} = \frac{1}{B} [f(x, y)]_{A \times B} [W_B]_{B \times B} \quad (D.2.8)$$

The first derivative is readily calculated:

$$\left[\frac{\partial f(x, y)}{\partial x} \right] = i [F(k_x, y)] [diag(k_x)] [W_B]^T \quad (D.2.9)$$

In the y direction the same procedure is developed. The DFT in y is:

$$F(x, k_y) = \frac{1}{A} \sum_{a=0}^{A-1} f(x, a\Delta y) e^{-ik_y a\Delta y} \quad (D.2.10)$$

In addition, its matrix notation becomes:

$$[F(x, k_y)]_{A \times B} = \frac{1}{A} [W_A]_{A \times A} [f(x, y)]_{A \times B} \quad (D.2.11)$$

The first derivative in y is readily calculated:

$$\left[\frac{\partial f(x, y)}{\partial y} \right] = i [W_A]^T [diag(k_y)] [F(x, k_y)] \quad (D.2.12)$$

Following, two examples of the application of the two-dimensional *DFT* to find the first derivative in two directions will be presented: a problem in rectangular coordinates and a problem in cylindrical coordinates.

This first case is related to the study of a rectangular acoustic cavity ($L_x = 25.4\text{cm} \times L_y = 19.9\text{cm} \times L_z = 3\text{cm}$) with rigid walls and the third dimension (3cm) much smaller than the others two. This leads to a two-dimensional problem with the following solution for the pressure field:

$$p_{mn} = A_{mn} \cos(k_{xm}x) \cos(k_{yn}y) \quad (\text{D.2.13})$$

The particle velocities are linked (linear acoustics) to the pressure gradient field by the Euler's relation,

$$\vec{u} = -\frac{1}{i\omega\rho_0} \nabla p \quad (\text{D.2.14})$$

and the analytical expressions for the particle velocities in x and y directions are

$$u_x = \frac{A_{mn}}{i\omega\rho_0 c} k_{xm} \sin(k_{xm}x) \cos(k_{yn}y) \quad (\text{D.2.15})$$

and

$$u_y = \frac{A_{mn}}{i\omega\rho_0 c} k_{yn} \cos(k_{xm}x) \sin(k_{yn}y) \quad (\text{D.2.16})$$

The wave numbers for each mode are found by application of the condition of null normal particle velocity at the boundaries:

$$k_{x_m} = \frac{m\pi}{L_x} \quad (\text{D.2.17})$$

$$k_{y_n} = \frac{n\pi}{L_y} \quad (\text{D.2.18})$$

Figure D.2.1 (left) shows the pressure field ($A_{mn} = 1$) for the 8th mode (1850Hz – $m = 1, n = 2$). It is clear that the application of the *DFT* in y will offer no problem as the it is perfectly periodic, but in x a spatial leakage will be present. To solve this problem the surface was mirrored (figure D.2.1 (right)) in the x direction and the spatial discontinuity was avoided.

The analytical particle velocity field for the x and y components is compared to the results obtained from the application of the *DFT* and *IDFT* to pressure field in figures D.2.2 and D.2.3. There is an excellent agreement.

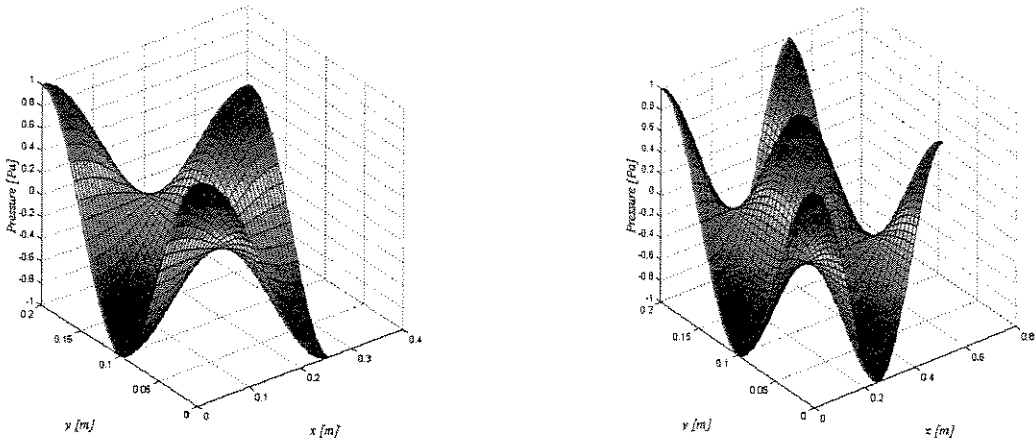


Figure D.2.1 – Pressure field for the 8th mode (1850Hz)
 (left) Original field (right) Original + Mirrored field

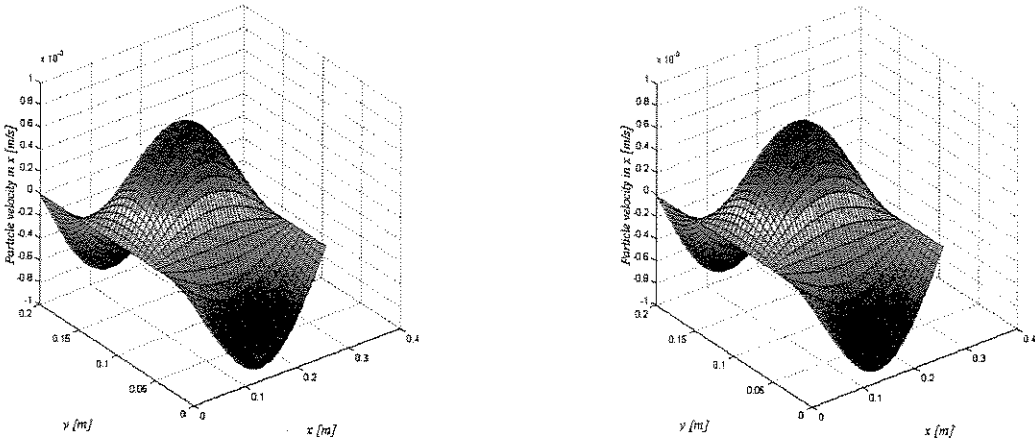


Figure D.2.2 – x -component of the particle velocity for the 8th mode
 (left) Analytical (right) From DFT and IDFT

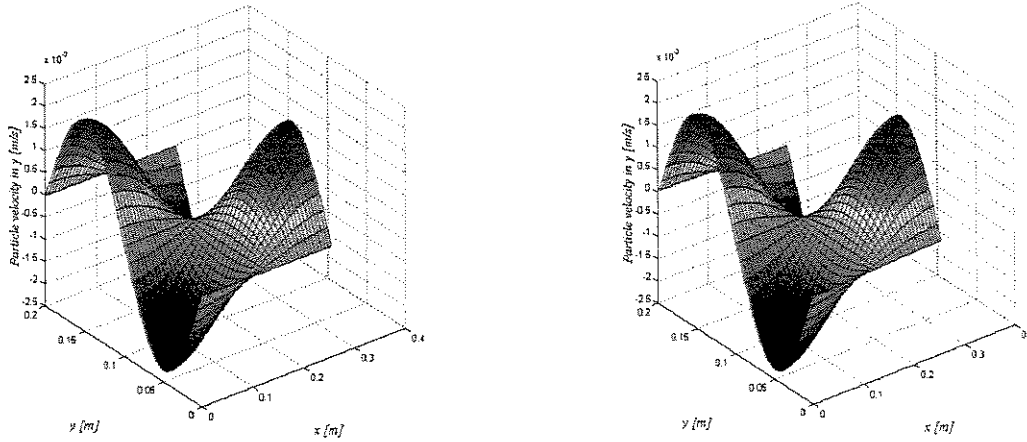


Figure D.2.3 – y -component of the particle velocity for the 8th mode
(left) Analytical (right) From DFT and IDFT

An interesting application of DFT is the treatment of problems in cylindrical coordinates. These problems have generally solutions based on Bessel functions, and, as these functions are constructed with sines and cosines, they are well fitted for Fourier Transforms application.

The same procedure adopted for the rectangular coordinates case is made for cylindrical coordinates case. For the angular direction θ , which is periodic, the DFT becomes:

$$F(r, k_{\theta}) = \frac{1}{A} \sum_{a=0}^{A-1} f(r, \theta) e^{-ik_{\theta} a \Delta \theta} \quad (D.2.19)$$

where

$$k_{\theta} = \frac{2\pi}{2\pi} k_3 = k_3 \quad k_3 = 0, \dots, A-1 \quad (D.2.20)$$

Its matrix notation is:

$$[F(r, k_{\theta})]_{A \times B} = \frac{1}{A} [W_{\theta}]_{A \times A} [f(r, \theta)]_{A \times B} \quad (D.2.21)$$

where

$$[W_{\theta}] = \sum_{k_3=0}^{A-1} \sum_{a=0}^{A-1} e^{\frac{2\pi k_3 a}{A}} \quad (D.2.22)$$

Its first derivative is calculated:

$$\left[\frac{\partial f(r, \theta)}{\partial \theta} \right] = i [W_\theta]^T [\text{diag}(k_\theta)] [F(r, k_\theta)] \quad (\text{D.2.23})$$

The *DFT* in the radial direction r becomes:

$$F(k_r, \theta) = \frac{1}{B} \sum_{b=0}^{B-1} f(b\Delta r, \theta) e^{-ik_r b \Delta r} \quad (\text{D.2.24})$$

where

$$k_r = \frac{2\pi}{L_r} k_4 = \frac{2\pi}{B\Delta r} k_4 \quad k_4 = 0, \dots, B-1 \quad (\text{D.2.25})$$

Its matrix notation is:

$$[F(k_r, \theta)]_{A \times B} = \frac{1}{B} [f(r, \theta)]_{A \times B} [W_r]_{B \times B} \quad (\text{D.2.26})$$

where

$$[W_r] = \sum_{k_4=0}^{B-1} \sum_{b=0}^{B-1} e^{\frac{2\pi k_4 b}{B}} \quad (\text{D.2.27})$$

Its first derivative is readily calculated:

$$\left[\frac{\partial f(r, \theta)}{\partial r} \right] = i [F(k_r, \theta)] [\text{diag}(k_r)] [W_r]^T \quad (\text{D.2.28})$$

As an example, the *DFT* will be applied to the interior pressure field of an infinite rigid-walled, circular waveguide of radius a ($= 1m$). The pressure field (Kinsler, 1982) is given by:

$$p_{mn} = A_{mn} J_m(k_{mn} r) \cos(m\theta) \quad (\text{D.2.29})$$

The wave numbers for each mode are found from the condition of null normal particle velocity at the boundaries:

$$k_{mn} = \frac{j'_{mn}}{a} \quad (\text{D.2.30})$$

where j'_{mn} are the zeros of $dJ_m(z)/dz$. Application of the Euler's relation (D.2.14) to the pressure field gives the particle velocities in the θ and r direction:

$$u_r = \frac{-A_{mn}}{ic\rho_0} J'_m(k_{mn}r) \cos(m\theta) \quad (\text{D.2.31})$$

$$u_\theta = \frac{A_{mn}m}{ik_{mn}c\rho_0} J_m(k_{mn}r) \sin(m\theta) \quad (\text{D.2.32})$$

The following relations related to the Bessel function were used in the construction of the analytical solution of the particle velocity in the r direction:

$$\frac{\partial J_n(z)}{\partial z} = J_{n-1}(z) - n z^{-1} J_n(z) \quad (\text{D.2.33})$$

$$J_{-s}(z) = (-1)^s J_s(z) \quad (\text{D.2.34})$$

Figure D.2.4 shows the pressure field ($A_{mn} = 1$) for the 12th mode (438Hz – $m = 3, n = 2$). In the angular direction θ the field is periodic and the *DFT* can be applied directly. In figure D.2.5 (left) it can be seen that in the r direction there will be a discontinuity when the field is periodized by the *DFT*. If a mirror is done (figure D.2.4 (right)) in this direction, leakage is suppressed and the *DFT* can be applied.

Results from the analytical formulation and from the application of the *DFT* and *IDFT* for the particle velocity field in the two directions is shown in figures D.2.5 and D.2.6, and they are in excellent agreement.

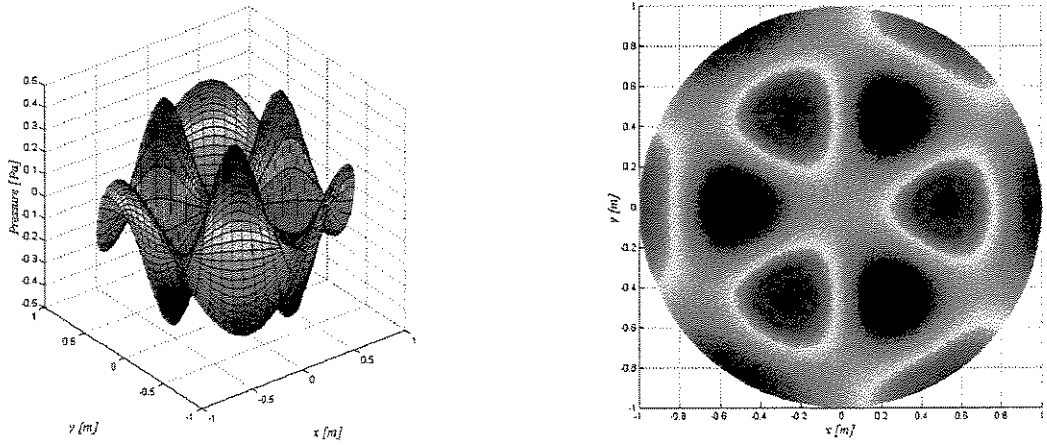


Figure D.2.4 – Pressure field for the 12th mode (438Hz)
 (left) 3D view (right) Top view

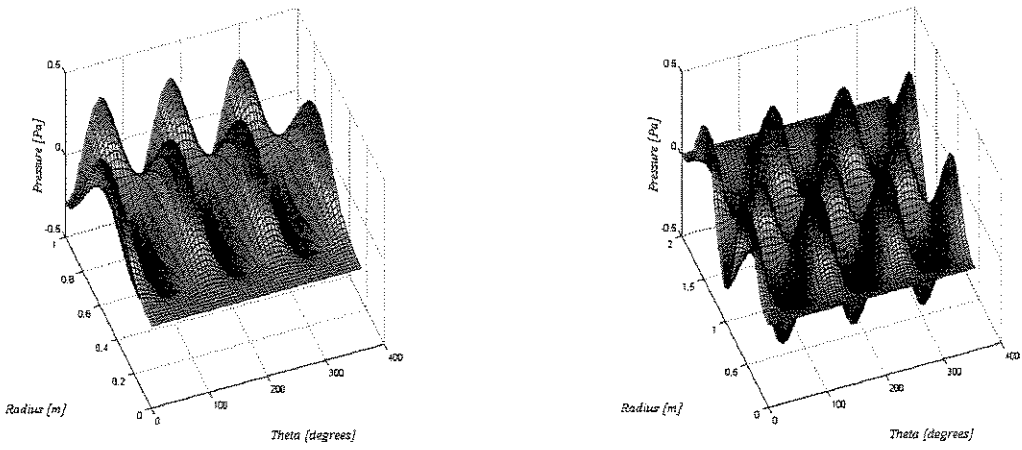


Figure D.2.5 – Pressure field for the 12th mode (438Hz)
 (left) Original field (right) Original + Mirrored field

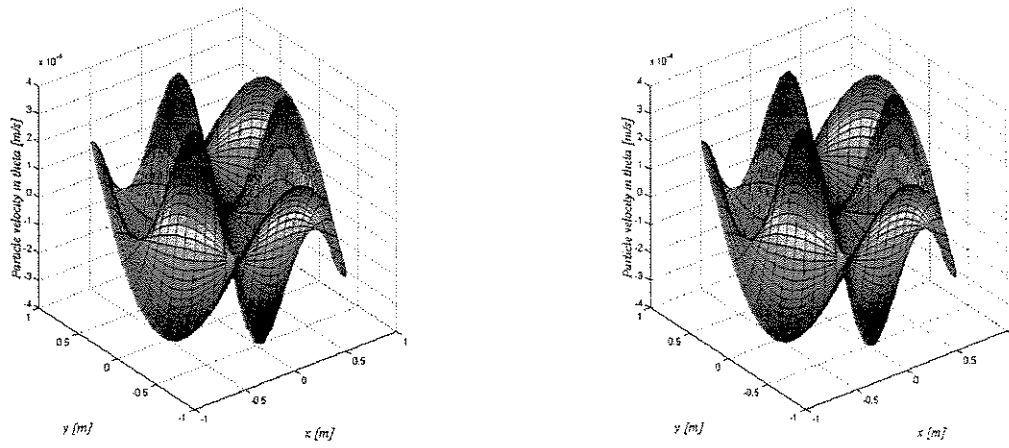


Figure D.2.6 – θ -component of the particle velocity for the 12th mode
 (left) Analytical (right) From DFT and IDFT

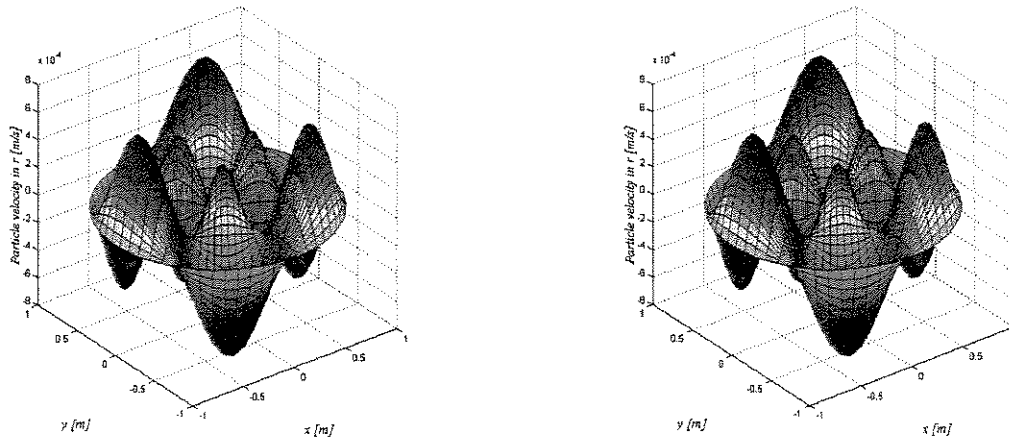


Figure D.2.7 – r -component of the particle velocity for the 12th mode
 (left) Analytical (right) From DFT and IDFT

D.3 – Three-dimensional problem

The three-dimensional case is a natural extension of the two-dimensional problem. Below an example similar to the first example given in the two-dimensional case is tested. The 43th mode (1964Hz) of an acoustic box of $0.5 \times 0.4 \times 0.3m$ is analyzed (figure D.3.1).

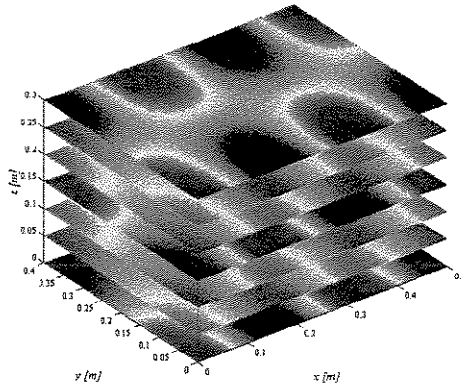


Figure D.3.1 – Pressure field for the 43th mode (1964Hz)

Figure D.3.2 shows the comparison between the analytical solution and the solution from the application of the DFT and IDFT for the x -component of the particle velocity for this mode.

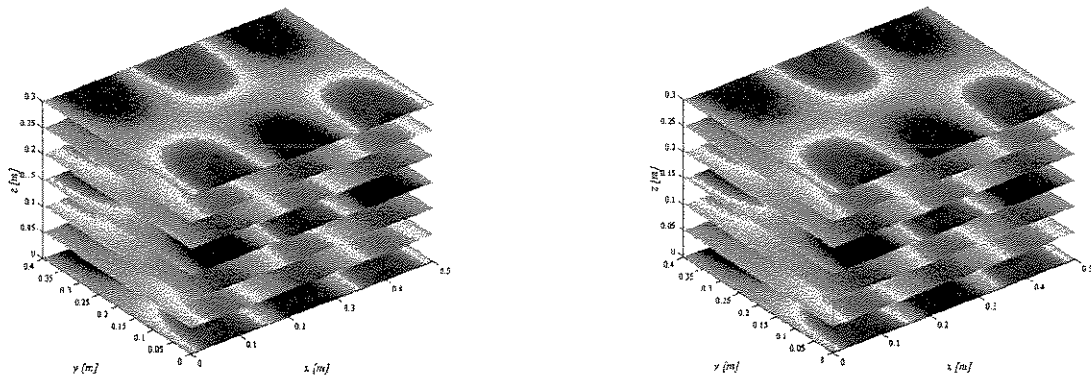


Figure D.3.2 – x -component of the particle velocity for the 43th mode
(left) Analytical (right) From DFT and IDFT

The use of the wire-frame representation, as mentioned in chapter 2, is very interesting and figure D.3.3 shows the two possibilities of visualizing the acoustic field.

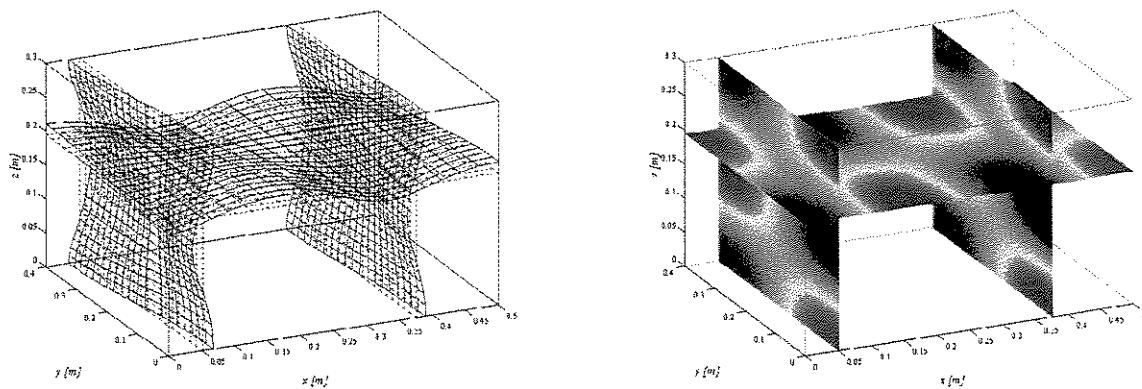
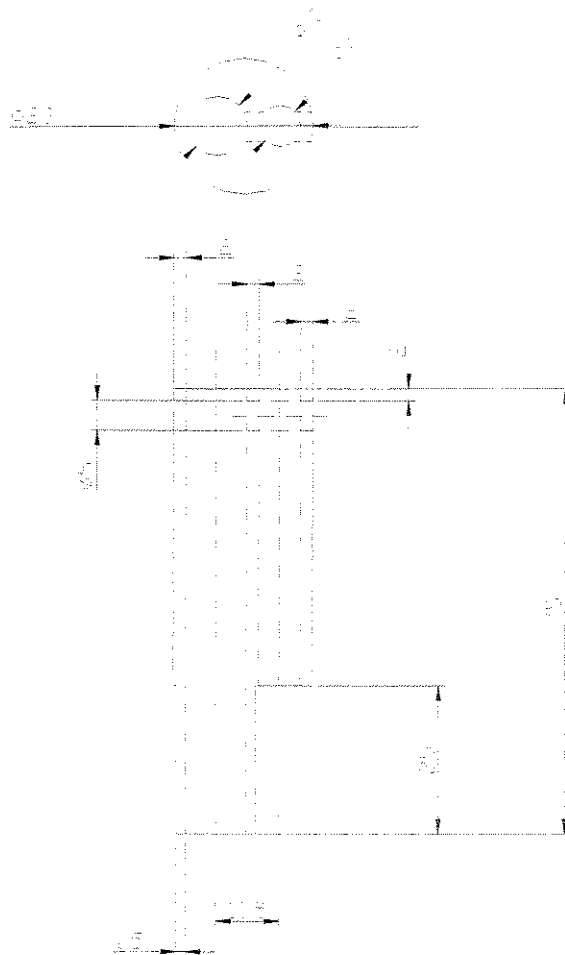


Figure D.3.3 – Particle displacement (left) and pressure (right) fields for the 43th mode

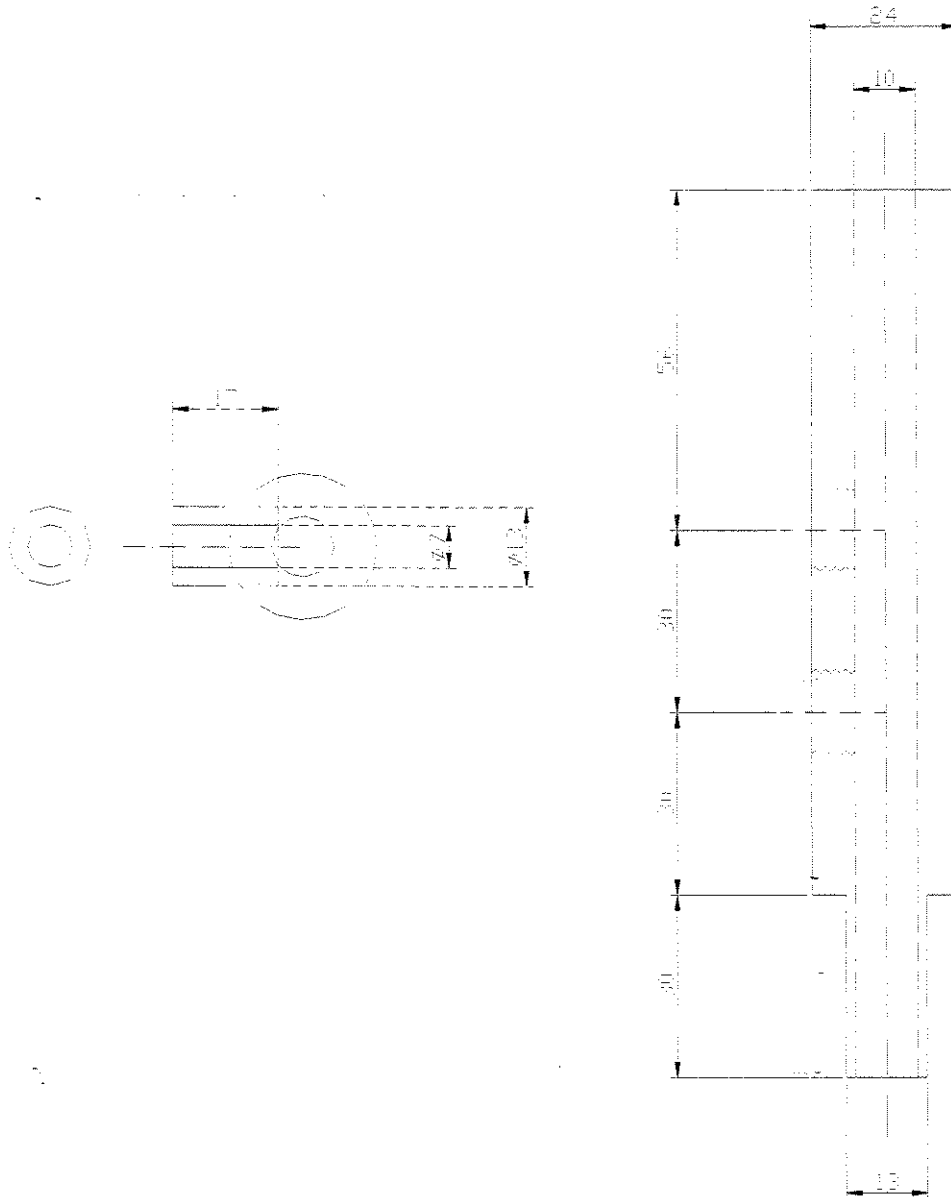
Appendix E

Actuators' scheme

One-microphone actuator (units in mm)



Two-microphone actuator (units in mm)



© 2000 Intel Corporation
All rights reserved. Intel, the Intel logo, and Pentium are trademarks or registered trademarks of Intel Corporation or its subsidiaries in the United States and other countries.